Summer 8-15-2015

Bio-Inspired Multi-Spectral Imaging Sensors and Algorithms for Image Guided Surgery

Shengkui Gao
Washington University in St. Louis

WASHINGTON UNIVERSITY IN ST. LOUIS

School of Engineering and Applied Science
Department of Computer Science and Engineering

Dissertation Examination Committee:
Viktor Gruev, Chair
Mark Anastasio
Roger Chamberlain
Yasutaka Furukawa
Richard Loomis
Robert Pless

Bio-Inspired Multi-Spectral Imaging Sensors and Algorithms for Image Guided Surgery

by
Shengkui Gao

A dissertation presented to the
Graduate School of Arts & Sciences
of Washington University in
partial fulfillment of the
requirements for the degree
of Doctor of Philosophy

August 2015
St. Louis, Missouri

Table of Contents

List of Figures

List of Tables

Acknowledgments

I would like to thank Dr. Viktor Gruev for all of his guidance and encouragement through my entire Ph.D. career. He always offered me guidance, valuable suggestions and comments regarding not only on research directions and problems, but also my career development. He is such a great advisor who guided me through my whole doctoral study.

I would also like to thank my lab mates from Advanced Sensors Research Laboratory for the countless help and great discussion. I would also like to thank the research collaborators from WUSTL Medical School, University of Arizona and many other places. Their expertise in different fields helped broaden my research vision.

I would like to thank all members serving on my proposal and dissertation committee for their time and patience, as well as the insightful feedback, suggestions and comments. They have guided me to greatly improve my research work.

Finally, I would like to thank my family. My family has given me tremendous help and support on my foreign graduate study. I would especially thank my wife Yawen, for her support and understanding during the whole of my graduate career and beyond.

Shengkui Gao

Washington University in St. Louis

August 2015

Dedicated to my wife and parents.

ABSTRACT OF THE DISSERTATION

Bio-Inspired Multi-Spectral Imaging Sensors and Algorithms for Image Guided Surgery

by

Shengkui Gao

Doctor of Philosophy in Computer Engineering

Washington University in St. Louis, 2015

Professor Viktor Gruev, Chair

Image guided surgery (IGS) utilizes emerging imaging technologies to provide additional structural and functional information to the physician in clinical settings. This additional visual information can help physicians delineate cancerous tissue during resection as well as avoid damage to near-by healthy tissue. Near-infrared (NIR) fluorescence imaging (700 nm to 900 nm wavelengths) is a promising imaging modality for IGS, namely for the following reasons: First, tissue absorption and scattering in the NIR window is very low, which allows for deeper imaging and localization of tumor tissue in the range of several millimeters to a centimeter depending on the tissue surrounding the tumor. Second, spontaneous tissue fluorescence emission is minimal in the NIR region, allowing for high signal-to-background ratio imaging compared to visible spectrum fluorescence imaging. Third, decoupling the fluorescence signal from the visible spectrum allows for optimization of NIR fluorescence while attaining high quality color images. Fourth, there are two FDA approved fluorescent dyes in the NIR region—namely methylene blue (MB) and indocyanine green—which can help to identify tumor tissue due to passive accumulation in human subjects.

The aforementioned advantages have led to the development of NIR fluorescence imaging systems for a variety of clinical applications, such as sentinel lymph node imaging, angiography,

and tumor margin assessment. With these technological advances, secondary surgeries due to positive tumor margins or damage to healthy organs can be largely mitigated, reducing the emotional and financial toll on the patient.

Currently, several NIR fluorescence imaging systems (NFIS) are available commercially or are undergoing clinical trials, such as FLARE, SPY, PDE, Fluobeam, and others. These systems capture multi-spectral images using complex optical equipment and are combined with real-time image processing to present an augmented view to the surgeon. The information is presented on a standard monitor above the operating bed, which requires the physician to stop the surgical procedure and look up at the monitor. The break in the surgical flow sometimes outweighs the benefits of fluorescence based IGS, especially in time-critical surgical situations. Furthermore, these instruments tend to be very bulky and have a large foot print, which significantly complicates their adoption in an already crowded operating room.

In this document, I present the development of a compact and wearable goggle system capable of real-time sensing of both NIR fluorescence and color information. The imaging system is inspired by the ommatidia of the monarch butterfly, in which pixelated spectral filters are integrated with light sensitive elements. The pixelated spectral filters are fabricated via a carefully optimized nanofabrication procedure and integrated with a CMOS imaging array. The entire imaging system has been optimized for high signal-to-background fluorescence imaging using an analytical approach, and the efficacy of the system has been experimentally verified. The bio-inspired spectral imaging sensor is integrated with an FPGA for compact and real-time signal processing and a wearable goggle for easy integration in the operating room. The complete imaging system is undergoing clinical trials at Washington University in the St. Louis

Medical School for imaging sentinel lymph nodes in both breast cancer patients and melanoma patients.

Chapter 1: Introduction

The primary goal for image guide surgery (IGS) is to provide structural and/or functional information to the surgeon in clinical settings. Optical imaging techniques for IGS have been widely explored for real-time clinical imaging, including fluorescence imaging, two-photon imaging, polarization contrast imaging, and others. These imaging techniques allow for accurate assessment of tumor margins during surgical procedures as well as identification of secondary tumor sites that would otherwise be missed with the unaided eye.

Although optical imaging techniques have advanced rapidly in the last few years, they have not been widely integrated in clinical settings. For example, in melanoma and breast cancer surgeries, methylene blue (MB) dye is used to tag cancerous tissues [1]. A physician relies on his or her eyesight to determine the location of the tumor—which is demarked in blue due to the MB dye—and to evaluate tumor margins based on color contrast. Due to the low contrast between healthy tissue and cancerous tissue demarked by MB dye, about 20% to 70% of breast cancer patients will undergo a secondary surgery to remove additional tumor tissue [2]. Near-infrared fluorescence imaging can greatly overcome these limitations based on the following two factors: 1) deeper tissue imaging due to low scattering of NIR signals, and 2) combining visible spectrum with NIR fluorescence can seamlessly fuse both anatomical structures with segmented cancerous tissue [3][4]. Imaging sensors tailored for multi-spectral sensitivity can help surgeons identify cancerous tissue margins and reduce the necessity of secondary surgeries.

However, there are several reasons for the slow adaptation of optical techniques for IGS: 1) lack of optimized imaging sensors capable of simultaneously capturing fluorescence and visible spectrum signals, 2) lack of ergonomic display systems integrated with multispectral cameras that can be easily integrated in the surgical flow, and 3) lack of optimized signal processing algorithms for multispectral cameras for displaying real-time structural and functional information simultaneously overlaid on color information.

Instead of focusing on improving the imaging technology used for the IGS, which has been a vibrant research area for the last 10 years, I have taken a radically different approach by looking at imaging designs developed 500 million years ago. The design of the multispectral imaging sensor described in this thesis is inspired by the visual system— i.e., the ommatidia—of the monarch butterfly. The ommatidium of the butterfly, optimized over millions of years of evolution, monolithically integrates interference filters with light sensitive cells. Local, neighboring ommatidia have differently tuned spectral filters, allowing for multispectral imaging of the world [5]. The avoidance of pigmented spectral filters allows the imaging of multiple spectrums with area efficient filters. I borrowed the anatomic design of the butterfly's ommatidium and developed a compact and optimized multispectral camera capable of imaging both the near-infrared and visible spectrums simultaneously. Furthermore, this imaging sensor is coupled with an ergonomic and light weight goggle display for real-time display of information to the surgeon. Real-time signal processing algorithms—such as interpolation and calibration—for the proposed bio-inspired multi-spectral imaging sensor and bio-inspired polarization imaging sensor have been developed on both field programmable gate array (FPGA) and PC. I have also developed signal processing algorithms for a bio-inspired, spectral-polarization imaging sensors that can also be integrated with the fluorescence imaging in a clinical setting.

Specifically, in this dissertation I focus on the following three research areas:

1) Developing light-weight and ergonomic goggle display systems capable of real-time imaging of the visible and NIR spectrums with high spatial resolution. The imaging system is used together with the FDA approved NIR fluorescent agent ICG for sentinel lymph node tracking in human subjects and with the tumor targeted NIR probe LS301 for imaging tumor margins in murine models.

2) Developing a compact, high resolution, high sensitivity, and bio-inspired multi-spectral imaging sensor. The imaging sensor borrows key ideas from the monarch butterfly's visual system to realize a highly sensitive NIH fluorescent camera capable of imaging the visible spectrum with high spatial resolution. The opto-electronic performance of this bio-inspired sensor is compared to state-of-the-art off the shelf fluorescence cameras. This newly developed sensor can enable future bio-medical imaging applications that were not possible before, such as NIR fluorescence endoscopy.

3) Developing signal processing algorithms for a bio-inspired spectral and polarization imaging sensor. This new class of bio-inspired sensors warrants the development of custom signal processing algorithms to increase the accuracy of the captured visual information. In particular, I focused on evaluating interpolation algorithms for bio-inspired polarization imaging sensors as well as developing a comprehensive theoretical and experimental analysis to evaluate the performance of these algorithms. Interpolation and calibration algorithms for the bio-inspired multispectral imaging sensor were also developed and evaluated using a set of test images.

1.2 Contributions of this Dissertation

During the quest to answer the above outlined research questions, I have designed, developed, and tested imaging systems and applied these systems in clinical settings. Hence, the research contributions of this thesis are the following:

I have developed three custom NIR fluorescence imaging systems using CMOS imaging sensors and FPGA technology to achieve compact design, real-time imaging, and accurate multi-spectral information co-registration. I have evaluated these systems in terms of co-registration accuracy, fluorescence signal detectability, and sensitivity. These imaging sensors have been tested on both animal breast cancer models and human subjects.

I have developed a pixelated multi-spectral imaging sensor based on the anatomical structure of the monarch butterfly ommatidium. The ommatidium of the monarch butterfly, which is the single photo sensitive element in the ommatidia, elegantly combines spectral interference filters with light sensitive cells in a vertically stacking fashion. The spectral filters, known as tapetal filters, are implemented by stacking alternating low dielectric constant layers, such as air, with high dielectric layers, such as cytoplasm. Using nanofabrication techniques, pixelated spectral filters were designed, fabricated, and integrated with an array of CCD imaging elements. The imaging sensor allows for simultaneous and co-registered imaging of both visible and near infrared spectrum information. The electro-optical performance of the bio-inspired imaging sensor has been carefully evaluated and compared to other non-bio-inspired imaging sensors.

The proposed multi-spectral imaging sensor is integrated with a goggle display system for real-time display of fluorescence and visible spectrum information to the surgeon in a clinical setting. We used the proposed bio-inspired goggle system in both animal and human pilot studies to

evaluate the sensitivity and selectivity of the designed system. The system performance in terms of detectability, sensitivity, computational complexity, and overall system integration was compared to other imaging systems used for simultaneously imaging the visible and NIR spectrums.

I have developed and evaluated imaging processing algorithms for the proposed bio-inspired multi-spectral imaging sensor, as well as for the bio-inspired polarization sensor. The bio-inspired multispectral imaging sensor utilizes pixelated spectral filters distributed over the imaging plane. Hence, the spatial resolution is reduced, and the accuracy of the spectral imaging (visible and NIR) is compromised. The chief reason for this effect is the difference in the instantaneous field of view in neighboring pixels. Furthermore, variations in the interference filters at the nanoscale manifest drastic variations in the optical response across the imaging array to the same spectral target. To mitigate these effects, I have developed image interpolation and calibration algorithms for this bio-inspired sensor, and I have evaluated their effect on the spatial resolution of the imaging sensor, i.e. the modulation transfer function. I have leveraged my experience evaluating interpolation algorithms for bio-inspired polarization imaging sensors to evaluate the proposed algorithms for the bio-inspired spectral camera.

1.3 Organization of the Dissertation

The dissertation is organized as follows: Chapter 2 describes NIR fluorescence imaging systems developed using multiple imaging sensors and a comprehensive algorithmic approach to fuse the information from these sensors. The imaging systems have been tested for detectability and sensitivity, and they have been used to image breast cancer mouse models injected with a tumor specific NIR probe, LS301. Chapter 3 introduces an NIR fluorescence imaging system implemented using a division-of-amplitude approach. This imaging system relies on

miniaturized imaging sensor components and customized optics. The opto-electronic performance is closely evaluated, and data from animal and human pilot studies are presented. Chapter 4 presents details of the bio-inspired multi-spectral imaging sensor and corresponding imaging system; its concept and fabrication procedure are presented. The performance of the imaging system is evaluated in terms of opto-electronic response, imaging sensor calibration, and NIR fluorescence detectability and sensitivity. The proposed system was tested in a spontaneous breast cancer mouse model as well as a human pilot study for sentinel lymph node mapping for patients with breast cancer and melanoma cancer. Chapter 5 describes the imaging interpolation algorithms developed for both multi-spectral imaging sensors and division-of-focal-plane polarization imaging sensors. The performance of these interpolation algorithms is analyzed visually and analytically.

Chapter 2. Multi-Channel Camera Systems for NIR Fluorescence Imaging

2.1 Background

Identification and differentiation of tumor tissue from surrounding healthy tissue is a major issue and challenge during oncologic surgery today [6]. The surgeons have to rely on palpation and visual information to identify tissue that needs to be resected (such as cancerous tissue and lymph nodes) and tissue that needs to be preserved (muscles, nerves, blood vessels, etc.). The low visual and structural contrast between cancerous and healthy tissues can lead to two negative scenarios after surgery. First, the patient might be diagnosed with positive margins once the tumor tissue is resected. This diagnosis indicates that not all cancerous tissue has been removed from the patient; consequently, secondary surgery will have to be performed to remove the rest of the cancerous tissue. About 20% to 70% of patients with breast cancer will undergo a second surgery due to positive margins of resected tissue [2][7]. The second issue is damage to healthy tissue, such as nerves, muscles, blood vessels, and vital organs, which can lead to additional surgeries to repair the damage on healthy organs inflicted during the primary surgery. Both of these scenarios, that is, positive tissue margins and damage to healthy tissue, bring an unnecessary toll to the patient's health and inflict financial costs.

Image-guided surgery (IGS) aims to provide structural and functional information to the surgeon in clinical settings [8]. This additional information allows the surgeon to quickly and accurately identify the margins of the tumor tissue as well as the healthy tissue that should be absolutely preserved. Optical imaging techniques have played a major role in IGS. Among the various optical imaging techniques, fluorescence imaging has played a significant role in providing vital

information to surgeons. Exogenous and endogenous fluorophores can help produce high contrast between healthy and tumor tissue once excited with the appropriate wavelength. Near-infrared (NIR) fluorescence is of particular interest in IGS because of the following advantages: low auto-fluorescence, low tissue scattering, low tissue absorption in the NIR region, and imaging wavelength outside the visible spectrum[9]. The low auto-fluorescence in the NIR allows for background-free imaging, leading to high contrast between tumor and healthy tissue. The low scattering and low absorption of the NIR light allows for deeper imaging and the localization of tumor tissue in the range of several millimeters to a centimeter depending on the tissue surrounding the tumor. There are two FDA-approved NIR fluorescence dyes: methylene blue (MB) and indocyanine green (ICG) [10][11], which help identify tumor tissue due to passive accumulation. Since these fluorescent dyes emit light outside the visible spectrum, NIR fluorescence imaging does not impede or hamper the existing surgical flow or surgical light sources.

However, NIR fluorescence requires developing specialized imaging sensors, since the human eye cannot perceive these wavelengths. The fluorescence imaging system should be able to capture both visible spectrum information as well as NIR information, which are temporally and spatially co-registered. This will simultaneously provide both anatomical information (color image) as well as tumor localization (NIR image) to the surgeon for more accurate resection. Since silicon photo detectors (CMOS [12] and CCD) are sensitive to both the visible and NIR region, the same photo detectors can be used to acquire both image modalities, which can simplify the design of the entire imaging system.

NIR fluorescence imaging systems (NFISs) have witnessed rapid growth in the last decade in both research and commercial settings. NIR imaging systems, such as FLARE [13][14], SPY

[15], PDE [16], and others [17], are currently being used in several clinical settings on a daily basis. These systems combine two CCD imaging sensors, one for visible spectrum imaging and the second one for NIR imaging, with optimized dichroic beam splitters and spectral filters. Visual information from both imaging sensors is processed and displayed on a remote monitor, which creates discomfort to the surgeon when viewing this information and performing resection simultaneously. The footprint for these devices is typically large, and the high cost associated with these systems limits the dissemination of the systems. Minimally invasive surgical procedures, such as endoscopy [18] and laparoscopy [19][20][21], have also benefited from NIR fluorescence. Optimized NIR rigid probes have been used to simultaneously acquire fluorescence and visible spectrum information and to present this information on an overlaying monitor. These studies have been limited to animal models, with promising leads for clinical studies in the near future.

One of the main challenges for wide acceptance of these imaging systems is how information is presented to the health operator. A creative solution was proposed by Liu et al. [22], in which a head-mounted device, such as the goggle display devices typically used in the gaming industry, was complemented with camera devices mounted on the physician's head to acquire both NIR and visible information. The camera utilized time-multiplexed spectral filters to acquire NIR and visible spectrum images at different times, which caused mis-registration between the visual information from both spectrums due to movements of either the surgeon or patient. The large weight of the entire system also caused severe discomfort to the surgeon. Another imaging system was proposed by Shao et al. [23], in which multiple cameras placed in the operating room were used to create a single synthetic image, combining both NIR and visible spectrum

information. The low accuracy of the co-registration between the visible and NIR images was a major issue of the system and prevented accurate resection of the tumor tissue in animal models.

In this chapter, we present two compact and ergonomic fluorescence imaging systems with a goggle display for simultaneous imaging of NIR and visible spectrum information and for real-time display of fused information to the health professional.

The first system is a threshold detection based two camera system.[24] The imaging portion of the system is composed of two CMOS imaging sensors placed on a custom printed circuit board (PCB). Spectral filters are placed on both imaging sensors such that one sensor is optimized for visible spectrum imaging and the other sensor is optimized for NIR spectrum imaging. The signal processing portion of the system is performed on either an FPGA or a PC, where a synthetic visible-NIR image is computed. The display portion of the system is composed of a video see-through goggle system. The entire system also utilizes a custom-built NIR-visible spectrum tracking pod that allows for automatic co-registration of both images.

The second system is a feature matching based three camera system. This system has two color sensors to provide visible information and stereo vision, and one NIR sensor to capture NIR information. Using the scale-invariant-feature-transform (SIFT) feature matching based image overlay algorithm, disparity information between visible and NIR channels is derived by extracting the related disparity information between the two visible channels, which is computed by matching the same features existing in left and right scenes. The NIR-visible overlay information is projected on video see-through goggle system with stereo vision, which can offer potential depth information to the user.

The performance of the two NFISs is evaluated respectively in subsection 2.3 and 2.5. The system sensitivity and co-registration accuracy are presented as well as data from a small animal model. Finally, we discuss the advantages and limitations of the presented imaging system.

2.2 The System Setup and Image Overlay Algorithm for Two Camera System

2.2.1 Overview of System Setup

Figure 2.1 depicts the entire imaging system, which is composed of four distinct modules: (1) an image capture module, (2) an image processing module, (3) an image display module, and (4) a light source for simultaneous visible spectrum and NIR fluorescence imaging.

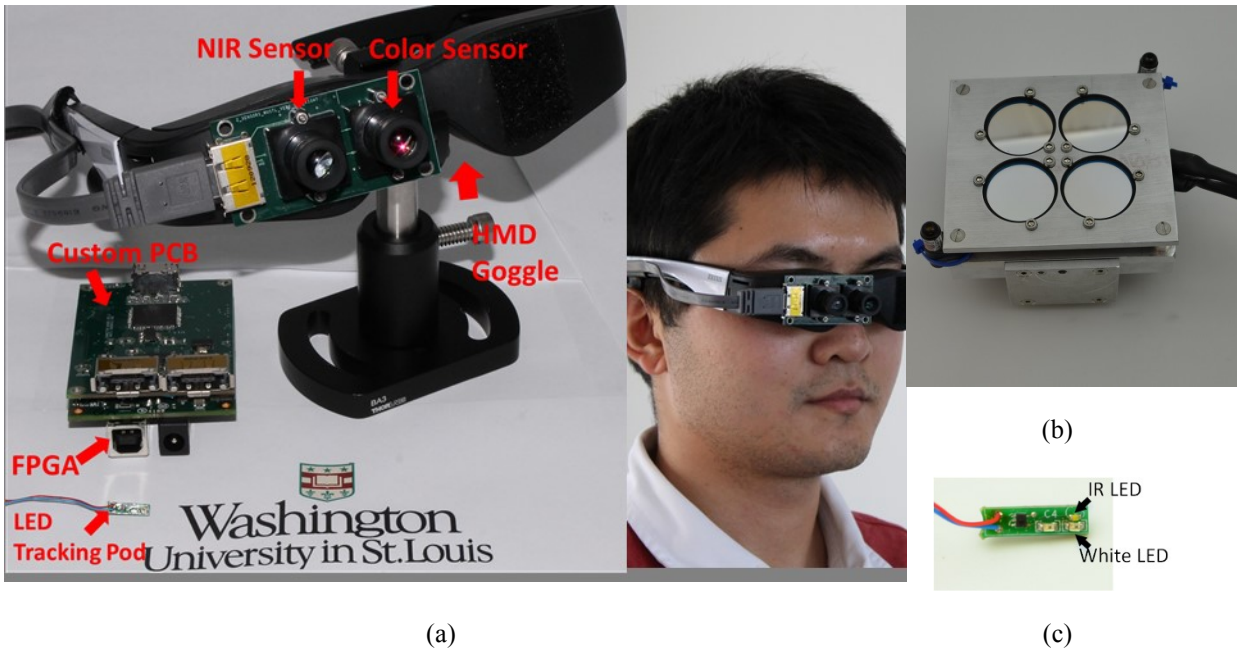

Figure 2.1. Dual-spectrum imaging system with a goggle display. (a) The imaging system is composed of two CMOS imaging sensors, long-pass and short-pass optical filters, an FPGA data acquisition and image processing board, and an HDMI goggle system; (b) a custom-built NIR LED illumination module; and (c) an NIR-visible spectrum LED tracking pod.

The image-capture module is composed of two CMOS imaging sensors (Aptina MT9V034) housed in a custom PCB. The custom PCB board ensures that the imaging sensors are placed parallel right next to each other, and the distance between the two sensors is minimal. Placing the

sensors close to each other ensures that the disparity between the two imaging sensors is small, and hence most of the imagers' field of view can be used to capture visual information. One of the CMOS imaging sensor has a color Bayer pattern, while the second CMOS imaging sensor is monochromatic. The Bayer pattern imager is used to produce a color image, and the monochromatic sensor is used to capture NIR information. The high quantum efficiency of 35% at 800 nm for the CMOS imaging sensor allows for efficient imaging of fluorescence signals in the NIR spectrum. Spectral filters are placed in front of the imaging sensors: a short-pass filter with a cutoff wavelength of 690 nm (Semrock FF01-694) is integrated with the Bayer pattern imager, while a long-pass filter with a cutoff wavelength of 785 nm (Semrock BLP01-785R) is integrated with the monochromatic imager. Two polymer-based objective lenses (Sunex DSL208 15.8mm F2.0) are used to minimize the weight and size of the complete imaging system. The weight of the entire system is ~50 g, and the size of the custom PCB is 1.5" by 1" (see Fig. 2.1).

The two imaging sensors operate in a master-slave configuration. This mode of operation allows for data to be sent from the monochromatic/NIR imaging sensor to the color imaging sensor via a two-line low-voltage differential signaling (LVDS) serial bus. The color imaging sensor then combines the data from both sensors and produces a single 16-bit word that contains information from both sensors (the lower 8 bits of data corresponds to the color imager and the upper 8 bits of data corresponds to the monochromatic/NIR imager). The 16 bits of data are serialized and sent via a two-line LVDS bus to the image processing module, hence minimizing the number of wires utilized to transfer data from both sensors.

The image processing module is composed of a custom PCB board, a FPGA, and an optional PC. The custom PCB board is designed to (1) connect with the two imaging sensors and provide easy scalability for additional imaging sensors, (2) mate with an FPGA board, and (3) connect to the

goggle display via an HDMI chip housed on the same custom PCB board. The connection between the imager board and the image processing board is accomplished via a custom eSATAp connector. This connector allows for eight independent signals to be transferred between two entities and three shielding wires. We utilize the eight signals as follows: two lines for LVDS image data from both cameras, two lines for the external exposure control signals of the two imagers, two lines for sending and receiving control signals to and from the imagers (such as exposure time, region of interest, gain of the signal, and others) via a serial protocol, and two power lines (ground and 3.3V). The shielding wires are grounded and used to shield the LVDS data signals from external noise sources. The serial data from the two imaging sensors is de-serialized in the FPGA (Opal Kelly 3050, Xilinx Spartan 3). The FPGA board can either transfer the de-serialized data to a PC via a USB 2.0 data link for image processing or execute the necessary image processing to provide a single combined NIR-visible spectrum image on the FPGA.

The image co-registration is accomplished via a software unit and a custom LED tracking pod. The LED tacking pod contains two bright and thin LEDs (Fig. 2.2). One of the LED is centered at 850 nm (Everlight HIR19-21C), and the second LED covers the entire visible spectrum (Rohm Semi., SMLP12WBC7W). The LEDs are placed next to each other. Due to their minimal form factors, the LEDs are virtually collocated when viewed at a 50-cm distance. This allows for both NIR and color cameras to observe a single point in both the NIR and visible spectrum, respectively. Since extra bright LEDs are utilized in the tracking pod, the location of the LEDs in both images corresponds to pixels with saturated values. Note that the assumption here is that the rest of the image in both the visible and NIR spectrum is not saturated. The image processing algorithm, which can run either on the FPGA or the PC (described in the next section), computes

the disparity between the NIR and visible spectrum images based on the tracking LEDs pods locations. An average disparity for the entire NIR image is computed when multiple tracking pods are utilized and applied on the entire image. A single combined image is computed by highlighting the pixel locations in the color image where NIR pixels values are above a user-defined threshold.

Since the FPGA is a compact device and can be easily carried in a pocket, the surgeon is free to move around the operating room, and the entire device does not impede the surgical flow. If the algorithm is executed on the PC, more optimization and advanced algorithms can be developed with significant time saving due to the easy implementation in the C++ programming language. Converting the same algorithm from C++ language to a hardware description language, such as Verilog or VHDL, is very time-consuming task. Furthermore, images and videos captured from the imaging sensor can be recorded on the PC, which is not possible on the FPGA implementation at this point. The shortcoming of using a PC for image processing is that the surgeon would be tethered to a computer, which would restrict his or her movement in the operating room.

The image display module is composed of an HDMI decoder chip housed on the custom PCB board and a goggle display device. The HDMI decoder chip receives display data from the FPGA and provides high-definition video data at 1080p to the display goggle unit. The state timing machine is optimized to display information on any device capable of handling HDMI input, such as LCD monitors, TVs, and projectors. We use a lightweight and ergonomic goggle display unit to display the final image to the health professional.

The illumination unit is composed for both NIR excitation and as a visible spectrum illumination source. The NIR excitation light source is constructed from 16 high-power 760-nm NIR LEDs (Roithner LaserTechnik H2A1-H760) covered with spectral band-pass filter centered at 769 +/- 20 nm (Edmund Optics 84-121). The optical power density at 70-cm working distance is measured to be 5 mW/cm2. The white light source is composed of a visible spectrum LED panel with an NIR blocking filter. The NIR blocking filter eliminates background signals when capturing the fluorescence image.

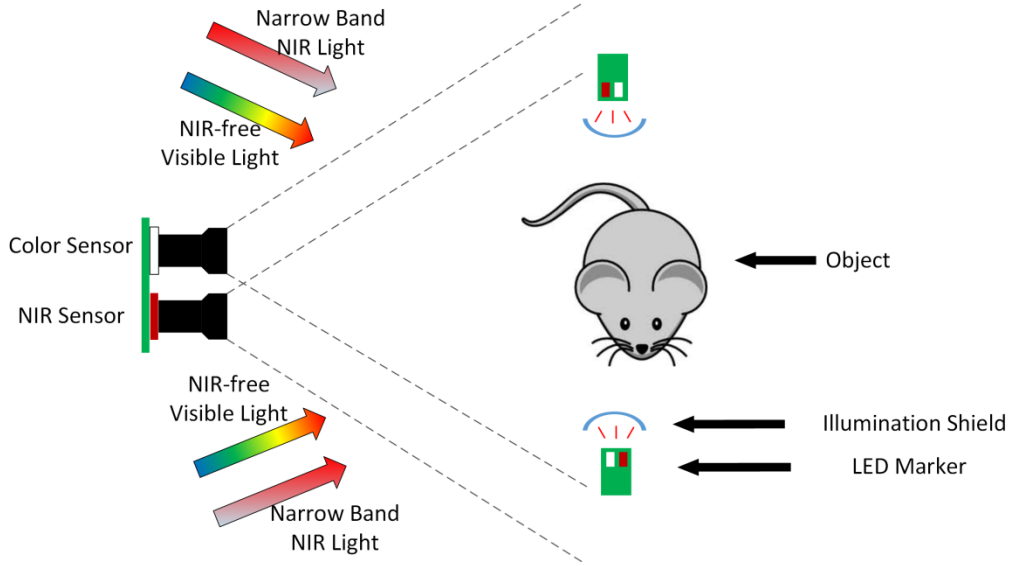

Figure 2.2. Block diagram of the NIR-visible imaging system. NIR-visible tracking pods are used to compute an average disparity between the two images. This disparity information is applied to the entire image to create a combined image in which the location of fluorescent data is highlighted on the color image data.

2.2.2 The Threshold Detection Algorithm with LED Tracking Pods

Accurate computation of the disparity information between the NIR and color image is of paramount importance when generating a combined NIR-color image. Mis-registration between these two images can create an incorrect assessment of the tumor location and can lead to both positive margins and damage to healthy tissue. In order to achieve high-precision overlay

images, the locations of the LED tracking pods in both images are used to compute the disparity information for the entire image. The complete disparity algorithm is depicted in Fig. 2.3.

The first step in this algorithm is calibrating both the NIR and color cameras. The main purpose of this step is to refer the NIR and color pixel's coordinates from the image planes (M) to a camera reference coordinate system (m) while taking into account the optical, geometrical, and digital characteristics of the camera. This is achieved by multiplying the pixel coordinates (x,y,1) with a 3-by-3 matrix A, as shown in equation (1).

Matrix A represents the intrinsic parameters of the camera, where (u_0, v_0) are the pixel coordinates of the principal point, α and β are the scale factors for the coordinate system, and γ is the skew of the two orthogonal image axes. In order to compute the intrinsic camera parameters, images are obtained in both the NIR and visible spectrum of a black-and-white checkerboard pattern obtained from different viewing perspectives.

$$\tilde{m} = A\tilde{M}, \text{ where } A = \begin{bmatrix} \alpha & \gamma & u_0 \\ 0 & \beta & v_0 \\ 0 & 0 & 1 \end{bmatrix} \qquad (2.1)$$

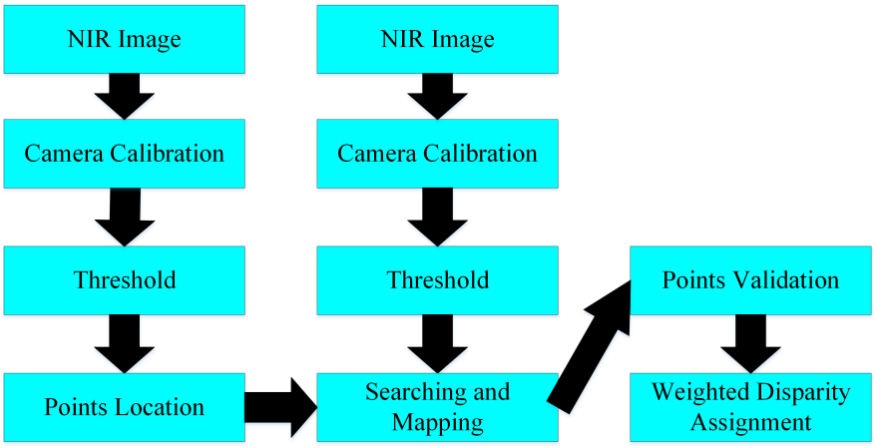

Figure 2.3. Flowchart of the disparity image processing algorithm using NIR-visible tracking pods. The algorithm is implemented on both FPGA and PC for real-time display of combined NIR-color images to the surgeon.

The next step in the image processing algorithm is to identify the location of the tracking pods in both the NIR and visible spectrum image. Since extra bright LEDs are used for the tracking pods, the pixels corresponding to the tracking pod LED will be saturated or will be close to saturation. Therefore, both NIR and color images use a threshold value corresponding to 95% of the dynamic range of the pixel. For example, since the maximum digital value of the pixel is 255, the threshold value is set to 232. It is important that the rest of the image is not saturated to prevent erroneous flagging of the tracking pod locations.

After the NIR and visible spectrum images are at the threshold, the locations of all pixels with values above the threshold are stored in separate lists for both spectrums. The locations of the pixels in the visible spectrum list are compared to the locations of pixels in the NIR list by performing a local search. The local search is limited to a pixel neighborhood of +/- 15 pixels. The pixel location is marked as a valid point if a saturated pixel is found in both images. Otherwise, the pixel location is removed from the list. Finally, after all the points are searched, the disparity information between the NIR and color images is computed based on the weighted disparity average shown in equation (2.2). Therefore,

$$\begin{cases} dx = (\alpha_1 dx_1 + \cdots \quad) / n \\ dy = (\alpha_1 dy_1 + \cdots \quad) / n \end{cases} \qquad (2.2)$$

Where n is the number of valid points, α_i is the coefficient of the distance ratio from the valid point i to the target pixel, dx_i is the horizontal disparity of the valid pixel i existing in NIR and color image, and dy_i is the vertical disparity for the valid pixel i in NIR and color scenes.

Since the NIR and visible spectrum images are placed next to each other on the custom PCB, translation accounts predominantly for the disparity between both the images generated from the sensors. Also, computing an average translation disparity between the two images is easily implemented on both FPGA and PC for real-time (27 fps) imaging. The disparity computation can be extended to include both an estimation of translation and rotation for a better and more accurate overlay between both images at the cost of higher computational complexity.

The disparity between the NIR and visible spectrum image is a function of depth. Since the two cameras view the same scene at different spectrums, stereo vision algorithms that estimate depth and therefore disparity cannot be used for this application. The LED tracking pods allow the same point in space to be viewed in both color and NIR images and hence estimate the disparity between the two images. The disparity information computed from the tracking pods has the highest accuracy at the depth where the tracking pods are located. Since the tracking pods are placed next to the subject that is imaged, part of the subject will be closer and part of it will be further away from the tracking pods, depending on the subject's 3-D structure. Hence, the disparity will be different across the imaging plane and will introduce error in the overlay image when a single (global) disparity metric is employed.

The disparity error estimation is illustrated in Fig. 2.4. In this figure, the square depicts the location of the tracking pods that are accurately determined via the image processing algorithm described in the previous section. A global disparity estimate is used for all pixels in the image based on the location of these LED pods. The circle depicts part of the scene that is further from the tracking pods, and the triangle depicts the part of the scene that is closer to the imaging camera. These three points in space at depths $D-\Delta D$, D, and $D+\Delta D$, will be projected to three different points on the imaging plane with different disparity ($2(l+x_1)$, $2l$, and $2(l-x_2)$). By

applying the triangular similarity theorem, a close form expression for the error estimate can be derived, as shown in equations (2.3 - 2.4). In equation (2.3), D is the distance between the sensor and the LED tracking pods, F is the focal length of the lens, d is the distance between NIR and visible sensor, and l is the distance between the targeted pixel and sensor center. Using equation (2.3), the relationship between the disparity error estimate and the target depth is shown in equation (2.4), where ΔD is the depth difference from the initial position D, and Δl is the corresponding distance change on one sensor pixel array. Under normal working distance, ΔD, d, and F are much smaller than D. Hence, error estimation, e, can be simplified to form a first-order linear relation with depth difference ΔD:

$$\frac{\frac{d}{2}+l}{D}=\frac{l}{F}\Rightarrow l=\frac{d}{2}\bullet F\bullet\frac{1}{D-F} \qquad (2.3)$$

$$e=2|\Delta l|=\frac{d\bullet F\bullet|\Delta D|}{(D-F)\bullet(D+|\Delta D|-F)}\approx\left(\frac{d\bullet F}{(D-F)^2}\right)\bullet|\Delta D| \qquad (2.4)$$

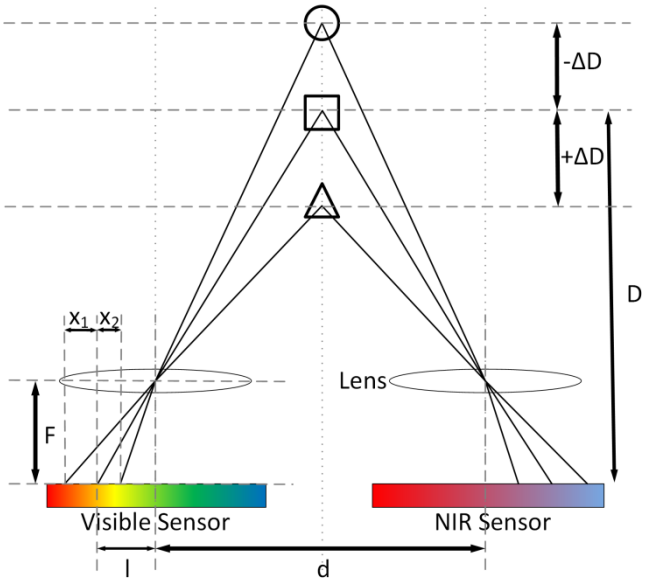

Figure 2.4. Disparity error estimate illustration.

2.3 Results of Threshold Detection based Two Camera System

The performance of the NIFS was evaluated under characteristic experiments and *in vivo* mouse model study. Characteristic experiments evaluated accuracy of threshold detection based camera system, and signal sensitivity of the NFIS. *In vivo* mouse model study validated the practicability of the NFIS and imaging overlay algorithms for image-guided application.

2.3.1 Disparity Error Estimation for Two Camera System

The disparity error between the NIR and color images is evaluated using a single tracking pod. The tracking pod is initially placed at either 45 cm or 65 cm to emulate two different working distances between the surgeon and the subject. The disparity at these working distances are computed and applied to all pixels in the image.

To emulate the fact that portions of the scene are closer or farther from the working distance, the tracking pod is moved +/- 6 cm from the working distance. Since the LEDs on the tracking pod are minimal in size, a single point in space emits both white light and NIR spectrum. The corresponding points of the LED tracking pods are determined from both images at different depths, and the disparity is computed. A disparity error measurement is computed by subtracting the global disparity at the working distance (45 cm or 65 cm) from the disparity of the tracking pod at various positions near the working distance (+/- 6 cm). The results are presented in Fig. 2.5.

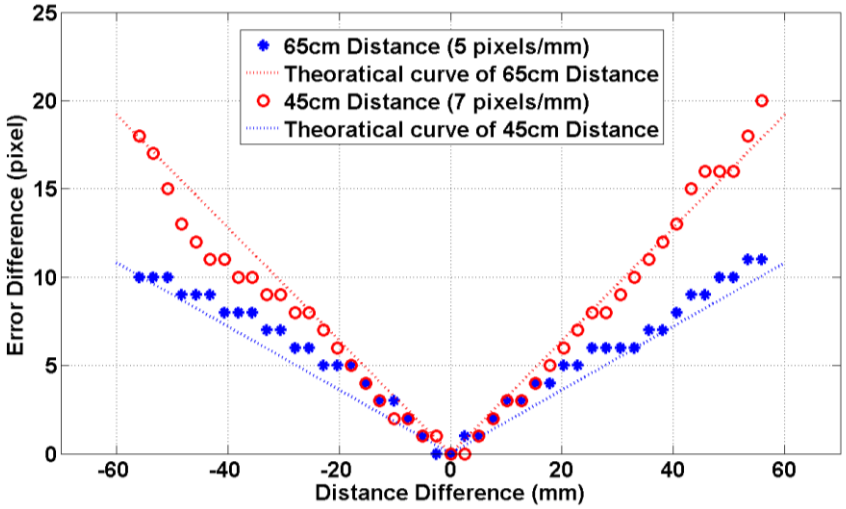

Figure 2.5. Disparity error measurement.

The measurements in Fig. 2.5 indicate that for a working distance of 65 cm, a maximum disparity error of 2 mm between the two images is registered at a distance of 6 cm away from the tracking pods. This error increases to 3 mm for a working distance of 45 cm at a distance of 6 cm away from the tracking pods. Hence, the tracking pods should be placed as close as possible to the location of the cancerous tissue that is being resected to increase the accuracy of the overlaid information.

2.3.2 Detectability

The detectability of the imaging system was tested by recording the NIR fluorescent signal responses for different ICG concentrations and different LS301 [22][25][26] concentrations dissolved in 100% dimethyl sulfoxide (DMSO). ICG has been widely used for NIR fluorescence since its FDA approval in the late 1960s. LS301 is a tumor-targeted contrast agent developed at Washington University in St. Louis and is currently under preclinical development. The vials with different ICG and LS301 concentrations are placed 50 cm from the imaging sensors. A control vial with DMSO is also imaged and denoted as a background signal. The NFIS was tested with its visible and NIR imaging sensors are operating at 27 FPS (i.e., a maximum exposure time of 30 ms). The exposure time for the color imaging sensor is typically around 1

ms due to the bright surgical LED light source. The NIR image sensor has a maximum exposure time of 30 ms to acquire the best SNR fluorescence signal. The diluted samples are illuminated with a 780-nm excitation light source, and two different optical powers (5mW/cm2 and 10mW/cm2) are used for the test evaluation. The mean and standard deviation of the signal-to-background ratio (SBR) of the imaging system is calculated from a 30-by-30 pixel region. The experiments are repeated with three different samples with the same ICG-DMSO and LS301-DMSO concentrations.

The detectability results of the NFIS are presented in Fig. 2.6. Figure 2.6(a) shows the signal intensity for different ICG and LS301 concentrations ranging from 500 pM to 50 uM. Higher illumination power increases the signal response from the same fluorescence sample. When the ICG and LS301 concentration are higher than a certain threshold (500 nM for ICG and 1 uM for LS301 under 10 mW/cm2 illumination; 1 uM for ICG and 10 uM for LS301 under 5 mW/cm^2 illumination), the fluorescent signal intensity exceeds the dynamic range of the imaging sensor. Hence, the imager output is saturated. Figure 2.6(b) shows the signal-to-background ratio (SBR) for the imaging system, where the vial with 100% DMSO is used as the background control negative sample. Defining the detectability of a system to be SBR = 2 [27], the imaging system can detect 25 nM of ICG and 30 nM of LS301 under 10 mW/cm^2. Using an excitation illumination of 5 mW/cm^2, the minimum ICG detectability is 30 nM and 40 nM for LS301. On the other hand, as seen in Fig. 2.6(b), the higher excitation power leads to lower SBR at higher concentrations, which occurs because the fluorescent signal is saturated while the background signal is higher. Therefore, selecting a proper optical power for the illumination module is always a tradeoff between keeping a high SBR and a high signal response.

Figure 2.6 also indicates that ICG achieves a higher signal response and SBR compared to LS301. The reason for this is that LS301 is a cypate-based contrast agent, which has lower quantum efficiency than ICG. Furthermore, as a tumor-targeted contrast agent, LS301 will clear out from most animal organs 24 hours after injection, which leads to a much higher fluorescent contrast in in vivo study. Hence, LS301 is used in our *in vivo* study in mice to further validate the performance of the imaging system.

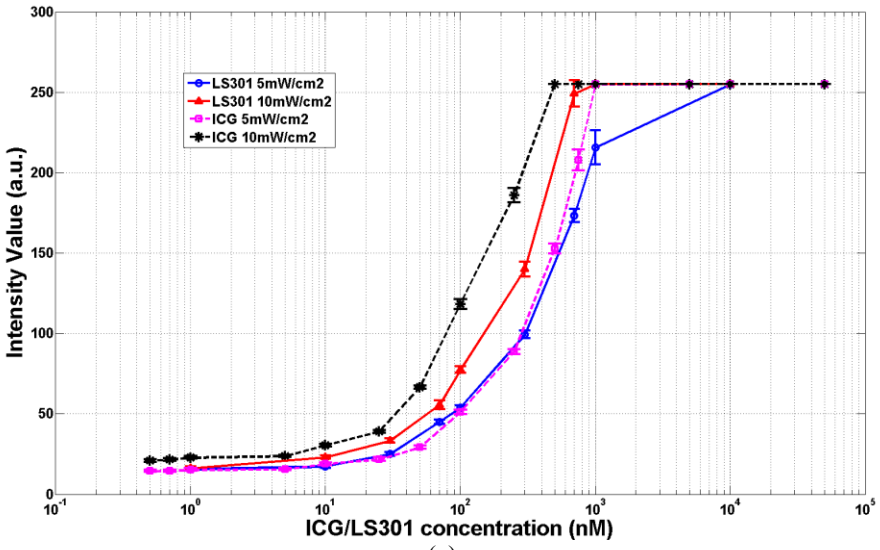

(a)

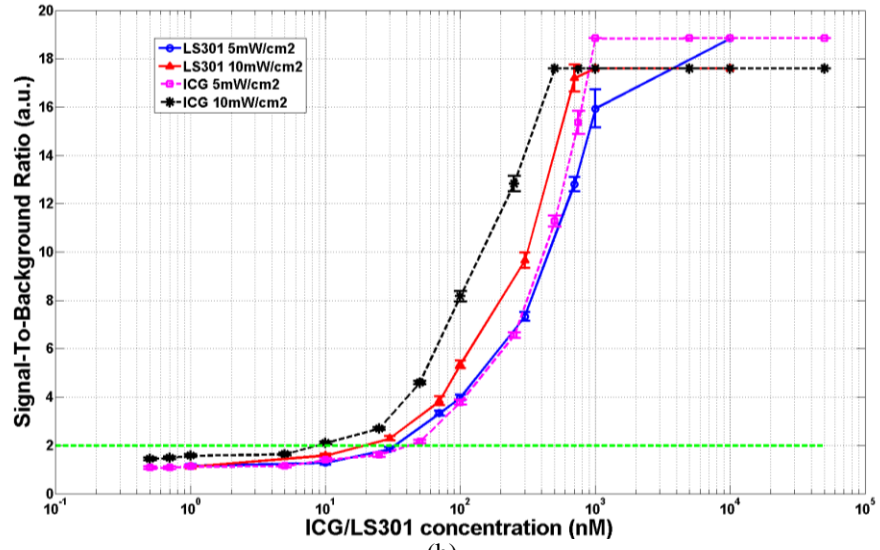

(b)

Figure 2.6. Detectability test using ICG-DMSO and LS301-DMSO, (a) Fluorescence signal response, and (b) signal-to-background ratio (SBR); green line shows the SBR = 2 threshold.

2.3.3 Sensitivity

Sensitivity of the NFIS solution was measured by using signal-to-noise ratio (SNR). SNR is the ratio of the signal response to the variation of the signal responses. Higher SNR represents better system sensitivity on distinguishing signal change. Since auto-fluorescence and background reflection commonly exist in tissues and bio-materials, it's important to eliminate their influence on signal response. Therefore, SNR is computed using equation (2.5), where the background mean intensity value B is subtracted from the mean intensity value S, and N represents the standard deviation of the signal response.

$$\text{SNR}=20 \bullet \log_{10}\left(\frac{S-B}{N}\right) \qquad (2.5)$$

In our experiment, sensitivity of the NFIS solution is measured by computing SNR of NIR fluorescent signal responses of different ICG concentrations in DMSO. S is the temporal mean value from ICG samples of different concentrations; and B is the mean value from the negative control sample of pure DMSO; the NFIS solution was setup at 50cm working distance, and 27 FPS (30ms exposure time). ICG-DMSO concentration samples were illuminated under two different illumination power (5 mW/cm^2 and 10 mW/cm^2).

Figure 2.7 shows the sensitivity results of the NFIS solution. Higher illumination power leads to slightly higher SNR. SNR difference under different illumination becomes smaller on ICG samples with higher concentration, since imaging sensor is approaching saturated, and less photon can be collected by the photodiode. SNR measurement shows that SNR of the NFIS solution can achieve more than 15 dB when ICG concentration is above 10nM, while the system

is running at 24 FPS. The 15dB SNR result is much higher than the confidence level of a normal signal distribution, which is defined to be 6dB for 95%, and 9.5dB for 99.7% [28].

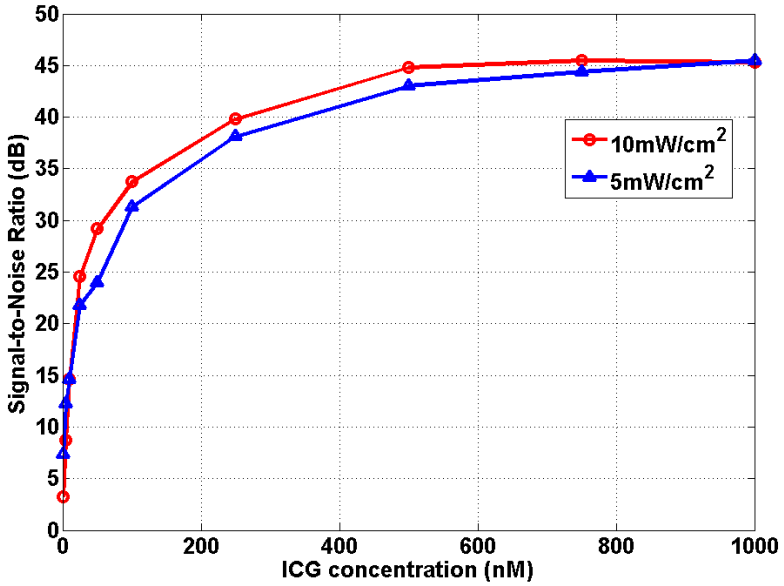

Figure 2.7. Sensitivity Test with SNR measurement using ICG.

2.3.4 *In Vivo* Study in Mice

The NFIS was validated through *in vivo* studies using a subcutaneous breast cancer mouse model. Four-to-six-week-old BalbC mice were given subcutaneous flank injections with 100,000 4T1Luc murine breast cancer cells. When the tumors were at least 10 mm in size, the mice were injected with 10 µl of 60 uM tumor-targeted NIR fluorescence contrast agent LS301, via the tail vein. Images were taken 24 hours post injection of LS301. During *in vivo* study, the image-capture module was set up at a 50-cm working distance, and the illumination module was placed at a 50-cm distance. All images were captured at 27 fps. During the imaging experiments, the mouse was kept anesthetized using a cocktail of ketamine/xylazine or through intubation of isofluorane. Following the imaging experiment, the mouse was sacrificed through cervical dislocation, and its organs were harvested, imaged, and preserved for histologic evaluation.

In Fig. 2.8, the mouse object and the LED tracking pod are placed in the same scene. Figure 2.8(a) presents the NIR image mapped using a false color map, demonstrating that the system can detect in vivo fluorescent signals from the tumor areas. A threshold value of 38 has been assigned to eliminate the background signal. Figure 2.8(b) presents the color image captured by the visible sensor. Without the disparity cancellation algorithm, the NIR and color images have a large disparity error, as shown in Fig. 2.8(c). Figure 2.8(d) depicts the final NIR-color image after the disparity algorithm is applied using the tracking LED pods. The tumor areas are clearly highlighted on the color image and accurately demarked after close visual evaluation of the final image.

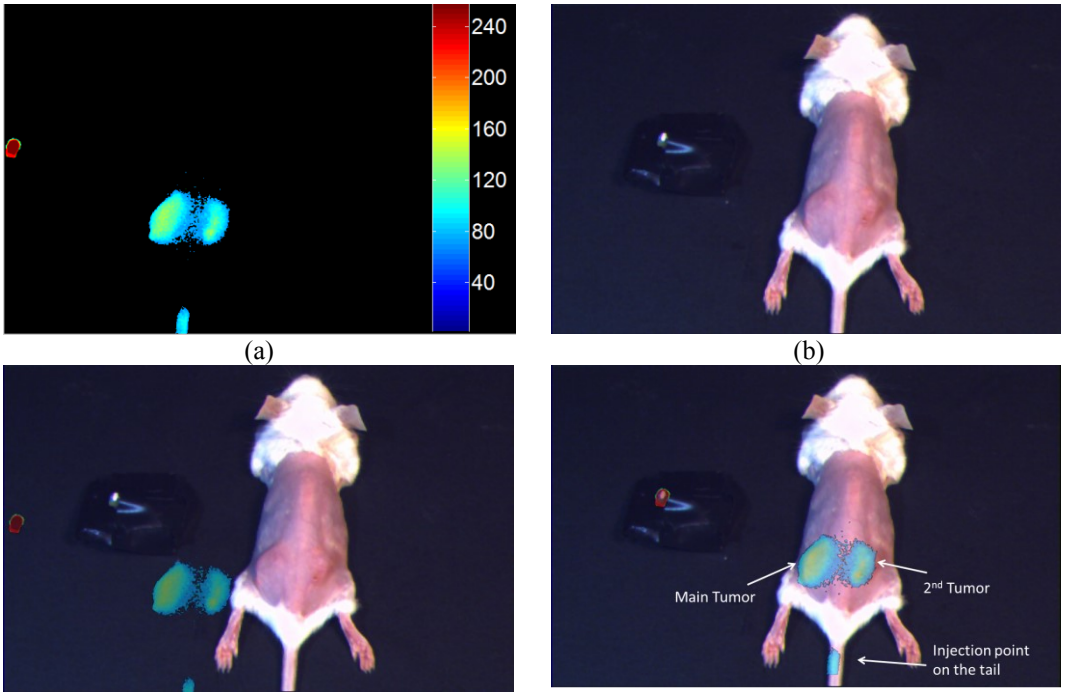

(a) (b)

(c) (d)

Figure 2.8. Mouse study test result: (a) NIR channel image, (b) visible channel image, (c) pre-disparity correction image, and (d) corrected image using a threshold detection algorithm.

Figure 2.9 shows the results of the same mouse object when the skin is deflected to reveal the tumors. The tracking LED pod allows for an accurate estimate of the disparity between the NIR and color image. The tumors are accurately highlighted in the final color image.

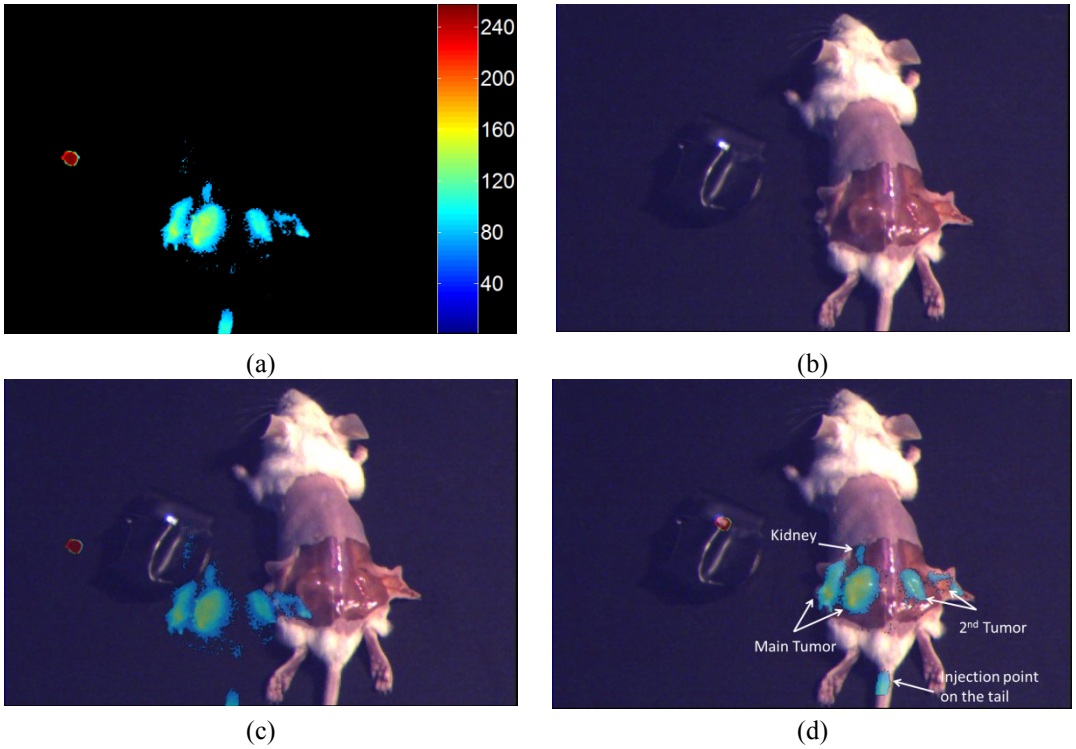

(a) (b)

(c) (d)

Figure 2.9. Mouse study test result (open skin): (a) NIR channel image, (b) visible channel image, (c) pre-disparity correction image, and (d) corrected image using a threshold detection algorithm.

2.4 SIFT Feature Matching Based Three Camera System

2.4.1 Overview of System Setup

The SIFT feature matching three camera system is shown in Fig. 2.10. The system is composed of four distinct modules: 1) an image capture module; 2) an image processing module; 3) an image display module; and 4) an illumination module.

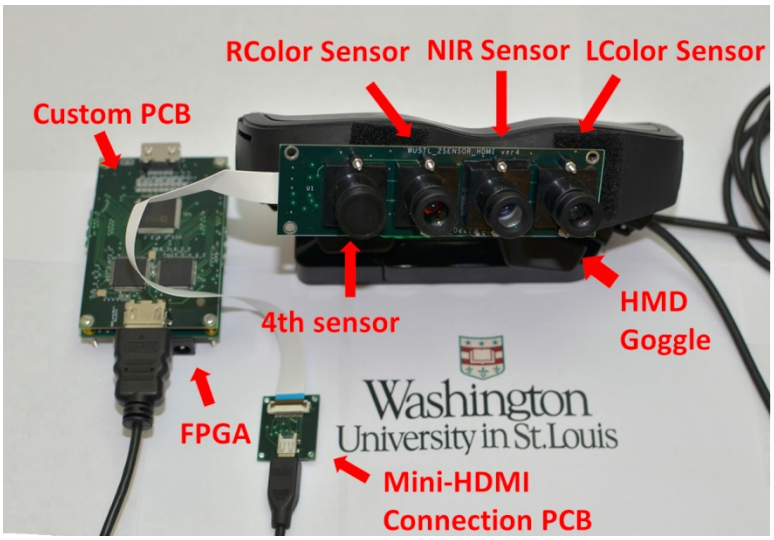

Figure 2.10. SIFT feature matching based three camera NFIS.

The image capture module is composed of three XVGA (753x480 pixels) CMOS imaging sensors (Aptina MT9V034) housed parallel in a custom PCB. From left to right, the three sensors utilize image data capture on visible, NIR, visible channels respectively. The center NIR sensor (Aptina MT9V034 monochrome type) is integrated with a high optical density (OD) long-pass filter (Semrock BLP01-785R). The high quantum efficiency of 35% at 800nm for the CMOS imaging sensor allows for efficient imaging of fluorescence signals in the NIR spectrum. Two color sensors (Aptina MT9V034 color type) on left and right (named as Lcolor and Rcolor) are integrated with high OD short-pass filter (Semrock FF01-694). Each sensor has a fixed 26mm distance from its neighbor(s), where NIR sensor locates at the middle point of the two visible sensors. Three S-mount 15.8mm miniature lens (Sunex DSL208) are used to reduce the weight and size of the whole imaging capture module. A mini-HDMI connector is used to transmit image data. The utilization of all 19 pins are as follows: 4 lines for LVDS data transmission, 4 lines for control commands transmission, 2 lines for exposure control, 4 lines for power supply

and 5 lines for ground and shielding. The whole module weights ~80g and occupies 10.5 cm x 3 cm space.

The three imaging sensors form two master-slave configurations. This type of configuration allows two sensors to bundle their 8 bits output data into a 16 bits output data in low-voltage differential signaling (LVDS) format, which only requires 2 signal wires to transfer up to distance of 10 meters. Hence, the imaging data from the three sensors use only 4 wires to transfer the data to the image processing module. In the image capture module, NIR sensor data is combined with one viable sensor data, while the other visible sensor data is bundled with the data from a "dummy" sensor (shown in Fig. 2.10), which could potentially serves as the 4th imaging sensor in future systems.

The image processing module is a combination of a custom PCB board for FPGA connection, a field-programmable gate array (FPGA) application board and a PC. The custom PCB is designed for image sensor connection, power supply, FPGA connection and possible HDMI output to a goggle display unit. Image data from the 3 sensors forms two 16 bits serial data flow in LVDS data format. The incoming image data is then de-serialized in the FPGA board (Opal Kelly 6310, Xilinx Spartan 6). The FPGA board features large memory (128 MB DDR2) and fast transmission interface (USB 3.0 port, update 200 MB/s). Hence, it realizes the real-time image data buffering and transmission to a PC for post processing.

The image display module is composed of an HDMI decoder chip located on the custom PCB board and a goggle display device. The HDMI decoder chip converts parallel data from FPGA into HDMI format for device display. Our timing state machine enables display on any device

with HDMI input capability, such as LCD monitors, HDTV and projectors. A light weight and ergonomic goggle display unit (Zeiss Cinemazer) is used for easy wearable devices.

The illumination unit is composed of both NIR and visible spectrum light sources, which was introduced in subsection 2.2.1[29].

2.4.2 Disparity Correlation

The illustration of the disparity correlation among the three imaging sensors is shown in Figure 2.11, the two color sensors (L_{Color} and R_{Color}) have the same distance *d/2* (26mm) from the center NIR sensor. Assume the distance between target and sensor plane is D_{depth}, focal length of lens is *f*, and the relative distance between the sensors and the target mapping on the sensor plane is d_1, d_2, and d_3, respectively. The geometry relation of horizontal disparity $H_{Diparity}$ and D_{depth} is shown in equation (2.6) by applying triangular similarity theorem. The symmetric structure provides horizontal disparity of L_{Color}-NIR sensor pair to be exactly the half value of horizontal disparity of L_{Color}-R_{Color} sensor pair by following equation (2.7), if all the sensors are aligned in the proposed locations. Therefore, by computing horizontal disparity information of L_{Color}-R_{Color} sensor pair, the corresponding disparity information of L_{Color}-NIR sensor pair can be solved. Furthermore, since the two color sensors with 52mm interval achieves similar pupil distance of human adult, it enables stereoscopic view by displaying L_{Color}-NIR super-imposed scene and R_{Color} scene on the left and right eyepieces of head-mount-display (HMD) goggle respectively. Hence, depth information of visible channel is supplied to surgeons.

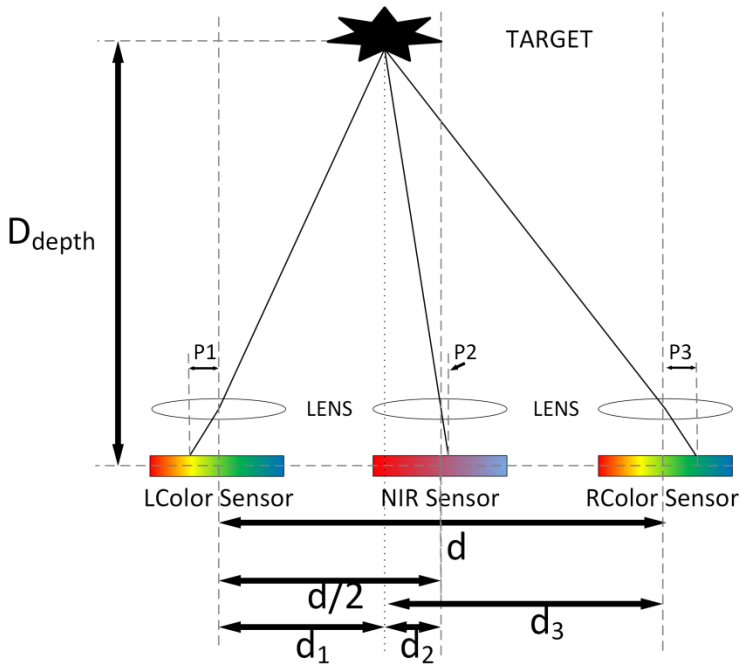

Figure 2.11. The block view of sensor system structure.

$$\begin{cases} \dfrac{p_1}{f} = \dfrac{d_1 + p_1}{D_{depth}} \\ \dfrac{p_2}{f} = \dfrac{d_2 + p_2}{D_{depth}}, \\ \dfrac{p_3}{f} = \dfrac{d_3 + p_3}{D_{depth}} \end{cases} \text{ where } \begin{cases} d_1 + d_2 = d/2 \\ d_1 + d_3 = d \end{cases} \tag{2.6}$$

$$\begin{cases} HDisparity_{LColor-NIR} = p_1 + p_2 = \dfrac{(d_1 + d_2) f}{D_{depth} - f} \\ HDisparity_{LColor-RColor} = p_1 + p_3 = \dfrac{(d_1 + d_3) f}{D_{depth} - f} \end{cases} \Rightarrow HDisparity_{LColor-NIR} = \frac{HDisparity_{LColor-RColor}}{2} \tag{2.7}$$

The three camera NFIS also offers simplified optical setup with no dichroic optics to maintain the identical field of view between NIR and visible sensor. Thus, the incoming fluorescent and visible signals suffer less attenuation before reaching imaging sensors, which benefits on much higher signal intensity for both visible and NIR channels, and increase the sensitivity of the

imaging system as well as the frame rate of video capture flow. Conversely, as a tradeoff, imaging overlay becomes a big problem for the SIFT feature matching NFIS solution, because large horizontal position differences exist among difference sensors. Therefore, we propose a SIFT feature matching scheme based image overlay algorithm to establish accurate, tool-free image overlay.

2.4.3 SIFT Introduction

SIFT feature detection and description method was developed by Lowe [30], and it has been widely used in computer vision domain. Lots of applications [31][32][33] have shown that SIFT performs robustness in dealing with vision problems such as translations, rotations, and scaling transformations, which makes it useful for image matching and object recognition.

$$H = \begin{bmatrix} D_{xx} & D_{xy} \\ D_{xy} & D_{yy} \end{bmatrix} \tag{2.8}$$

$$\text{Ratio} = \frac{Tr(H)^2}{Det(H)}, \text{ where } \begin{cases} Tr(H) = D_{xx} + D_{yy} \\ Det(H) = D_{xx}D_{yy} - (D_{xy})^2 \end{cases} \tag{2.9}$$

SIFT feature detection uses the Harris matrix functions shown in equation (2.8), the principal curvature is computed from 2x2 Harris matrix *H*. By computing the ratio of the trace of *H* to the determinant of *H*, the feature point can be detected if the ratio (shown in equation (2.9)) is below certain threshold. Gaussian smoothed image is used to compute the gradient magnitude and the gradient orientation. Therefore, the SIFT feature detection is scale-invariant and rotation-invariant.

SIFT description collected the orientation distribution histogram of intensity gradient vectors in four quadrants of the target feature point neighborhood (shown in Fig. 2.12). It creates

orientation histograms over 4x4 sample region, and samples significant shift in gradient positions. In Fig. 2.12, it shows eight directions for each orientation histogram, with arrow length representing the magnitude of that histogram entry. In our application, for each feature point, 4x4 local quadrants are selected. Hence, the SIFT descriptor uses 4x4x8=128 element feature vector to describe each feature point. And in order to increase the illumination immunity, the vector is normalized to unit length.

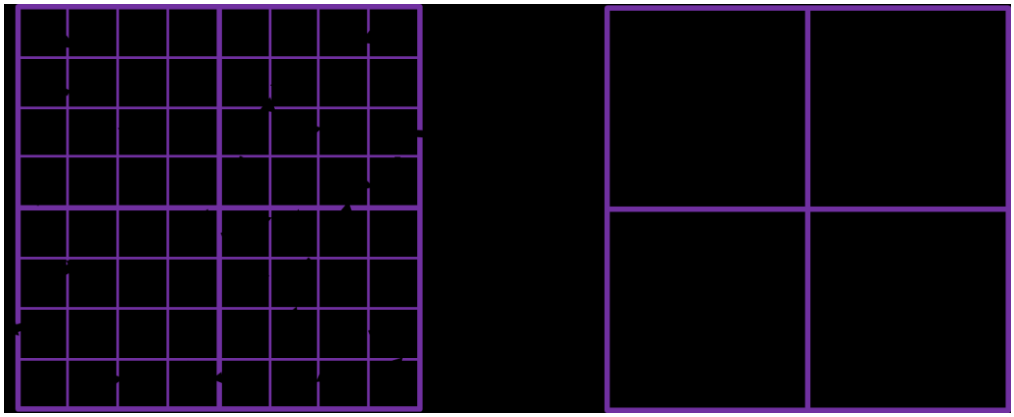

Figure 2.12. SIFT description kernel, (a) gradients map of 16 pixels in a quadrant, (b) histogram of the four quadrants as an 8-vector plot.

After the SIFT features are collected from the image scenes of the two color sensors, a RANSAC based feature matching algorithm is implemented to pair the features in the two color channels. A threshold is set to distinguish the inliers from outliners. The horizontal disparity is then computed based on the coordinate difference of each matching feature pair. Different disparity results are saved in a list, and sorted by descending order of the number of matching pairs for each disparity result. Which means on the top of the list, the disparity information is shared by the largest group of matching pairs; while at the bottom of list, the disparity information is only shared by few matching pairs. After the disparities of all the matching pairs are computed, the disparity information is computed as the average of the top three disparity results stored in the

list. Finally, the disparity between NIR and L_{Color} imaging sensors are derived by following Equation (2.7).

2.4.4 Image post-processing and SIFT Implementation

The SIFT feature detection and description algorithm is implemented with image post-processing and display using C++ OpenCV library. The complexity of the SIFT causes slow processing speed on each image frame. Our test shows that the SIFT feature based disparity computation can only run at 5-6 frames per second, which is much slower than the requirement of 27 frame per second real-time video rate. To keep the slow SIFT processing speed from affecting real-time video rate display, a multi-thread based code scheme is implemented in C++ to take advantage of the multi-core and parallel processing features of CPU. As shown in Fig. 2.13, the C++ code is running in three threads. The main thread executes raw data capture from FPGA, and offers real-time video recording function; the sub-thread 1 is the display thread, which is responsible for image post-processing such as image interpolation, color correction, etc.; the sub-thread 2 is the disparity computation thread, which includes SIFT based image overlay algorithm. The pre-processed color images are sent into sub-thread 2 for SIFT feature matching, and disparity information is returned to sub-thread 1 to adjust image overlay of NIR-LColor images. To further accelerate disparity computation step, the source image is decimated by half of its resolution for faster feature detection. Meanwhile, feature detection is limited to only within a regional pixel array (200x100 pixels array) because of fixed position correlation between the two color sensors.

Running under the multi-thread scheme, though the disparity computation is executed at a slower speed, it doesn't affect the real-time image display rate. In our current implementation, the disparity information update runs at 5-6 frames per second (FPS), while image display has frame

rate of 27 FPS. The exposure time of each NIR frame and color frame is 30 ms at 27 FPS frame rate, additional overhead time is caused by external global shutter mode with full pixel array readout for each frame (~18ms overhead).

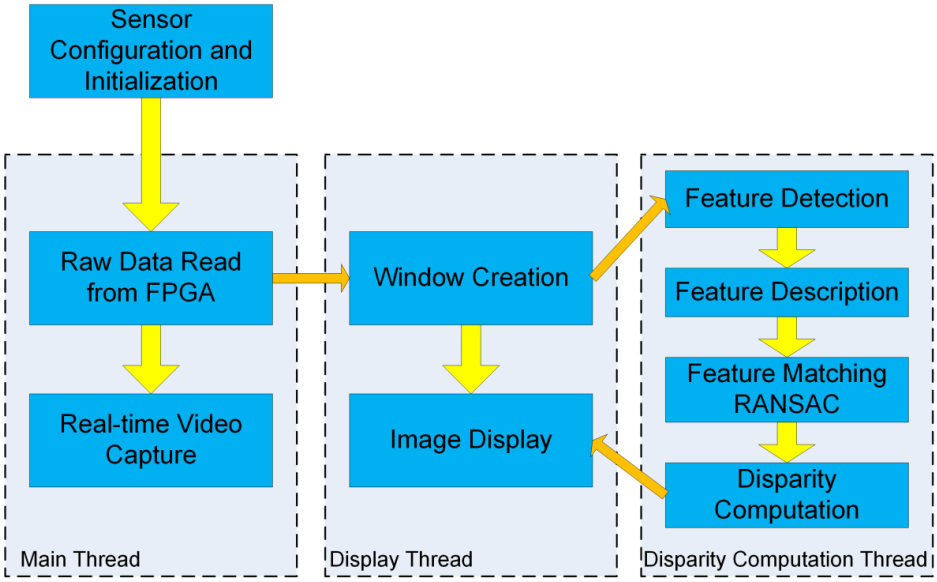

Figure 2.13. Multi-threads based code implement scheme.

2.5 Results

The performance of the near infrared imaging systems was also evaluated under characteristic experiments and *in vivo* mouse model study.

2.5.1 Accuracy Measurement of Feature Matching Based Three Camera System

Disparity information will alter along the depth change between image capture module and experimental object during open surgery process. It is important to understand the accuracy of disparity information recorded by the NFIS solution and SIFT algorithm. However, in *in vivo* animal study, the depth information of features from animal body is hard to precisely measure. Thus, we use a printed open-skin mouse image to emulate the real feature on mouse body, while the gel-form ICG sample is added on top of the tumor region of the mouse to supply fluorescent signal. By taking both visible and NIR co-registered image, the disparity information in both x

and y axes supplied by SIFT image overlay algorithm are collected at different working distances (30-70cm). The printed image board was setup under 5mW/cm2 illumination using a 780nm CW laser diode (B&W TEK Inc., BWF2-780-0.8), while the camera module is running at 27 FPS.

Figure 2.14 shows the disparity error between the complete imaging overlay result and SIFT feature matching result in both X and Y axes. Based on the test, the SIFT based image overlay algorithm can well maintain the error within 1-2 pixels in both X and Y axes at the setup working distance (30-70 cm), which corresponds to 0.2-0.4mm. Hence, the NFIS and SIFT image overlay algorithm is qualified for intraoperative operation.

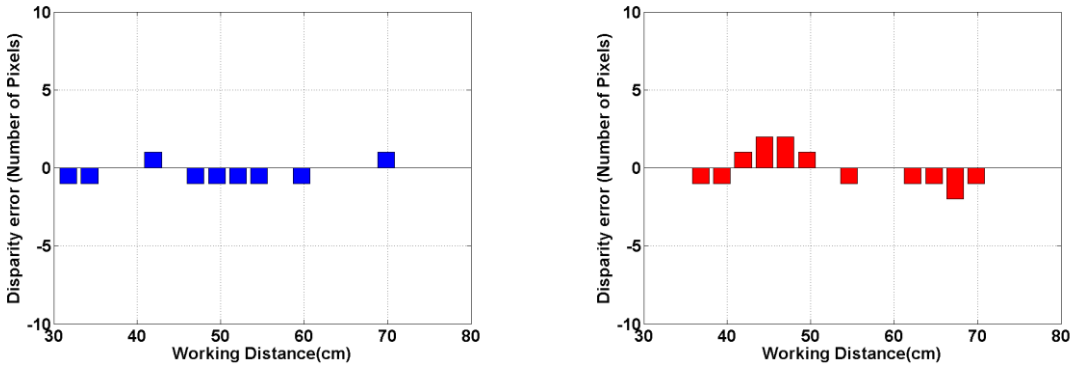

(a) (b)

Figure 2.14. Disparity error results of SIFT based imaging overlay algorithm, (a) horizontal disparity, and (b) vertical disparity.

2.5.2 Detectability and Sensitivity

Since both camera systems have the same optical setup and imaging sensors, the feature matching based three camera system have the same detectability and sensitivity results as the previous two camera system. The detectability test using SBR and sensitivity test using SNR for the three camera system are shown in Fig. 2.15. As shown in Figure 2.15, the NFIS can detect down to 25 nM of ICG and 30 nM of LS301 under 10 mW/cm^2, and its SNR can achieve 15 dB when ICG concentration is higher than 10 nM.

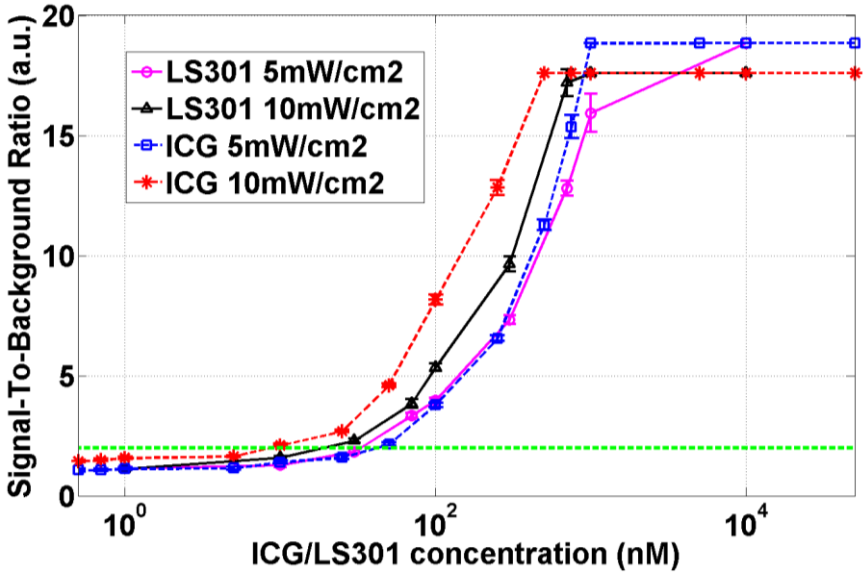

(a)

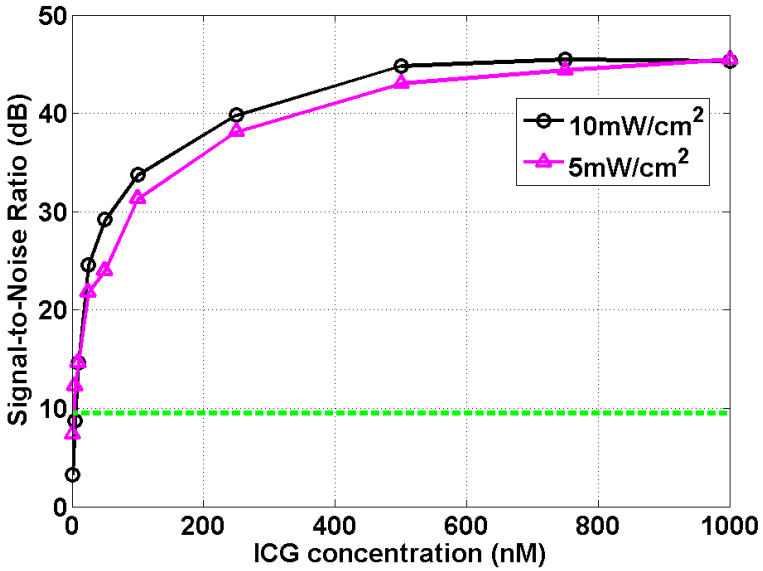

(b)

Figure 2.15. Detectability and sensitivity testing results, (a) SBR of three camera system, and (b) SNR of three camera system.

2.5.3 *In vivo* study in mice

The same mouse object, mentioned in subsection 2.3.4, was also used to evaluate feature matching based three camera NFIS. Figure 2.16 shows the test results of the mouse object. Figure 2.16(a) is the NIR channel image mapped to JET color map. The major tumor and the 2nd tumor were clearly detected in NIR channel. Figure 2.16(b) is the visible image from the left color channel image. The SIFT matching result are shown in Fig. 2.16(c), where blue dots in

both scenes are the feature points detected by SIFT and green dots with line connection are the matching pair inliers found by RANSAC matching algorithm. Without the SIFT feature matching method, large disparity error exists between NIR-color images, as shown in Fig. 2.16(d), the NIR channel information cannot supply meaningful overlay information for user to locate tumors. With the SIFT feature matching method, as shown in Fig. 2.16(e), the NIR channel information is well superimposed with visible information.`

Figure 2.17 shows mouse with deflected skin for tumor identification. Figure 2.17(a) and (b) show the NIR channel and LColor channel images, respectively. The SIFT matching result is shown in Figure 2.17(c). Figure 2.17(d) and (e) are image overlay results without SIFT / with SIFT respectively. The main tumor, 2nd tumor and their residual parts on the mouse skin are shown clearly in Fig. 2.17(e), Mouse kidneys are also highlighted in NIR channel, but they are considered to clear out in regular fluorescence animal study [34].

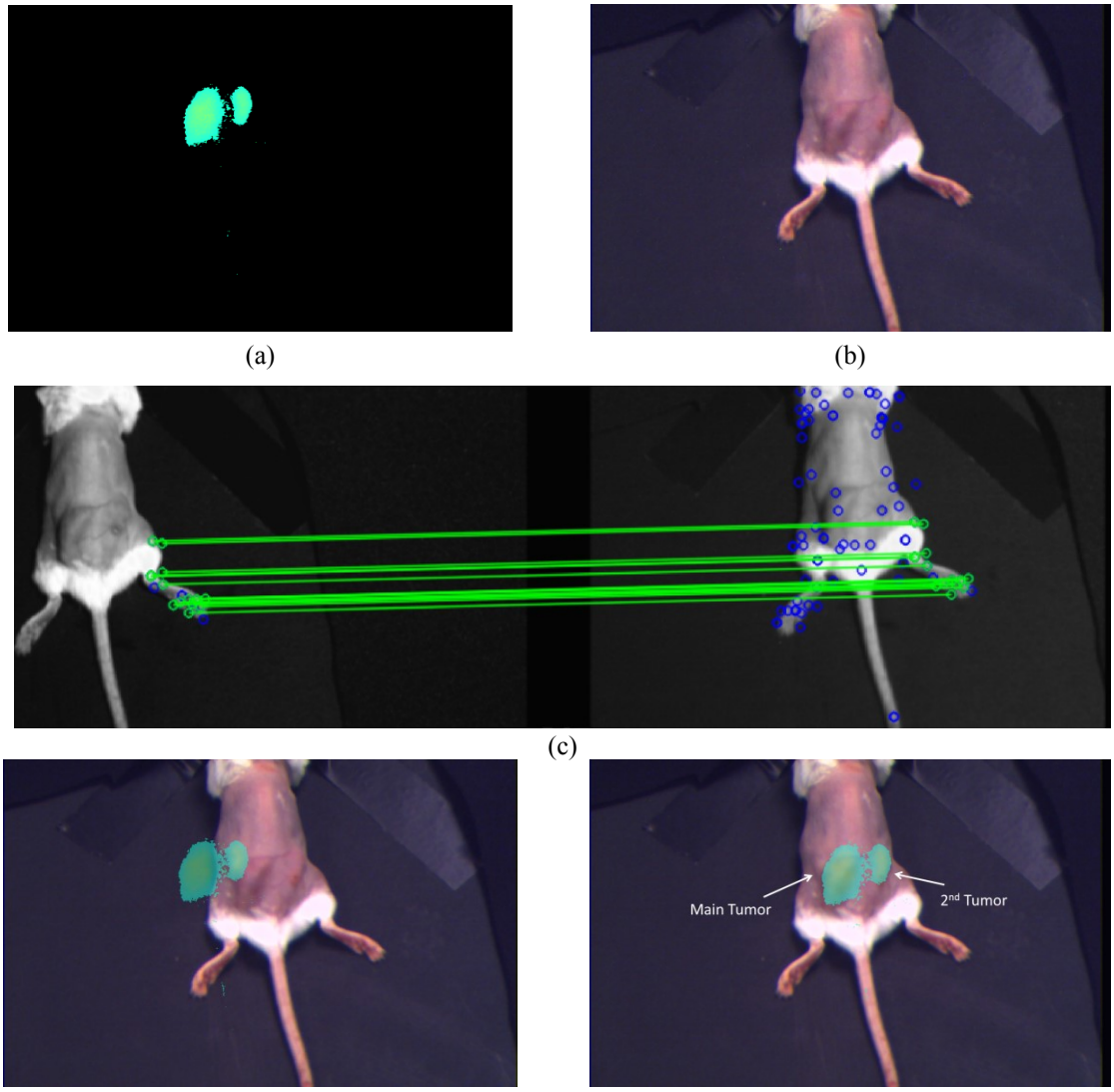

(a) (b) (c) (d) (e)

Figure 2.16. Mouse study test result, (a) NIR channel image, (b)Visible channel image, (c) SIFT matching result, (d) Pre-disparity correction image, and (e) Corrected image using threshold detection algorithm.

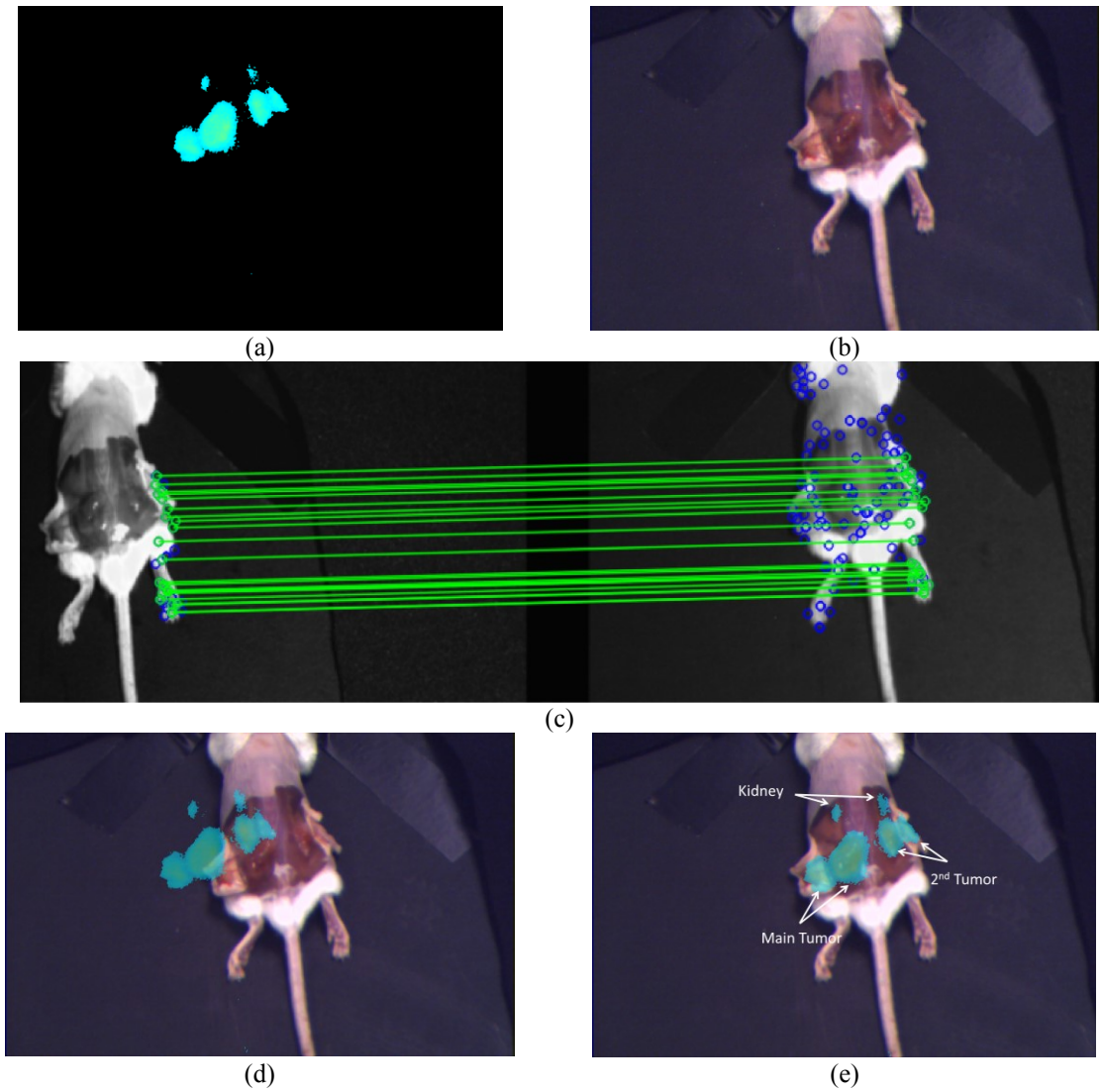

(a) (b) (c) (d) (e)

Figure 2.17. Mouse study test result (Open skin), (a) NIR channel image, (b)Visible channel image, (c) SIFT matching result, (d) Pre-disparity correction image, and (e) Corrected image using threshold detection algorithm.

2.6 Discussion

With the rapid growth of intraoperative image-guided procedures, the development of NIR fluorescence imaging system presents an important tool for assisting surgeons to better locate tumor margins and increase the success rate of tumor excision. Concurrently, research advances in NIR fluorescent contrast agents encourages the development of imaging systems optimized for NIR fluorescence imaging. These developments reflect potential advantages of having NIR fluorescence imaging for intraoperative image guidance. Considering the needs for surgical

procedures in the operating room, the fundamental design principles for NIR fluorescence imaging should be fluorescent signal detection with high sensitivity, real-time feedback, compactness, and hands-free features. Highly sensitive fluorescence detection will assist surgeons in accurate tumor resection and minimize the positive margins issues. Moreover, real-time image processing and display of information offers immediate feedback to the surgeon in the operating room. The compactness of the imaging system will also allow easy incorporation in the "already crowded" operating room setup and not hinder normal surgical operation. Additionally, the hands-free feature eliminates the interruption and distraction caused by frequent switching between using a scalpel and adjusting the imaging system by the surgeon. Most existing NIR fluorescence imaging systems employ a complex optical and electronic setup to guarantee the high sensitivity of fluorescent signal detection with real-time feedback. Conversely, few of them consider the great convenience brought by compactness and a hands-free feature. These limitations prevent these systems from being widely used in operating rooms worldwide for open surgery.

Correspondingly, in this chapter, we present two compact NIR fluorescence imaging systems with an ergonomic goggle display system. By using the threshold detection image overlay solution and CMOS imaging sensors, the camera module of the imaging system achieves a small footprint and light weight, while keeping high sensitivity at real-time frame rate. The threshold detection algorithm and miniature LED tracking pods are implemented to replace a complex and heavy dichroic optical setup so that the image overlay between NIR and color channels can be well maintained. This solution has two major advantages: the light weight of the entire imaging system and optical simplification. First, the optical part in the imaging system only contains optical lenses and spectral filters, which yields a compact and lightweight goggle device. Second,

optical simplification reduces the number of optical parts contributing to the optical display of the NFIS system, which leads to similar or even better optical performance. Additionally, compared with the CCD imaging sensor commonly used in existing NFIS, the CMOS imaging sensor leads to a much smaller form factor camera module, lower power consumption, and higher quantum efficiency in the NIR spectrum. The simplified peripheral circuitry further reduces the weight of the camera module. For our SIFT feature matching three camera system, it can compute accurate disparity information based on the feature points on the experimental object itself. Neither additional tracker nor complex optical setup is needed for performing image overlay, which brings a huge benefit on applying our system in practical intraoperative use. Furthermore, simplified optical setup optimizes the sensitivity and detectability of the imaging sensor system. The footprint and weight of the imaging system also gets minimized by simplifying the optical components. Another big improvement of the NFIS is the three camera setup enables stereoscopic view for the surgeons, which is the first time according to what we know so far, to offer them real depth information of the target. This huge advantage could let surgeons precede operation much more accurately, and increase the success rate of the intraoperative treatment in the operating room.

To examine the performance of the NFIS solutions, we measured detectability and sensitivity achieved as a function of fluorescence concentration under real-time frame rates and standard working distance. The results show that the NFISs running at 27 FPS can detect concentrations as low as 25 nM ICG-DMSO. Therefore, the NFISs can achieve similar or even better sensitivity compare to other existing NFISs reported in the literature, and their performance can be easily improved simply by applying better optical lenses. The *in vivo* study in mice also validates that the NFIS solutions are able to precisely highlight tumor margins while performing good image

overlay. The downside of our solution is the disparity error brought by different depths between the reference points created by LED tracking pod or features, and the targeting area. However, based on our error tolerance test, our NFISs can stay within a 2-mm offset when the depth difference is less than 6 cm at a 65-cm working distance. So for regular surface operation and typical animal study, the offset is within the tolerance scale.

Finally, in this work, we present our efforts to push the NFIS development from a hardware-emphasized design to the concept of a software-hardware co-design, which not only takes advantage of the computational power of modern computers but also simplifies the necessary optical setup. The experimental measurements show that although our threshold detection algorithm does not require much computational complexity on the programming side, it achieves good image overlay results, as well as a simplified optical setup. The downside of our proposed SIFT feature matching based camera system is the relatively slow image overlay information update rate, and heavy feature dependency. However, the advancement of computer hardware allows us to accelerate the SIFT algorithm easily. GPU[35][36] and multi-core implementation [37][38] of the SIFT algorithm will be implemented in the following technological progress. The actual sensor system design, such as PCB and lenses design, will also be further optimized to have a high precision camera setup for image capture[39]. Currently, our NFISs work well in preclinical animal study and characterization test, further clinical trial is necessary to validate their performance in the operating room. In addition, spectral or polarization features[40] of clinical object will be explored to further define the feature points that SIFT replies on, and achieve more accurate result.

2.7 Conclusion

In this Chapter, we present two compact NIR fluorescence imaging systems (NFIS) for NIR fluorescence imaging. The first NFIS is threshold detection based two camera NFIS, which can be easily integrated with a goggle display system for intraoperative guidance. The NFIS achieves NIR-visible image overlay with high precision and a real-time frame rate. In addition, the miniature and ultra-light weight LED tracking pod is easy to incorporate with a NIR fluorescence imaging study. Based on experimental evaluation in a mice *in vivo* study, the NFIS solution can achieve down to 25 nM ICG detectability at 27 FPS and realize highly precise image overlay of NIR and visible images. The overlay error is limited within a 2 mm scale at a 65 cm working distance, which is highly reliable for clinical study and surgical use. The second NFIS is SIFT feature matching based three camera NFIS. The NFIS enables stereoscopic view and tool free high precision image overlay solution for intraoperative guidance. In characterization test, the NFIS solution achieves less than 0.4mm disparity error, more than 25 dB SNR, and down to 25 nM detectability while running at 27 FPS frame rate. And it also demonstrated accurate image overlay NIR-visible results in *in vivo* animal study.

Chapter 3. Beam Splitter Based Single Camera System with Goggle Display for NIR Fluorescence Imaging

3.1 Background

Image guided surgery (IGS) utilizes emerging imaging technologies to provide additional structural and functional information to the physician in clinical settings. This additional visual information can help physicians delineate cancerous tissue during resection as well as avoid damage to near-by healthy tissue. Near-infrared (NIR) fluorescence imaging (700 nm to 900 nm wavelengths) is a promising imaging modality for IGS, namely for the following reasons: First, tissue absorption and scattering in the NIR window is very low. Second, spontaneous tissue fluorescence emission is minimal in the NIR region [8]. Third, decoupling the fluorescence signal from the visible spectrum allows for optimization of NIR fluorescence while attaining high quality color images. Fourth, there are two FDA approved fluorescent dyes in the NIR region—namely methylene blue (MB) and indocyanine green (ICG)—which can help to identify tumor tissue due to passive accumulation.

The aforementioned advantages have led to the development of NIR fluorescence imaging systems for a variety of clinical applications, such as sentinel lymph node imaging [14], angiography [17], and tumor margin assessment [41]. With these technological advances, secondary surgeries due to positive tumor margins or damage to healthy organs can be largely mitigated, reducing the emotional and financial toll on the patient.

In the previous chapter, two multi-channel NIR fluorescence imaging systems (NFISs) were presented with detailed performance evaluations. The threshold detection- based two camera

NFIS provides a compact, accurate NIR-visible co-registration in real time by using an external LED tracking pod [42]; the SIFT feature matching-based three camera NFIS uses a feature matching algorithm to extract features from the object area and achieve accurate NIR-visible image overlay. However, the location difference between the object and reference points created by external tools or features causes a disparity error in the NIR-visible co-registration. This disparity error leads to one major drawback: inaccurate positive margin information during the image guided surgery. The incapability of the human eye to sense the NIR spectrum makes surgeons heavily rely on NFIS to check positive margins, so incorrect margin information increases the risk of incomplete excision and has negative impacts on the imaging guidance benefit that NFIS provides during surgery. Therefore, the disparity error needs to be well modeled and studied in NFIS development.

Currently, in order to minimize the disparity error in the NIR-visible co-registration, most NFISs that are available commercially or undergoing clinical trial—such as FLARE [43], SPY [15], and Fluobeam [44]—use two separate CCD/CMOS cameras with a complex optical setup to minimize distortion and vignetting [45] to capture multi-spectral images. These images are then combined with real-time image processing to present an augmented view to the surgeon. The information is presented on a standard monitor above the operating bed, which requires the physician to stop the surgical procedure and look up at the monitor. The break in surgical flow sometimes outweighs the benefits of fluorescence based IGS, especially in time-critical surgical situations. Furthermore, these instruments tend to be very bulky and have a large foot print, which significantly complicates their adoption in an already crowded operating room.

In this chapter, we describe a compact and wearable goggle system capable of real-time sensing of both NIR fluorescence and color information. The system uses the similar orthogonally

aligned beam splitter based dual optical path setup, but replaces two separate cameras with two CMOS imaging sensors in one camera case. It also uses an FPGA for real-time signal processing and a goggle device for displaying a synthetic image (color image combined with NIR information) to the physician with minimum latency. The efficacy of the entire imaging system has been experimentally verified and optimized for high signal-to-background fluorescence imaging using an analytical approach. The complete imaging system is undergoing clinical trials for imaging sentinel lymph nodes in both breast cancer patients and melanoma patients. The human pilot study was approved by the Washington University St. Louis Medical School's internal review board (IRB).

3.2 Beam Splitter Based Single Camera System Setup

We have developed a real-time multi-spectral NIR fluorescence imaging system capable of simultaneously capturing NIR fluorescence emission and color images. The imaging system is comprised of the following: 1) an illumination light source, 2) an imaging module implemented using CMOS imagers and optimized optical setup, 3) an image processing module implemented on an FPGA, and 4) a goggle with a high definition screen for real-time display of visual information to the surgeon. The block diagram of the imaging system is shown in Fig. 3.1(a).

3.2.1 Illumination Light Source Design

The purpose of the illumination light source is twofold. First, it has to illuminate the tissue of interest such that both the surgeon and the imaging sensor register a high quality image in the visible spectrum. The current guidelines for surgical light source are a color rendering index between 85 and 100 and a minimum central luminance of 40k lux. The high illumination intensity used in the surgical settings allows for high signal-to-noise ratio imaging with a typical CMOS imaging sensor at 30 frames per second or higher.

The second purpose of the illumination source is to provide excitation for the NIR dye used to mark the cancerous tissue. A typical surgical light source has a significant NIR component beyond the excitation wavelength for the fluorescent dye. Hence, an NIR image due to reflection from the tissue dominates the signal and impedes the detection of the fluorescence signal. In order to mitigate this issue, custom built band pass filters are placed in front of the surgical light source to block the unwanted IR illumination. The color rendering is minimally altered with the additional filters with a transmission efficiency of 96% [46].

Custom built NIR LEDs are added next to the surgical light source and are used to excite the fluorescent ICG dye molecules. A band pass spectral filter (750 nm to 790 nm) is added to the NIR LEDs to remove higher NIR wavelengths beyond the necessary excitation light.

3.2.2 Color-NIR Imaging Module

Fluorescence and color information is captured via two CMOS imaging sensors (Aptina MT9V034): one monochromatic sensor for NIR signal sensing and one color sensor for visible signal sensing. Both sensors have 753 by 480 pixels (XVGA resolution), a quantum efficiency of 40% at 800 nm, and a pixel pitch of 6 μm2. The two imaging sensors operate in a master-slave configuration, i.e. 8 bits of data is sent from the monochromatic/NIR imaging sensor to the color imaging sensor via a two-line low-voltage differential signaling (LVDS) serial bus. The color imaging sensor combines 8 bits of data from both sensors and produces a single 16-bit word that contains information from both sensors (the lower 8 bits of data correspond to the color imager and the upper 8 bits of data correspond to the monochromatic/NIR imager). The 16 bits of data are serialized and sent via a two-line LVDS bus to the image processing module, hence minimizing the number of wires utilized to transfer data from both sensors.

Custom PCB boards (1.5 cm by 1.5 cm) house both CMOS imagers, which are integrated with spectral filters in a compact housing, as shown in Fig. 3.2 (a). A dichroic beam splitter is used such that visible spectrum information (400 nm–700 nm) is passed in one direction and NIR information (>800 nm) is passed in the orthogonal direction. The color sensor senses visible spectrum information and the monochromatic sensor senses NIR information. The beam splitter ensures that the images between the two sensors are always co-registered. In addition, spectral filters are placed in front of the imaging sensors: a short-pass filter with a cutoff wavelength of 694 nm (Semrock FF01-694) is integrated with the color imager, while a long-pass filter with a cutoff wavelength of 785 nm (Semrock BLP01-785R) is integrated with the monochromatic imager (Fig. 3.1(b)). A compact 3D-printed camera case (Fig. 3.1(c)) is designed for imaging sensor and optical setup housing.

The camera box is mounted on the side of a goggle (Fig. 3.1(d)), allowing for easy and ergonomic wear of the system in the operating room by a surgeon (Fig. 3.1(e)). The FPGA board receives information from the two imagers via an LVDS bus, where signal processing algorithms are implemented with minimum latency (165 μsec) to ensure real-time display of information to the surgeon.

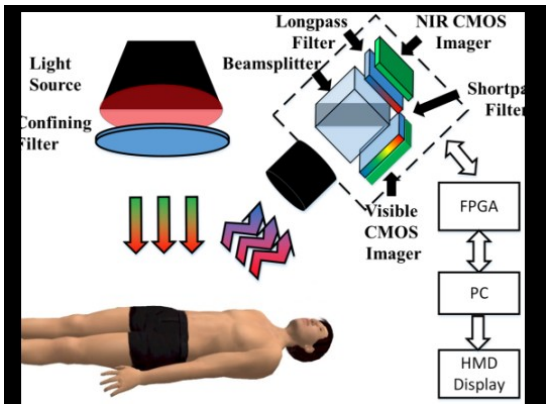

(a)

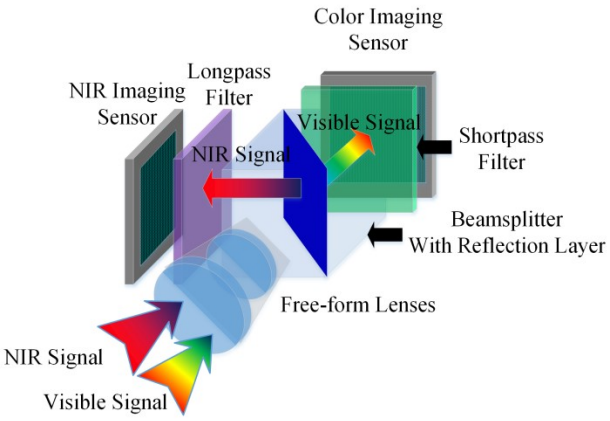

(b)

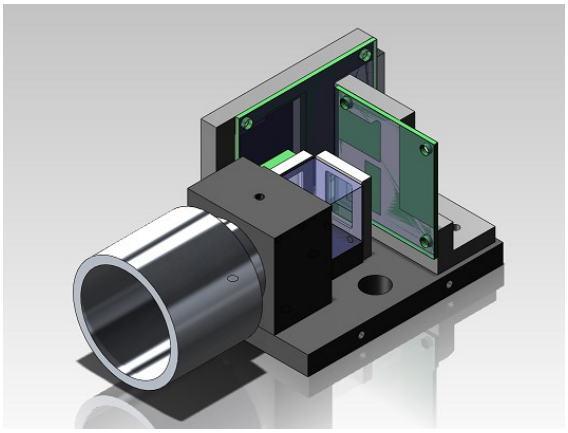

(c)

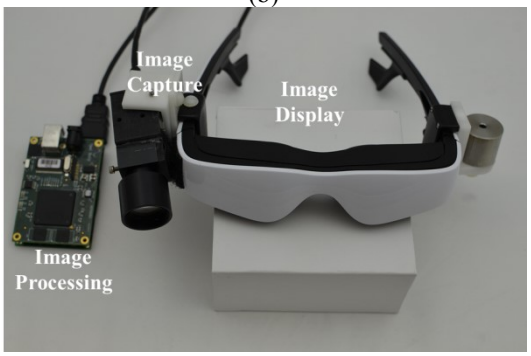

(d)

(e)

Figure 3.1. (a) Block view of fluorescence imaging system, (b) architecture of the beam splitter based single camera, (c) 3D-printed camera case, (d) the NFIS prototype, and (e) system under test in the operating room.

3.2.3 FPGA-Based Image Processing Module

The image processing module is composed of a custom PCB board, an FPGA, and an optional PC. The custom PCB board is designed to 1) connect with the two imaging sensors, 2) mate with an FPGA board, and 3) connect to the goggle display via an HDMI chip housed on the same custom PCB board. The connection between the imaging sensor board (Fig. 3.2(a)) and the

image processing board are accomplished via a custom mini-HDMI connector. This connector allows for nineteen independent signals to be transferred between two entities, including 4 LVDS line pairs. In our camera system, two lines are used for LVDS imaging data transmission, two lines are used for sending and receiving control signals, two lines are used for external exposure control, and the rest of the lines are used for power supply and signal shielding. The LVDS data from both imaging sensors is deserialized in the FPGA (Opal Kelly 3050, Xilinx Spartan 3). The FPGA board can either transfer the deserialized data to a PC via a USB 2.0 data link for image processing or execute the necessary image processing to provide a single combined NIR-visible spectrum image on the FPGA.

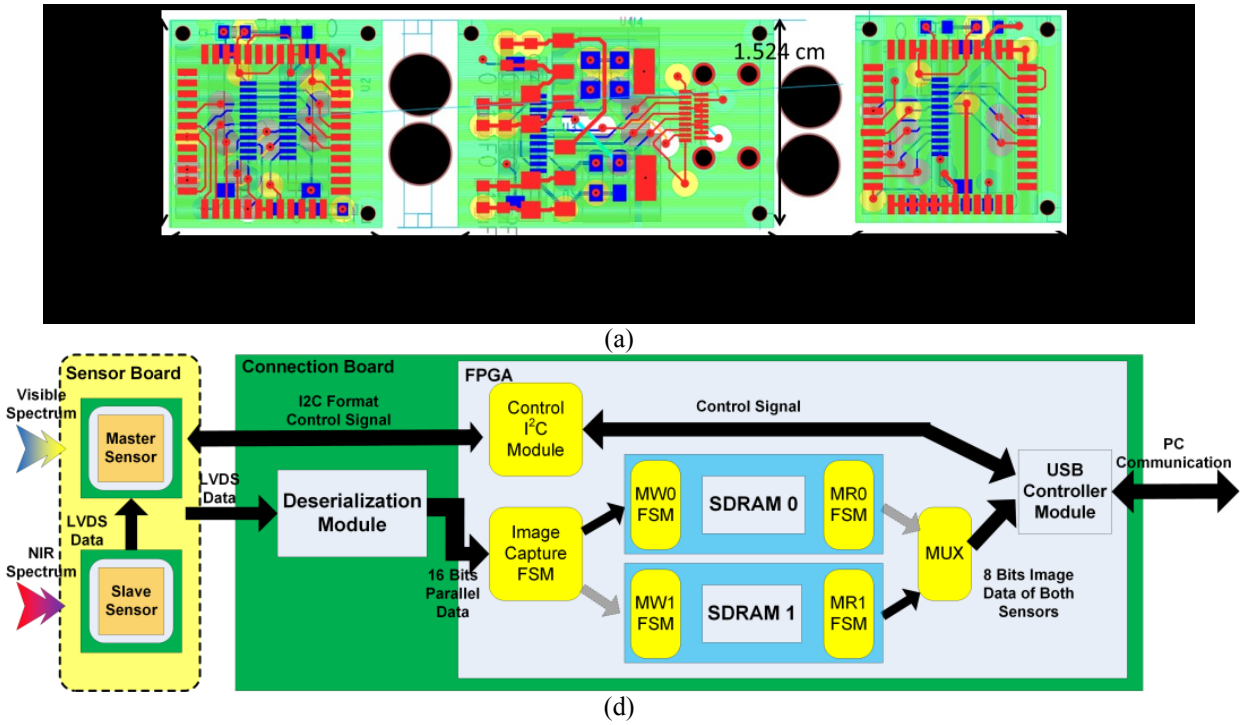

Figure 3.2. (a) PCB board layout for imaging sensor housing and (b) block view of the FPGA-based image processing module.

The image processing routine on the FPGA performs the following steps: 1) realign the color and NIR images, 2) threshold the NIR image, and 3) combine color and NIR images into a single image in which NIR information is highlighted using false color. Two SDRAM chips are used to

realize simultaneous data acquisition from the imaging sensor and either image processing or data transmission to the PC. As shown in Fig. 3.2(b), one SDRAM chip stores the pixel data from a memory control write state machine, while the other SDRAM chip either processes the data or transfers it to the PC. Since the FPGA is a compact device and can be easily carried in a pocket, the surgeon is free to move around the operating room, and the entire device does not impede the surgical flow.

3.2.4 Optical Filter Design Specifications

The optical filter design and excitation light wavelength is critical for high quality fluorescence imaging. Several factors influence the quality of fluorescence imaging, including quantum efficiency (QE) of the sensor and the quantum yield (QY) of the dye, tissue and dye absorption, and tissue reflection properties. Some of these factors, such as QE and QY, have opposite constraints. For example, typical CMOS imaging sensors have high quantum efficiency for shorter NIR wavelengths, such as 700 nm, and lower quantum efficiency for longer NIR wavelengths (Fig. 3.3). The quantum yield for typical NIR dyes, such as ICG or LS301, is maximum around 780 nm to 820 nm, a region in which the quantum efficiency of the CMOS imager is low. Hence, placing the excitation light source at shorter NIR wavelengths will benefit from high QE of the CMOS sensor, with the shortcomings of the lower QY of the dye. The opposite is true for an excitation light source at longer NIR wavelengths (Fig. 3.3).

Next, we derive a close form solution for fluorescence contrast in order to determine an optimal wavelength for the excitation light source. The output photon flux from the NIR excitation light source, $S_{excitation\_light}$, is described by equation (3.1), where TBP is the transmittance of the band pass filter and $S_{lightsource}$ is the NIR LEDs photon flux.

$$S_{excitation\_light}(\lambda) = T_{BP}(\lambda) \bullet S_{lightsource}(\lambda) \quad (3.1)$$

The fluorescence dye will absorb a portion of the excitation light photons and will emit fluorescent photons at higher wavelengths. Therefore, the efficiency of the transformation is mainly decided by the dye's absorbance, A(λ), and quantum yield, QY(λ). The photon flux of the fluorescence signal, $S_{emission\_signal}$, is a product of the absorbance, quantum yield, and optical power of the excitation light, as illustrated by equation (3.2).

$$S_{emission\_signal}(\lambda) = A(\lambda) \bullet QY(\lambda) \bullet S_{excitation\_light}(\lambda) \quad (3.2)$$

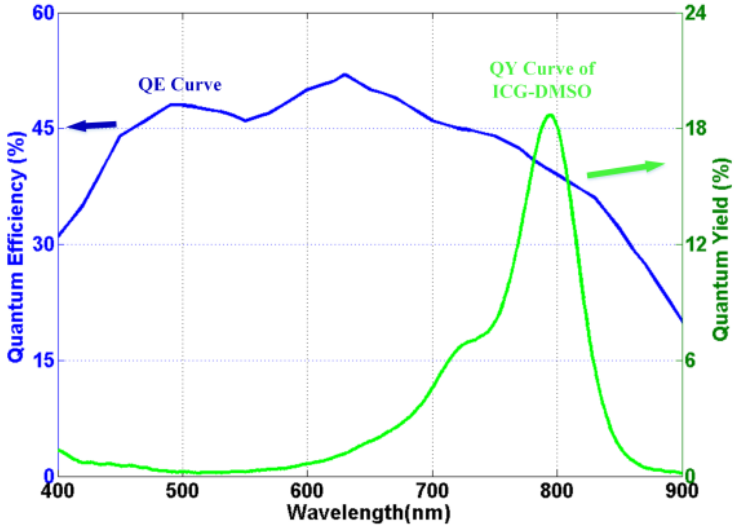

Figure 3.3. The quantum efficiency of the CMOS sensor and the quantum yield of the fluorescence dye should be closely considered to determine the optimal excitation wavelength.

The emitted fluorescence photons will impinge on a CMOS photodiode and generate electron-hole pairs depending on the quantum efficiency of the imaging sensor, QE(λ). The imaging sensor should only register photons in the emission spectrum and should block photons from all other wavelengths. Hence, a long pass filter, with transmission $T_{long\_pass}(\lambda)$, is used to collect fluorescent photons with the CMOS image sensor. The total number of photo-generated electron-hole pairs per area and per time in the CMOS imaging sensor, $G_{fluorescence}(\lambda)$, due to fluorescence is presented by equation (3.3).

$$G_{fluorescence}(\lambda) = T_{long\_pass}(\lambda) \bullet QE(\lambda) \bullet S_{emission\_signal}(\lambda) \qquad (3.3)$$

A portion of the excitation light source will be reflected from the tissue and will travel toward the imaging sensor. A portion of the reflected excitation light will be blocked using optical filters placed in front of the sensor. The reflected photon flux impinging on the CMOS sensor is described by equation (3.4).

$$G_{reflected\_light}(\lambda) = T_{BP}(\lambda) \bullet R(\lambda) \bullet T_{optical}(\lambda) \bullet F_{emission\_light}(\lambda) \qquad (3.4)$$

Two parameters are important for fluorescence imaging: contrast ratio and photocurrent of the fluorescence signal. Fluorescence contrast is the ratio of the electron-hole pairs generated due to the fluorescence signal and the electron-hole pair generated due to the reflected light, which is defined by equation (3.5).

$$Fluorescence\ Contrast = \frac{\int_{\lambda \in emission} G_{fluorescence}(\lambda)}{\int_{\lambda \in excitation} G_{reflected\_light}(\lambda)} \qquad (3.5)$$

In order to determine an optimal excitation wavelength, we used a fluorometer (HORIBA Fluorolog-3) to determine the emission spectra of the fluorescent signal for three different excitation wavelengths. Figure 3.4 presents the emission spectrum for 720 nm, 760 nm, and 780 nm excitation. The emission spectrums are collected at 735 nm, 775 nm, and 795 nm. These excitation wavelengths were chosen because the quantum efficiency of the CMOS imager is highest at 720 nm and lowest at 780 nm, whereas the dye's absorption is lowest at 720 nm and highest at 780 nm. The peak spectral wavelength of emission is at 820 nm. Table 3.1 summarizes our analytical and experimental results. Hence, an excitation wavelength at 780 nm generates the highest photocurrent and has the highest contrast ratio.

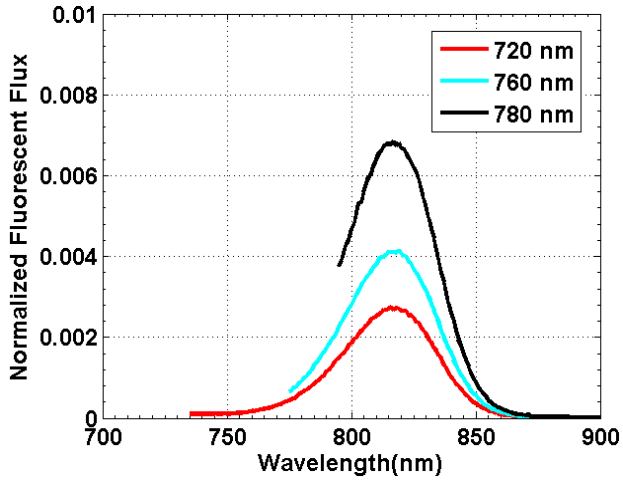

Figure 3.4. Emission spectrum of ICG-DMSO for three different excitation wavelengths. The peak emission is at 820 nm.

Table 3.1. LED responses comparison

Excitation Wavelength	720nm	760nm	780nm
Normalized Photocurrent	4.95%	7.03%	9.91%
Fluorescence Contrast	0.79	1.12	1.57

3.3 Performance evaluation

3.3.1 Detectability

The detectability of the beam splitter based single camera NFIS was tested by using difference concentrations of ICG and LS301 dissolved in 100% dimethyl sulfoxide (DMSO) [47][48]. The vials with different ICG and LS301 concentrations are placed 50 cm from the imaging sensors. A control vial with DMSO is also imaged and denoted as a background signal. The NFIS was tested with its visible and NIR imaging sensors operating at 27 FPS (i.e., a maximum exposure time of 30 ms). The exposure time for the color imaging sensor is typically around 1 ms due to the bright surgical LED light source. The NIR image sensor has a maximum exposure time of 30 ms to acquire the best signal-to-background ratio (SBR) fluorescence signal. The diluted samples are illuminated with a 780 nm excitation light source, and two different optical powers (5mW/cm2 and 10mW/cm2) are used for the test evaluation. The mean and standard deviation of

the signal-to-background ratio (SBR) of the imaging system is calculated from a 30-by-30 pixel region.

The detectability results from the NFIS are presented in Fig. 3.5. Figure 3.5(a) shows the signal intensity for different ICG and LS301 concentrations ranging from 300 pM to 50 uM. Higher illumination power increases the signal response from the same fluorescence sample. When the ICG and LS301 concentrations are higher than a certain threshold (1 uM for ICG and 1 uM for LS301 under 10 mW/cm^2 illumination; 5 uM for ICG and 10 uM for LS301 under 5 mW/cm^2 illumination), the fluorescent signal intensity exceeds the dynamic range of the imaging sensor. Hence, the imager output is saturated. Figure 3.5(b) shows the SBR for the imaging system, where the vial with 100% DMSO is used as the background control negative sample. Defining the detectability of a system to be SBR = 2 [13], the imaging system can detect 30 nM of ICG and 30 nM of LS301 under 10 mW/cm^2. Using an excitation illumination of 5 mW/cm^2, the minimum ICG detectability is 50 nM and 50 nM for LS301. On the other hand, as seen in Fig. 3.5(b), the higher excitation power leads to lower SBR at higher concentrations, which occurs because the fluorescent signal is saturated while the background signal is higher. Therefore, selecting a proper optical power for the illumination module is always a tradeoff between keeping a high SBR and a high signal response.

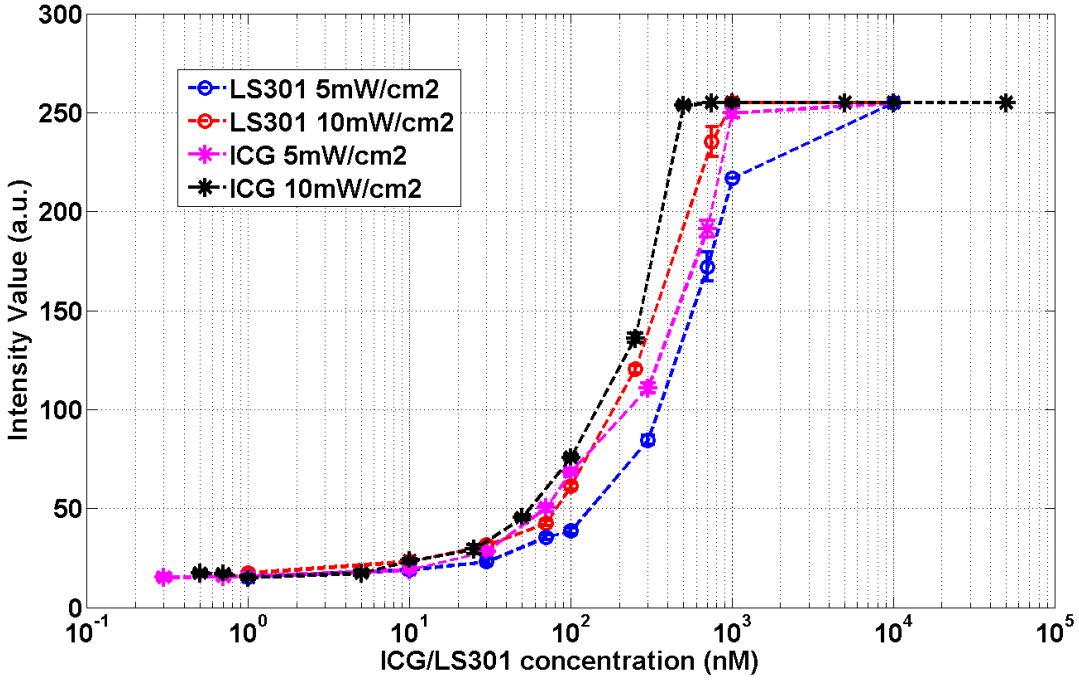

(a)

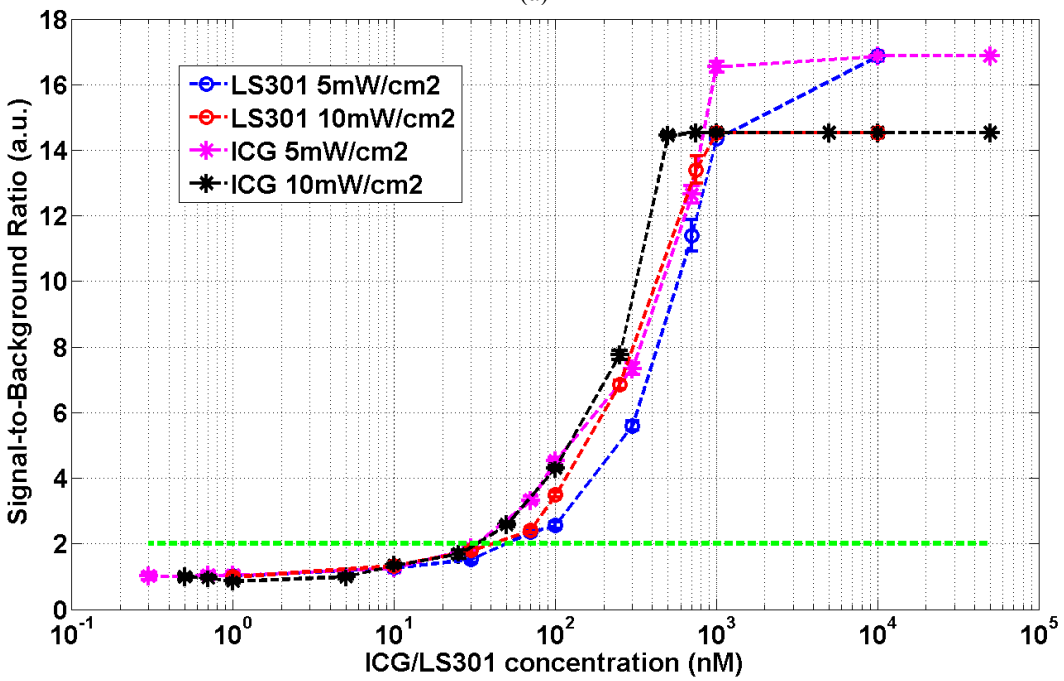

(b)

Figure 3.5. Detectability test using ICG-DMSO and LS301-DMSO, (a) fluorescence signal response, and (b) signal-to-background ratio (SBR); green line shows the SBR = 2 threshold.

3.3.2 Sensitivity

The sensitivity of the NFIS solution was measured by using a signal-to-noise ratio (SNR). As explained in the previous chapter, SNR is the ratio of the signal response to the variation of the

signal responses. Higher SNR represents better system sensitivity in distinguishing signal change. Because auto-fluorescence and background reflection commonly exist in tissues and bio-materials, it is important to eliminate their influence on signal response.

In our experiment, the sensitivity of the NFIS solution was measured by computing the SNR of the NIR fluorescent signal responses of different ICG concentrations in DMSO. The NFIS solution was setup at 50 cm working distance, and 27 FPS (30 ms exposure time). ICG-DMSO concentration samples were illuminated under two different illumination powers (5 mW/cm^2 and 10 mW/cm^2). For each concentration, 128 frames of images were collected to compute the signal intensities and their deviation (considered as noise).

Figure 3.6 shows the sensitivity results of the NFIS solution. Higher illumination power leads to slightly higher SNR. The SNR difference under different illumination powers becomes smaller on ICG samples with higher concentration because the imaging sensor is approaching saturation, and fewer photons can be collected by the photodiode. The SNR measurement shows that the SNR of the NFIS solution can achieve more than 15 dB when ICG concentration is above 10 nM and while the system is running at 27 FPS. The 15dB SNR result is much higher than the confidence level of a normal signal distribution, which is defined to be 6dB for 95%, and 9.5dB for 99.7% (shown as the green dotted line in Fig. 3.6) [50].

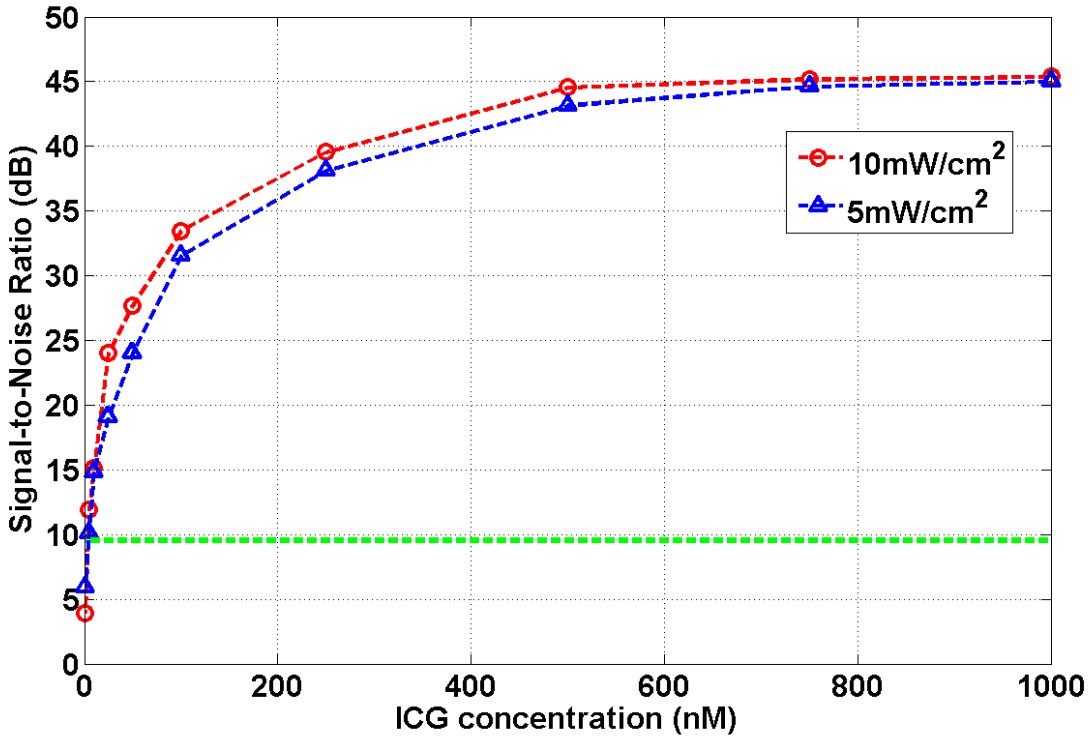

Figure 3.6. Sensitivity test with SNR measurement using ICG.

3.4 Experimental Results

3.4.1 *In Vivo* Mouse Study

The NIFS was also evaluated through *in vivo* studies using a subcutaneous breast cancer mouse model. The model was developed by administering a subcutaneous flank injection to four-to-six-week-old BalbC mice with 100,000 4T1Luc murine breast cancer cells. The mouse was imaged 10–12 days after injection. During *in vivo* study, the NFIS was set up at a 50 cm working distance, and the illumination module was placed at a 50 cm distance. All images were captured at 27 FPS. During the imaging experiments, the mouse was kept anesthetized using a cocktail of ketamine/xylazine or through intubation of isofluorane. Following the imaging experiment, the mouse was sacrificed through cervical dislocation, and its organs were harvested, imaged, and preserved for histologic evaluation.

Figure 3.7 shows the test results of the mouse object, Fig. 3.7(a) is the NIR signal mapped in false JET color with proper threshold, Fig. 3.7(b) is the visible image of the mouse body, and Fig. 3.7(c) shows the image overlay result by combining both the NIR and visible channels. The tumor is clearly detected, and its margins in NIR and visible channels match accurately. The histology study results shown in Fig. 3.7(d) validate the imaging results captured by our NFIS.

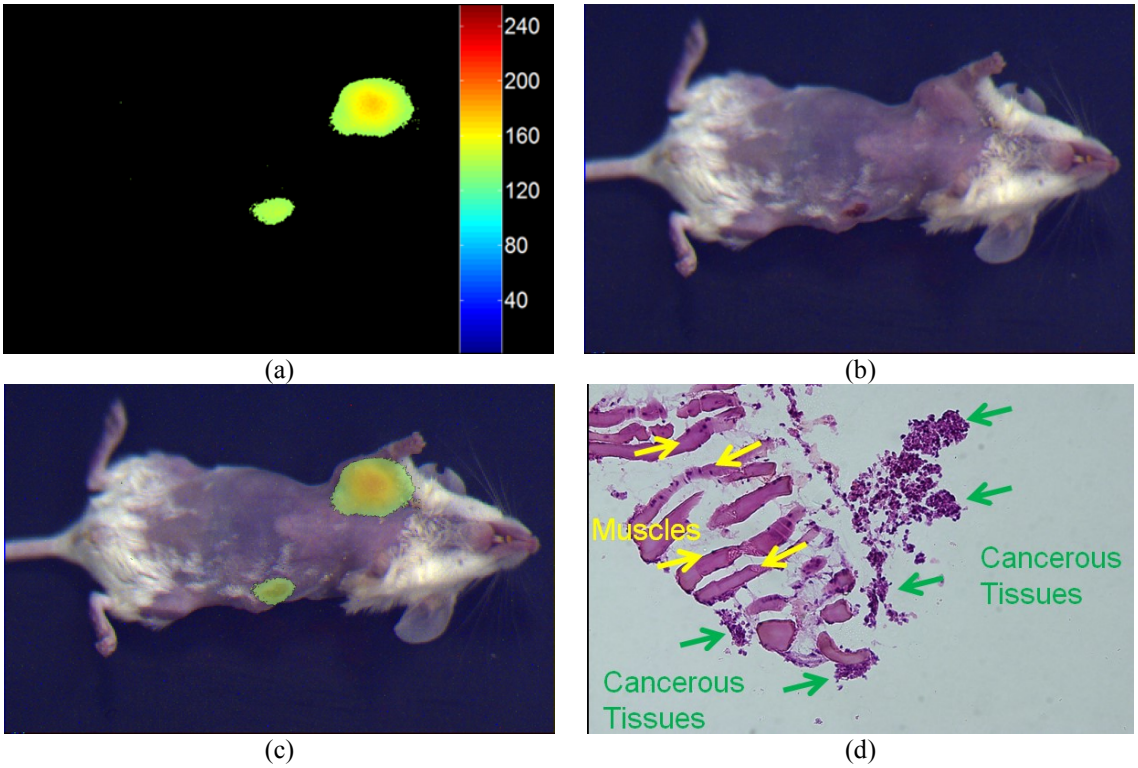

Figure 3.8. Mouse model study at 30 ms exposure time, (a) NIR channel, (b) NIR-visible overlay channel, and (c) histology test verification.

3.4.2 Human Pilot Study

A human pilot study was conducted to examine the practical performance of the beam splitter based NFIS. Currently the NFIS has been tested on breast cancer patients (N=10) undergoing lumpectomy, partial mastectomy, or radical mastectomy and on melanoma patients (N=5) undergoing wide excision of skin lesions for sentinel lymph node mapping. Before the surgery, as a commonly used visual tracer, ICG was injected into the patient's tumor area with a lower

concentration (5mg/ml; 5ml) for NIR fluorescence imaging, and the region was under site massage for 5 minutes. At 10–15 minutes post injection, surgeons used the NFIS to observe the sentinel lymph node area. The NFIS was set up at a 50 cm working distance, and the illumination module was placed at a 1 meter distance. All images were captured at 27 FPS. The in vivo human pilot study results of the sentinel lymph node mapping of the NFIS are shown in Fig. 3.9. Figure 3.9(a) is the NIR signal with the proper threshold (threshold value equals 40), Fig. 3.9(b) is the visible channel image, and Fig. 3.9(c) shows the image overlay result by combining both NIR and the visible channel. The sentinel lymph node is clearly detected, and its margins in NIR and the visible channels match accurately after proper disparity adjustment being implemented before observation. This disparity adjustment means applying constant disparity offset values to the horizontal and vertical direction of imaging results to compensate for the disparity between the field of view of the two imaging sensors, which are generated during mechanical alignment of the imaging sensors and corresponding optical components.

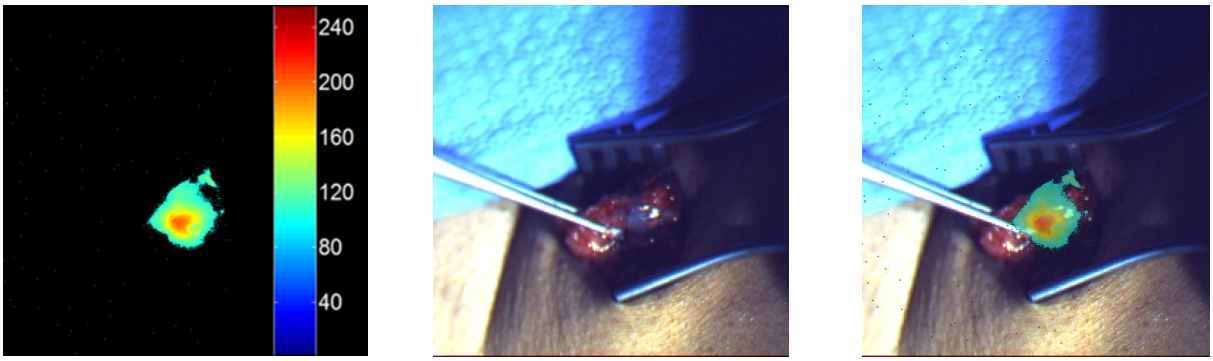

(a) (b) (c)

Figure 3.9. In vivo human pilot study on sentinel lymph node, (a) NIR, (b) visible, and (c) NIR-visible co-registered results.

Using the same NFIS setup, the ex vivo human pilot study results of the sentinel lymph node mapping of the NFIS are shown in Fig. 3.10. Figure 3.10(a) is the NIR signal with the proper threshold (threshold value equals 40), Fig. 3.10(b) is the visible channel image, and Fig. 3.10(c)

shows the image overlay result by combining both NIR and the visible channels. The margins of the sentinel lymph node in NIR and visible channels match accurately after the proper disparity adjustment is implemented before image display. Using histologic analysis as the gold standard, our NFIS with ICG injection for sentinel lymph node mapping maintains a 100% matching rate.

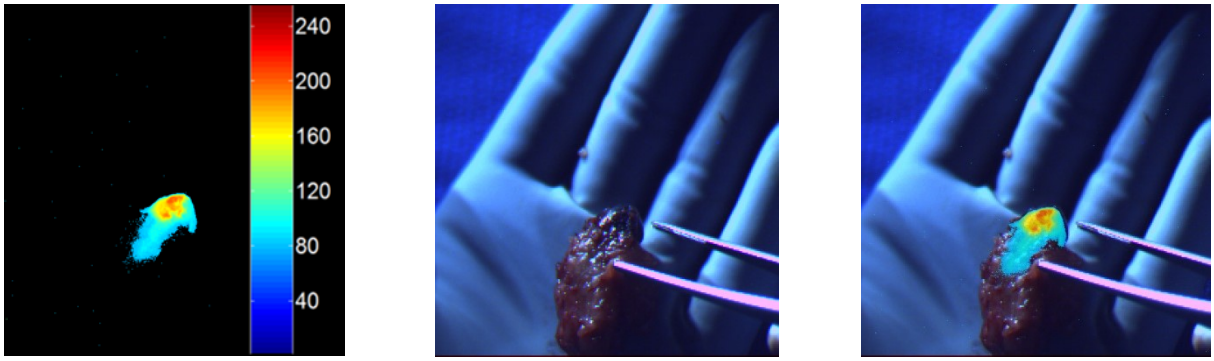

(a) (b) (c)

Figure 3.10. *Ex vivo* human pilot study on sentinel lymph node, (a) NIR, (b) visible, and (c) NIR-visible co-registered results.

3.5 Conclusion

In this Chapter, a compact beam splitter based single camera NFIS for intraoperative guided surgery is presented. The system offers 27 FPS real-time frame rate, NIR-visible dual-channel image streaming. The design of its electronic and optical parts are analyzed. The performance of the NFIS is evaluated under both detectability and sensitivity measurements. The NFIS is then further rested in an in vivo mouse model study for breast cancer and a human pilot study of sentinel lymph node mapping. The results show that the system could offer sensitive and accurate NIR fluorescence imaging results for possible use in intraoperative guidance.

Chapter 4. Bio-inspired Multi-Spectral Imaging Sensor and System Development

4.1 Introduction

In oncologic surgery, differentiating tumor tissue from surrounding healthy tissue is a major challenge. Physicians still rely on their eyesight to determine the location of the tumors, which leads to a high secondary surgery rate [2][7]. Image guided surgery (IGS) aims to provide additional structural- and functional-related visual information to assist physicians in clinical settings. This additional visual information can help physicians precisely identify cancerous tissue during resection as well as preserve near-by healthy tissue. Near-infrared (NIR) (700 nm to 900 nm) fluorescence imaging is a promising multi-spectral imaging modality for IGS for the following reasons. First, the low tissue absorption and scattering in the NIR spectrum allow for deeper imaging and localization of tumor tissue up to a 1 cm range depending on the surrounding tissues. Second, human tissue has minimal spontaneous fluorescence emission in the NIR spectrum [3][51], which enables high signal-to-background ratio fluorescence imaging. Third, since the NIR fluorescence signal is decoupled from the visible spectrum, this enables the optimization of the NIR fluorescence signal while attaining a high quality visible spectrum signal. Fourth, the NIR signal can be effectively captured by using regular CCD or CMOS imaging sensors; thus, advances of current CCD or CMOS technology facilitate the system development of NIR fluorescence imaging. Additionally, two FDA approved fluorescent dyes in NIR spectrum, namely methylene blue (MB) and indocyanine green (ICG), have been widely used in oncologic surgery, which help distinguish malignant tissue due to passive accumulation [52]. On the other hand, the blindness of human eyes with respect to the NIR signal necessitates

the development of multi-spectral imaging technology. Therefore, a multi-spectral imaging system with accurate and sensitive NIR-visible signal detectability will contribute a critical weapon to the war on cancer.

Mechanisms of multi-spectral imaging in existing NIR fluorescence imaging technologies include division-of-time, division-of-amplitude, and post-processing-based multiple camera solutions. Division-of-time uses a single high-performance CCD/CMOS camera with high sensitivity in the visible and NIR spectra and a pulsed illumination light source to provide NIR and visible illumination alternatively. Adjacent time lapse images capture multi-spectral information, and multi-channel co-registration is executed in the post-processing stage by overlaying time lapse images [53]. The division-of-time solution can achieve precise multi-spectral channel co-registration with a simple imaging setup. However, pulsed illumination often leads to insufficient photon collection for real-time imaging requirements. The division of amplitude uses a beam slitter based optical setup to split the incoming spectral signal of an identical field of view into different spectral channels and overlay this information on multiple sensors. Commercial NIR fluorescence imaging systems (NFISs), such as FLARE [54], SPY [15] and Fluo-beam [44][55], mainly use this technology, since it offers the most robust and simplest solution for NIR fluorescence imaging. However, this solution suffers from a large footprint and a potential long lead time on calibration before practical use. Additionally, the complex optical setup causes signal loss during transmission, which leads to a weaker multi-spectral signal. Post-processing-based multiple camera solutions [23][24] were proposed recently to achieve compact NFIS design while maintaining signal strengths. The implementation of post-processing algorithms in software benefits from a simplified hardware setup, but up until now, most solutions in this category were not practical due to the randomness of reference generation,

which affects the accuracy of multi-spectral information co-registration. Therefore, the major limitation of existing multi-spectral solutions is the tradeoff between the accuracy of multi-spectral information co-registration and the complexity of the instrumentation setup. Having a compact, real-time NFIS with accurate NIR-visible co-registration can meet the need of NIR fluorescence imaging used in image-guided surgery. The limited commonality between current engineering solutions of multi-spectral imaging and known biological solutions suggests that the development of new principles for imaging inspired by biological concepts from the nature can be a powerful force in solving emerging healthcare and instrumental problems. [56][57]

In this chapter, we show that a compact and innovative solution can be achieved if we can mimic the 10,000,000-year-old design features of the ommatidia of the monarch butterfly using state-of-the-art nanofabrication technology and advanced CCD/CMOS imaging sensor technology [58]. In our proposed design, pixelated spectral interference filters are integrated with a light sensitive CCD imaging sensing unit. The pixelated spectral filters are fabricated via a carefully optimized nanofabrication procedure and integrated with a CCD imaging array using off-chip alignment technology. The entire imaging system has been experimentally verified and optimized for high signal-to-background fluorescence imaging using an analytical approach. This bio-inspired spectral imaging sensor is integrated with a wearable goggle for easy integration in the operating room. The complete imaging system has undergone animal study for performance validation. A clinical trial is also being held at Washington University in St. Louis (WUSTL) Medical School for imaging sentinel lymph nodes in both breast cancer patients and melanoma patients, which was approved by WUSTL Medical School internal review board (IRB).

4.2 Interference Filter Concepts and System Setup

In nature, animals, especially insects, have sophisticated vision system. Inspired by the structures of their vision system, biomimetic approaches have greatly accelerated modern imaging system design. The monarch butterfly has an interesting ommatidium structure, which could be a cue to design a compact DoFP multi-spectral imaging sensor. The ommatidium structure of a monarch butterfly is shown in Fig. 1(a) [14], each ommatidium has a cornea to focus incoming light into pigment cell through crystalline tract; a rhabdom exists below the crystalline tract to sense the incoming light. In the rhabdom, a reflection layer with stacked layer structure reflects light at particular spectrum, while transmitting light at other spectrum to optical nerve underneath. The vertically stacking layers form an interference filter structure because it has multiple layers of cytoplasmic plate isolated by air gaps, and the refractive indexes of cytoplasmic plate and air gap are different. In Fig. 1(b) [14], the eye-shine effect is shown among different ommatidia in the scene, which is caused by different reflective wavelengths of tapetal filters in the butterfly's ommatidia [5]. The SEM image of the corresponding nano-fabrication implementation is shown in Fig. 1(c).

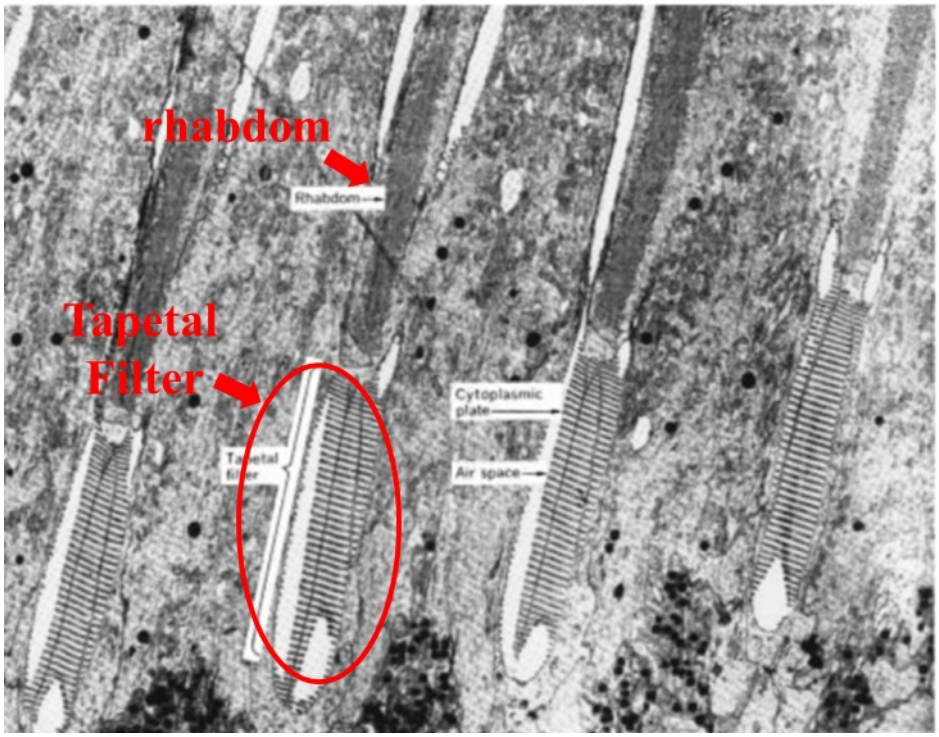

(a)

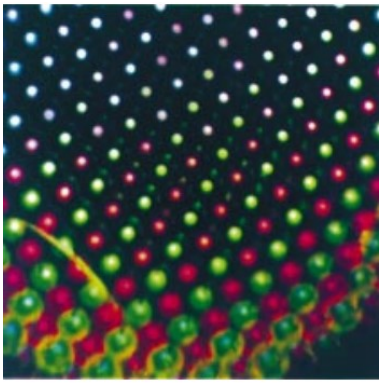

(b)

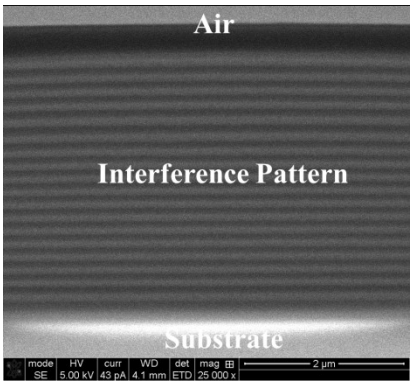

(c)

Figure 4.1. Interference filter structures, (a) ommatidium of monarch butterfly, (b) eye-shine effect of butterfly's ommatidium, (c) analogous structure of interference filter.

4.2.1 Principles of Interference Filter

The principle of the interference filter can be explained using interference theory of light, as illustrated in Fig. 4.2(a). When incident light passes through the interface of two materials (using

SiO_2 and TiO_2 as an example) with different refractive indexes, reflections from the two surfaces and thickness of middle material layer add phase differences into the reflective elements R_1, R_2, R_3, etc. As shown in equation (4.1) [60], if the traveling distance in the middle material layer of the incident light is integer times the wavelength of light, there would be no phase change among the reflective elements. The reflected light would be at its maximum reflection. On the other hand, if the traveling distance of the incident light in the center material layer shows odd integer times of the lights' half wavelength, the phase retardation will be π degrees. Hence, the reflective elements will cancel each other out, and the reflected light will be at its minimum amount, while most light of that wavelength will transmit through the middle material layer.

$$\begin{cases} 2nd\cos\beta = m\lambda \quad \text{..... maximum reflection} \\ 2nd\cos\beta = (m+\frac{1}{2})\lambda \text{..... maximum transmittion} \end{cases} \tag{4.1}$$

Considering the above interference effect through the whole visible spectrum, the thin-film interference structure has different responses to different wavelength of light. Equation (4.2) shows the relationship among the maximum reflective wavelengths and the depth of the layer, incident angle, and refractive index.

$$\lambda_{\max} = \left(\frac{4n_2 d}{2\left(\frac{n_2}{n_1}\right)+1}\right)\left(1-\frac{n_1^2}{n_2^2}\sin^2\beta\right) \tag{4.2}$$

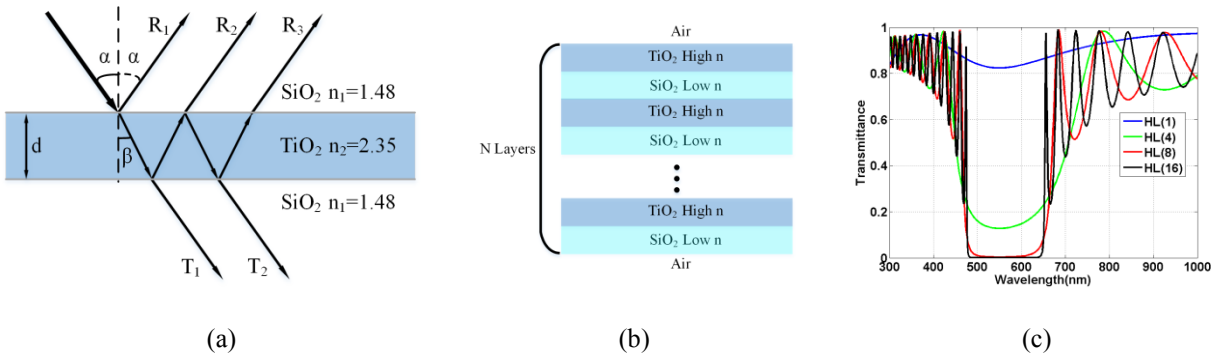

(a) (b) (c)

Figure 4.2. Interference concept and filter, (a) interference of light, (b) vertical structure of interference filter, and (c) an example spectral response of interference filter.

A single stacked structure of a high refractive index material layer and a low refractive index material is not enough to act as a filter. An optical interference filter is composed of multiple layers of interleaved high refractive index material and low refractive index material, shown as Fig. 4.2(b). The total transmission response will be a product of the reflective result of each layer. As shown in Fig. 4.2(c), HL represents the single stacked structure of a high refractive index material layer and a low refractive index material. More alternating layers between a high and low refractive index will lead to a higher ratio between the transmission band and the reflection band.

4.2.2 Pixelated Interference Filter

The proposed pixelated interference filter has a pattern containing four different pixelated spectral interference filters. As shown in Fig. 4.3, in a neighborhood of 2 x 2 pixels, four different spectral filters, R, G, B, and NIR are deposited on individual photo receptors. The neighborhood of four pixels is typically referred to as a "super pixel." It contains the information of all four spectral channels. Fig. 4.3(b) shows the micrograph of the proposed filter array, and Fig. 4.3(c) presents the lateral structure of single pixelated filter image captured using scanning electron microscope (SEM) imaging. Two different types of pixel interference filter were

designed for the proposed multi-spectral imaging sensor; one is a longpass filter type for NIR spectral imaging, and the other is a shortpass filter type for visible spectral imaging. The interference filters were fabricated using high-precision photolithography and physical vapor deposition (PVD). For visible pixels, an additional polymer spectral filter was spin-coated on top of the interference filter (shown in Fig. 4.3[c]) to further split visible spectrum light signal into R, G, and B channels.

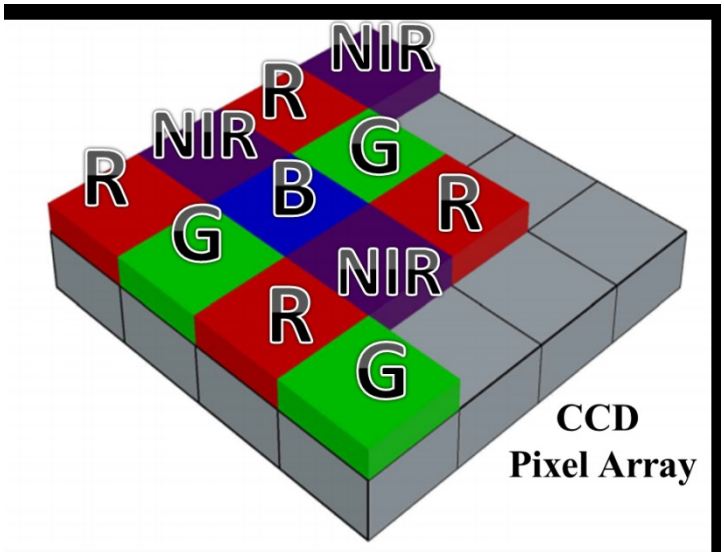

(a)

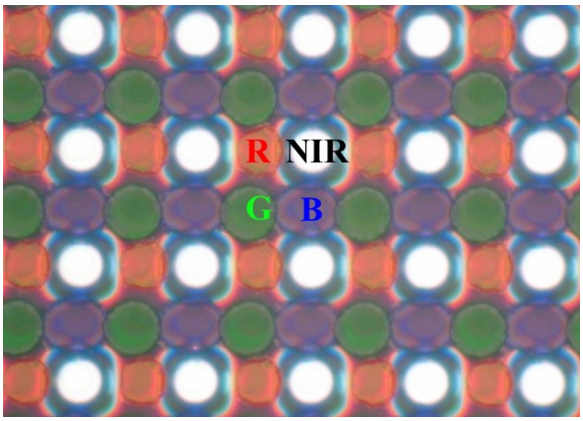

(b)

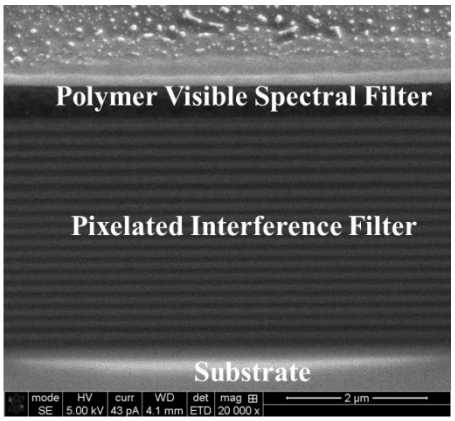

(c)

Figure 4.3. Proposed pixelated interference filter array, (a) block diagram, (b) micrograph of the proposed filter array, and (c) SEM image of the interference filter structure.

4.2.3 Bio-Inspired Multi-Spectral Imaging Sensor

The proposed bio-inspired multi-spectral imaging sensor is composed of a pixelated interference filter and a high performance CCD imaging sensor. Fig. 4.4(a) shows the filter topology and pixel structure of the proposed imaging sensor. The interference filter is fabricated with integer number of the pixel pitch in imaging sensor and aligned with CCD imaging sensor by strictly overlapping the photodetector with the interference filter. The blocking diagram of the alignment setup is shown in Fig. 4.4(b). Different high-power narrow-band spectral LEDs and collimating lenses were used to provide uniform light illumination at a specific wavelength. The proposed pixelated interference filter was flip-bounded to the CCD imaging sensor using a custom built nanometer-level precision six-freedom control station. By precisely tuning relative positions of the interference filter array and the CCD imaging sensor, signal responses from different pixels are expected to be maximized at their corresponding wavelength and minimized at other wavelength.

Small test samples of the proposed pixelated interference filter were fabricated and tested using the cleanroom facility at WUSTL. The final spectral imaging array contains a resolution of 720 x 534 pixels with a 14.8 micron pixel pitch. A high performance CCD imaging sensor (Kodak KA2020) [61] is used as the imaging sensor part. Using the off-chip alignment setup, precise filter-imaging sensor alignment was achieved. The lateral view of the proposed bio-inspired multi-spectral imaging sensor is shown in Fig. 4.4(c).

4.2.4 Illumination Light Source Setup for NIR Fluorescence Imaging

The purpose of the illumination light source serves for two major goals. First, it has to illuminate the tissue of interest such that both the surgeon and the imaging sensor register a high quality image in the visible spectrum. The current guidelines for surgical light source are color rendering index between 85 and 100 and minimum central luminance of 40k lux. The high illumination intensity used in the surgical settings allow for high signal to noise ratio imaging with a typical CMOS/CCD imaging sensor at 30 frames per second or higher.

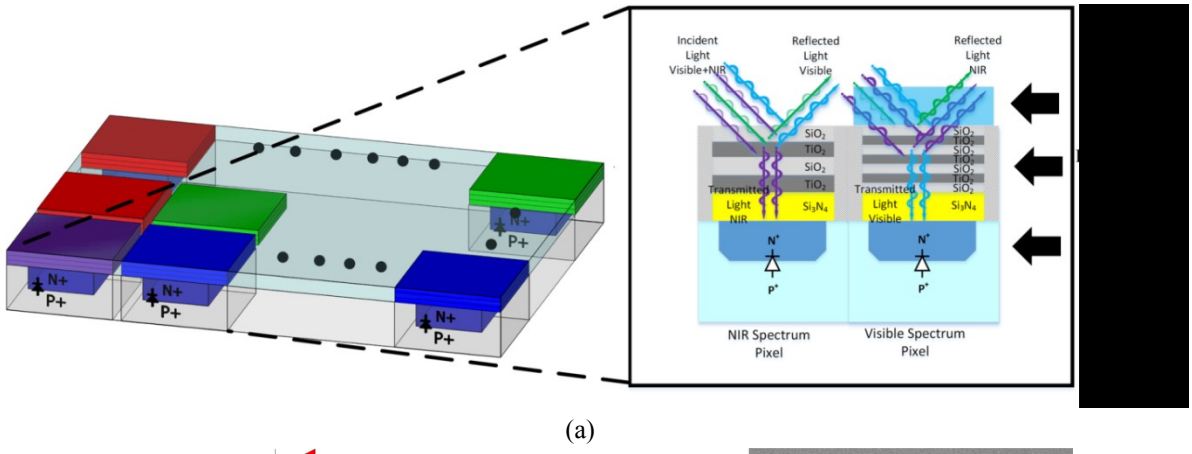

(a)

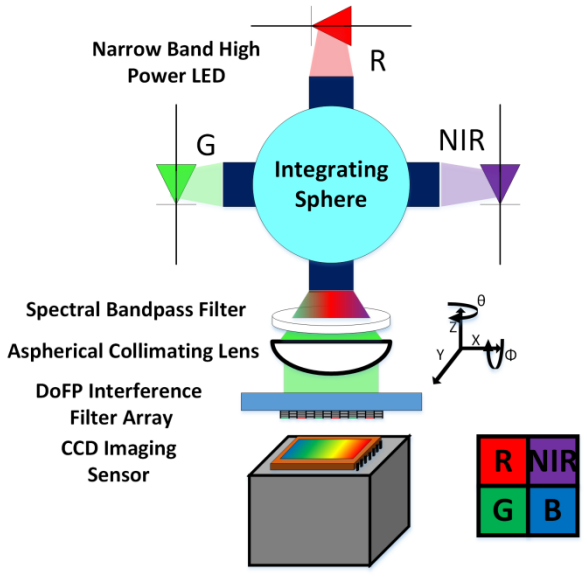

(b)

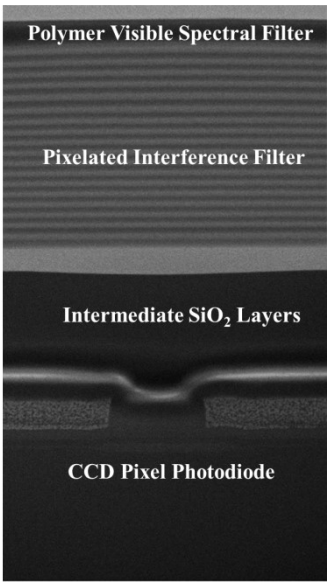

(c)

Figure 4.4. Proposed bio-inspired imaging sensor, (a) sensor structure, (b) alignment setup, and (c) SEM image of the proposed multi-spectral imaging sensor (blue pixel).

A custom-built NIR laser light source is added next to the surgical light source and is used to excite the fluorescent ICG dye molecules. A laser clean-up filter (Semrock, LD01-785/10-25) is added to the NIR laser beam to remove additional NIR wavelengths beyond the necessary excitation light. A free-form collimating lens (designed and fabricated Dr. Rongguang Liang's lab at University of Arizona) and a diffuser (Edmund Optics, 47-994) are also used to achieve large area (15 cm diameter) uniform illumination at a working distance (1 m).

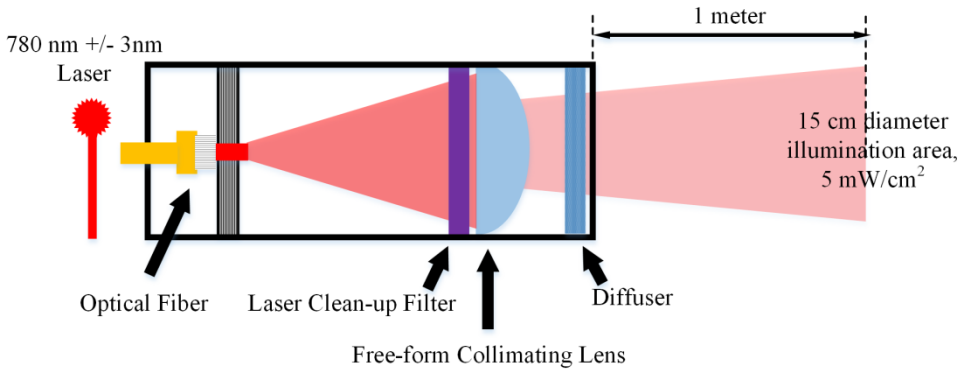

Figure 4.5. Laser illumination source design.

4.3 Spectral Characteristics

The spectral characteristics of the bio-inspired multi-spectral imaging sensor are evaluated in terms of quantum efficiency, transmission, optical density, and divergence response. In order to evaluate the spectral response of the bio-inspired multi-spectral imaging sensor, we used the setup shown in Fig. 4.6. A computer-controlled monochromator (Princeton Instruments Acton SP2150) was used to provide illumination in the visible-NIR spectrum. A 1200 g/mm, 500 nm blaze grating was used. The output slit was adjusted to 2 mm, which corresponds to a FWHM of approximately 8 nm around the central wavelength. An external DC power source (Agilent N5746A) was used to provide constant power supply to the illumination bulb of the monochromator. An integrating sphere (Newport 819D-SF-4) and an aspheric condensing lens (Thorlabs ACL 7560) were used to maintain the uniformity of the monochromator output. The

bio-inspired multi-spectral imaging sensor was placed in an Ethernet connected camera case (Imperx B1620) for transmission of the imaging data to the PC.

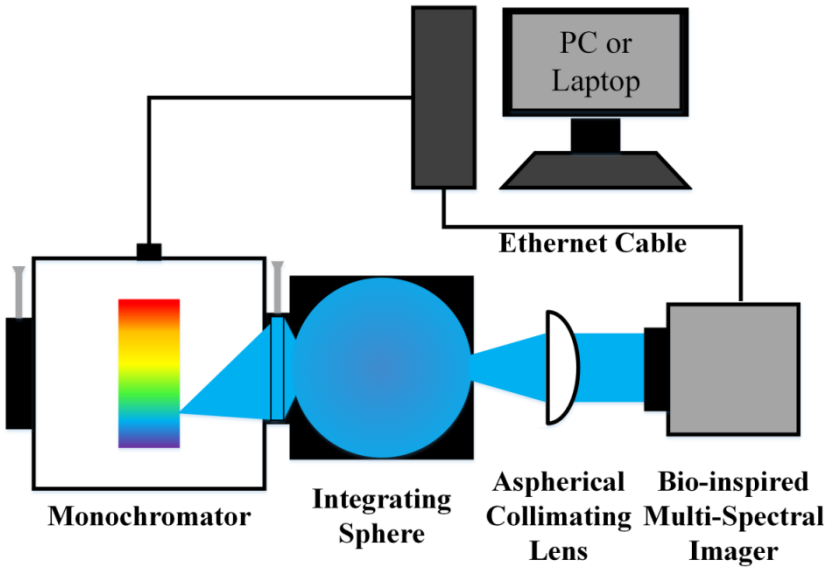

Figure 4.6. Optical setup for performance evaluation.

4.3.1 Quantum Efficiency, Transmittance, and Optical Density Measurement

Quantum efficiency (QE) is used to measure the response of the proposed bio-inspired imaging sensor. As shown in Fig. 4.7(a), the cyan line is the measured QE curve of the pixel of the CCD imaging sensor without a spectral filter; QE of the R, G, and B channels are plotted in corresponding colors, while the QE of NIR channel is plotted in black. The proposed bio-inspired imaging sensor can achieve about 30–40% in the visible spectrum and up to ~18% QE in the NIR spectrum. The difference between the QE response of the pixel without a filter and the pixel with a filter can be further explained using transmittance, as shown in Fig. 4.7(b). The pixelated interference filter deposited on top the CCD pixel array can achieve about 70% transmittance in B and G, 90% in R, and 80% in NIR. In multi-spectral imaging, especially

fluorescence imaging, the optical filter should effectively block unwanted light from other wavelengths to maintain a high signal-to-noise ratio (SNR), and the blocking performance of the optical filter is evaluated using optical density (OD), which is defined in equation 4.3. As shown in Fig. 4.7(c), the NIR pixelated interference filter offers an OD above 2 in the visible spectrum (450–650 nm), the visible R and G pixelated interference filters achieve an OD around 2 in the NIR spectrum (700–900 nm), and the visible B pixelated interference filter has an OD over 1.5 in the NIR spectrum. Therefore, the pixelated interference filter can achieve a similar performance as regular bandpass filter, and its miniature size benefits the compact design of NFIS.

$$OD = -\log_{10}(T) \qquad (4.3)$$

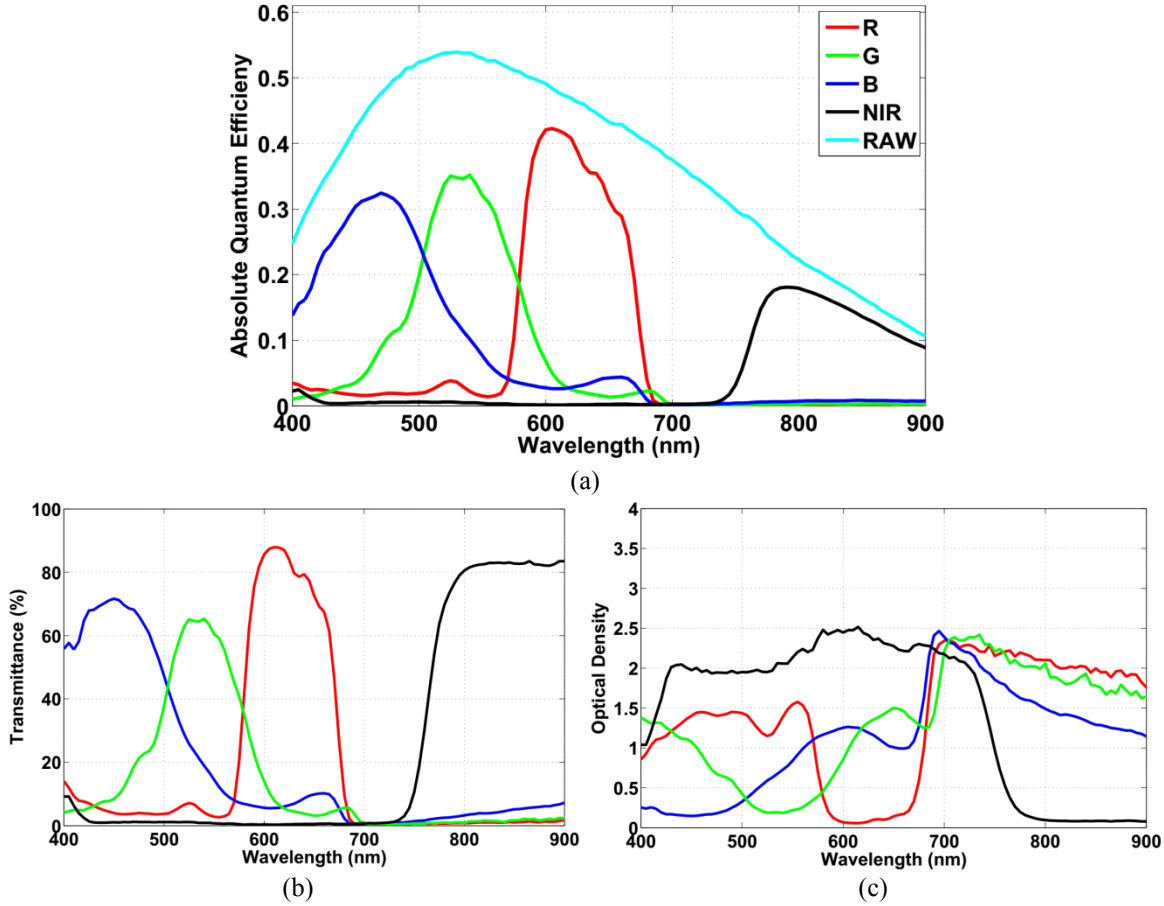

Figure 4.7. Optical responses of the bio-inspired multi-spectral imaging sensor, (a) quantum efficiency, (b) transmittance, and (c) optical density.

4.3.2 Divergent Response

The filtering performance of the interference filter is largely impacted by divergent light from three major aspects. First, the incident angle of the spectral signal changes the light traveling distance of the signal in the interference filter. Equation 4.1 shows that it could affect the selectivity of the interference spectral filter, which affects how well it can pass the light within its passing band and how well it can block the light within its stopping band. Second, it aggravates the optical crosstalk among neighboring pixels in different spectra because the divergent light crosses the optical part of the targeting pixel and is collected by its neighbors more easily. Third, divergent light attenuates the transmittance of the filters and leads to a much lower signal response of the pixel array.

In order to measure the impact of divergent light on the proposed multi-spectral imaging sensor, the experiment was implemented using the setup shown in Fig. 4.5. A motorized rotating base was used to create the effects of divergent light on the imaging sensor. The divergent response from 0 to 5 degrees was investigated in both horizontal and vertical directions, which are shown in Fig.s 4.8 and 4.9. Divergent light creates a slightly different spectral response on the NIR and visible channels of the proposed bio-inspired multi-spectral imaging sensor. Based on Fig. 4.8(a) and Fig. 4.9(a), as the divergent angle of the incoming light increases, the passing band of the NIR interference filter shifts towards a shorter wavelength, and its transmittance decreases dramatically within the NIR spectrum. Visible channels (R, G, and B) show robustness in keeping their passing band from shifting, but they suffer from lower transmittance in the visible spectrum. These observations indicate divergent light leads to a much lower transmittance within the passing band of the filter and an undesired spectral shift on the stopping band. These impacts

lead to poorer signal-to-noise performance of the proposed imaging sensor and lower selectivity of the multi-spectral channel signals.

In our design, two major improvements were made to attenuate the impact of divergent light on the proposed imaging sensor. First, we placed a 780 nm laser notch filter (Semrock, NF03-785E-25) in front of the imaging sensor. This filter prevented reflected laser illumination light from interfering with the NIR fluorescence signal and blocked the leakage signal created by the divergent light. Second, longer focal length lenses with smaller apertures (F2.8 or above, 50 mm or above) were used to achieve less divergent light field on the imaging sensor.

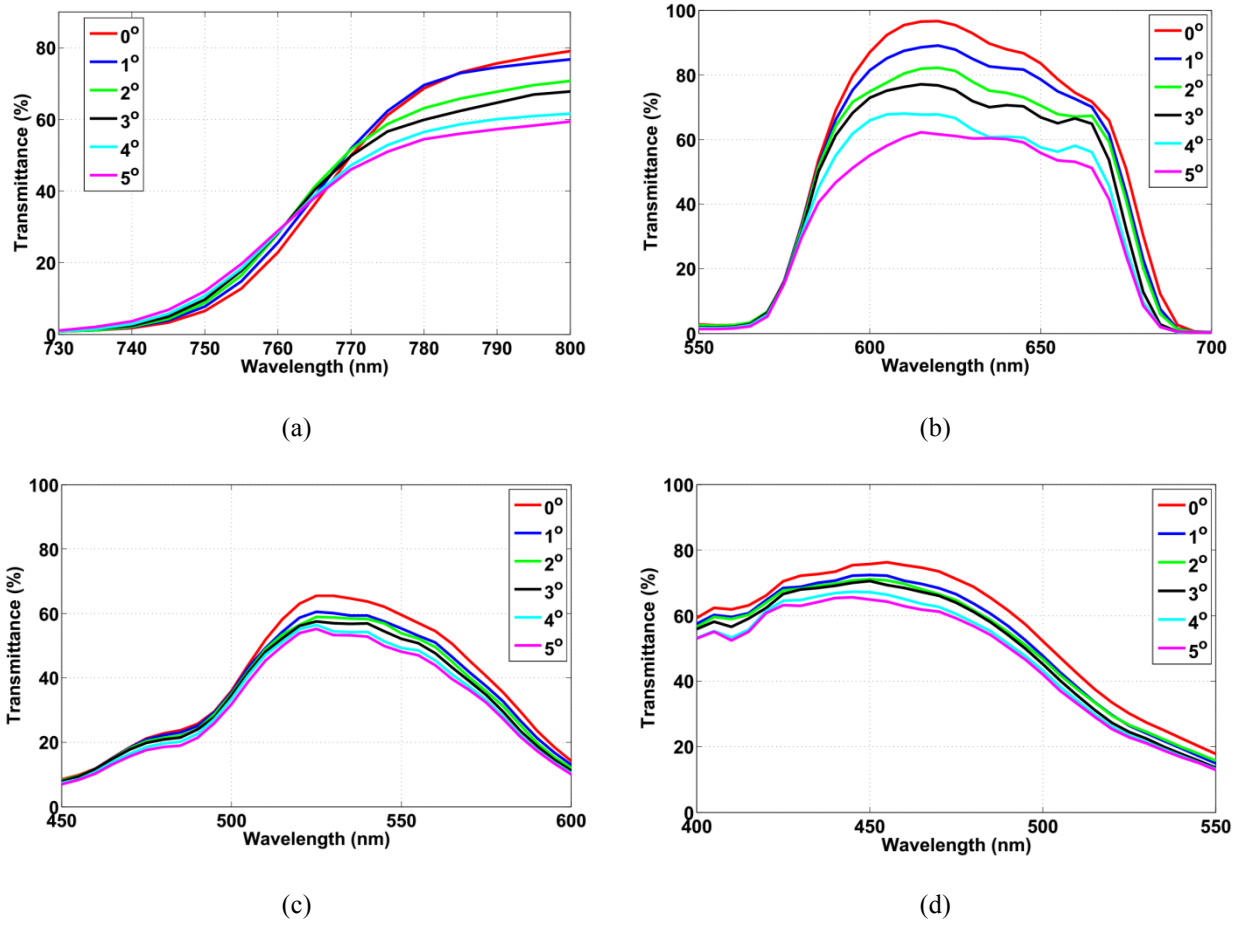

Figure 4.8. Divergent response of the pixelated interference filter in horizontal direction, (a) NIR channel, and (b) R channel, (c) G channel, (d) B channel.

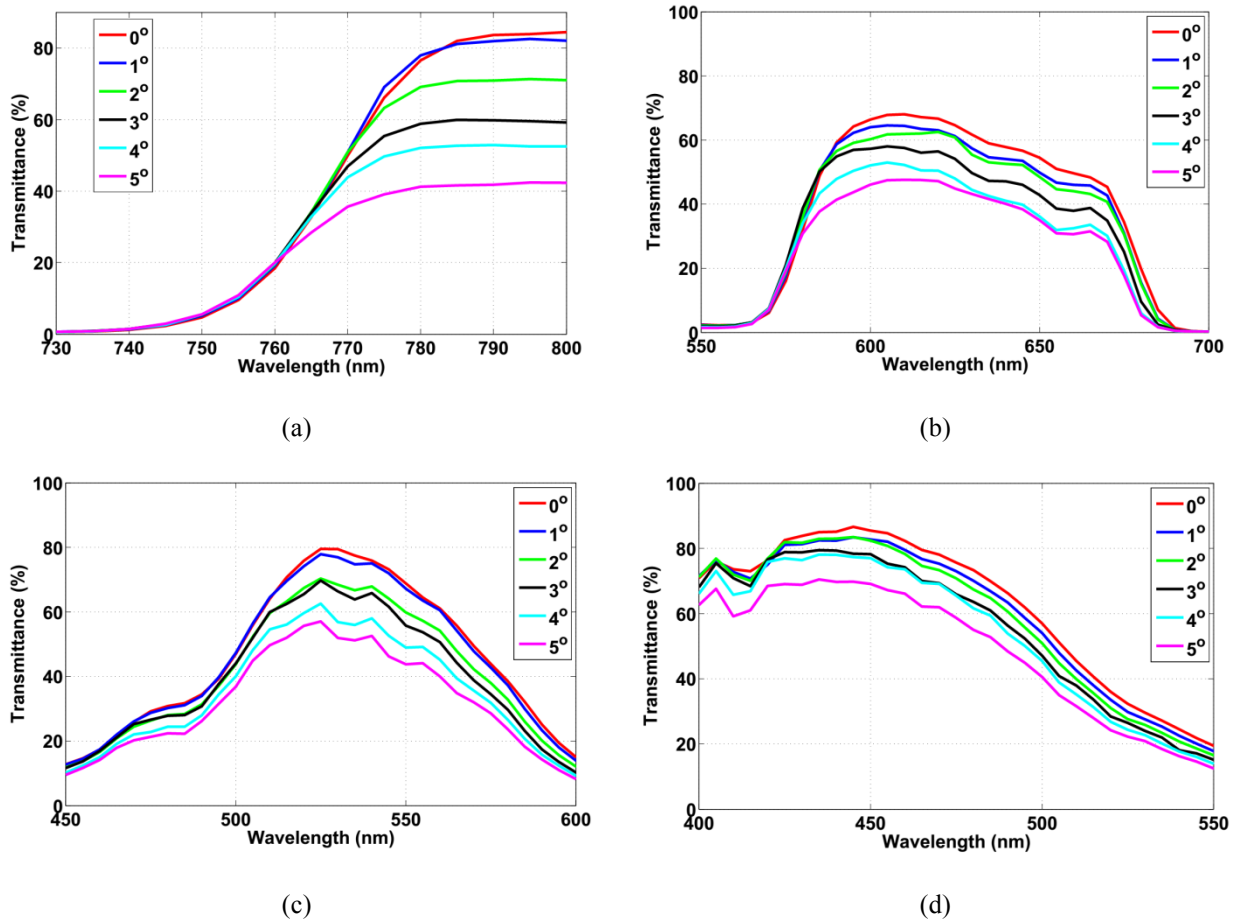

Figure 4.9. Divergent response of the pixelated interference filter in vertical direction, (a) NIR channel, and (b) R channel, (c) G channel, (d) B channel.

4.4 Calibration for Multi-Spectral Imaging Sensor

Calibration of the proposed bio-inspired imaging sensor aims to correct imperfection and variations of the pixelated spectral interference filters during nanofabrication and alignment. Variations in the thickness of a high refractive index material layer and low refractive index material layer and misalignment or dirt existing between filter and photodetector cause the optical properties of the proposed bio-inspired imaging sensor to have non-uniform response. Thus, a mathematical approach is used to perform a first order linear calibration (shown in Equation [4.3]) to pixels on the imaging sensor separately. In equation (4.3), *I* represents the raw

data from imaging sensor; a gain and offset is computed for each single pixel by collecting intensity values of imaging sensor under different exposure time. An imaging sensor will be exposed under a uniform light created by a narrow band LED, optical condensing lens, and integrating sphere. The calibrated results is evaluated in a linearity test and compared with raw image results for visual effect.

$$I_{calibrated} = I \bullet gain + offset \qquad (4.3)$$

Fig. 4.10 shows the calibration results of the proposed multi-spectral imaging sensor under uniform illumination of different spectral channels, i.e. the red, green, blue and NIR pixels in the imaging array. For a given exposure time, as shown in Fig. 4.10 1 ((a)-1, (b)-1, (c)-1 and (d)-1) and 2 ((a)-2, (b)-2, (c)-2 and (d)-2) groups, before applying calibration on the imaging output, pixels in the imaging sensor array had a different intensity response under uniform illumination; after calibration, most pixels obtained nearly identical response from uniform illumination as evident in the histogram plots in the Fig 4.10. For different exposure time, results shown in Fig. 4.10 3 ((a)-3, (b)-3, (c)-3 and (d)-3) and 4 ((a)-4, (b)-4, (c)-4 and (d)-4) groups indicate that the proposed calibration method can greatly improve the linearity of the intensity response while maintaining high uniformity. The symbols and error bars in figures represent mean values of different exposure time and corresponding standard deviations.

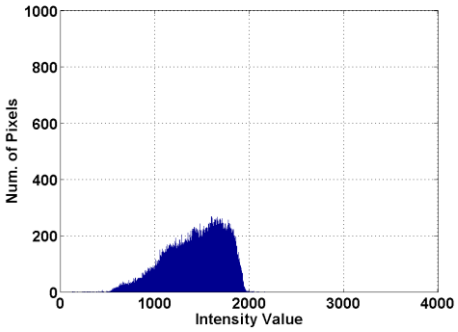

(a)-1

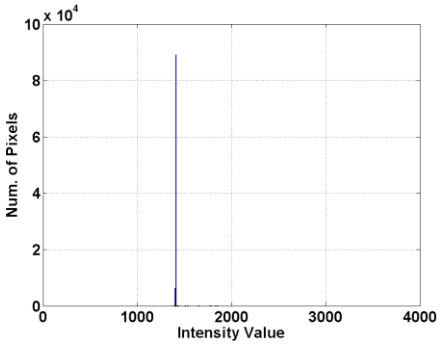

(a)-2

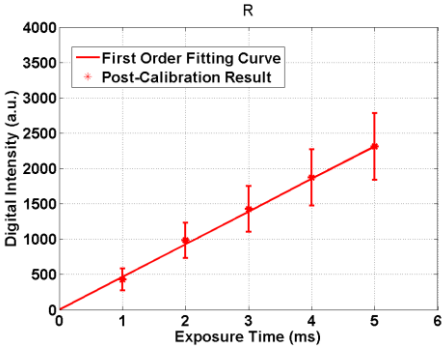

(a)-3

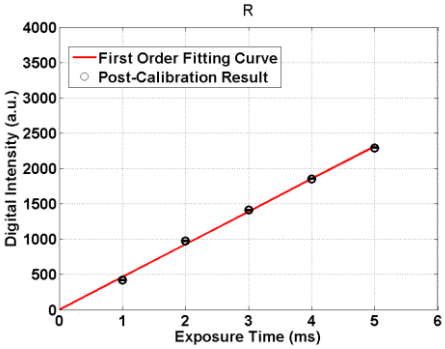

(a)-4

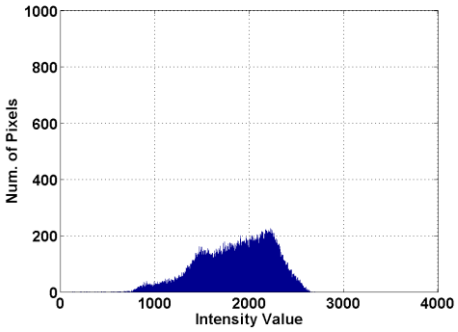

(b)-1

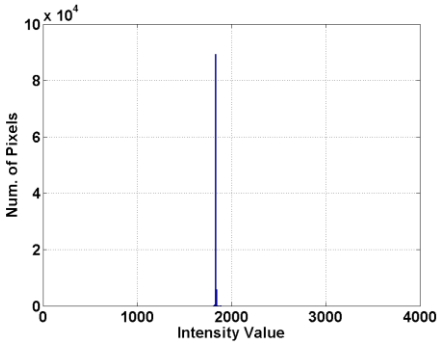

(b)-2

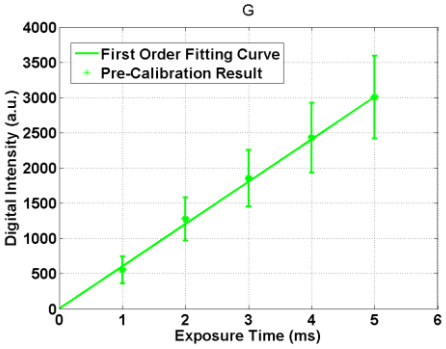

(b)-3

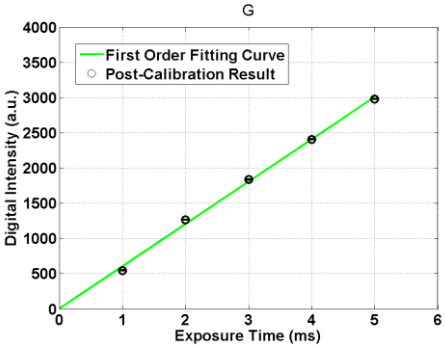

(b)-4

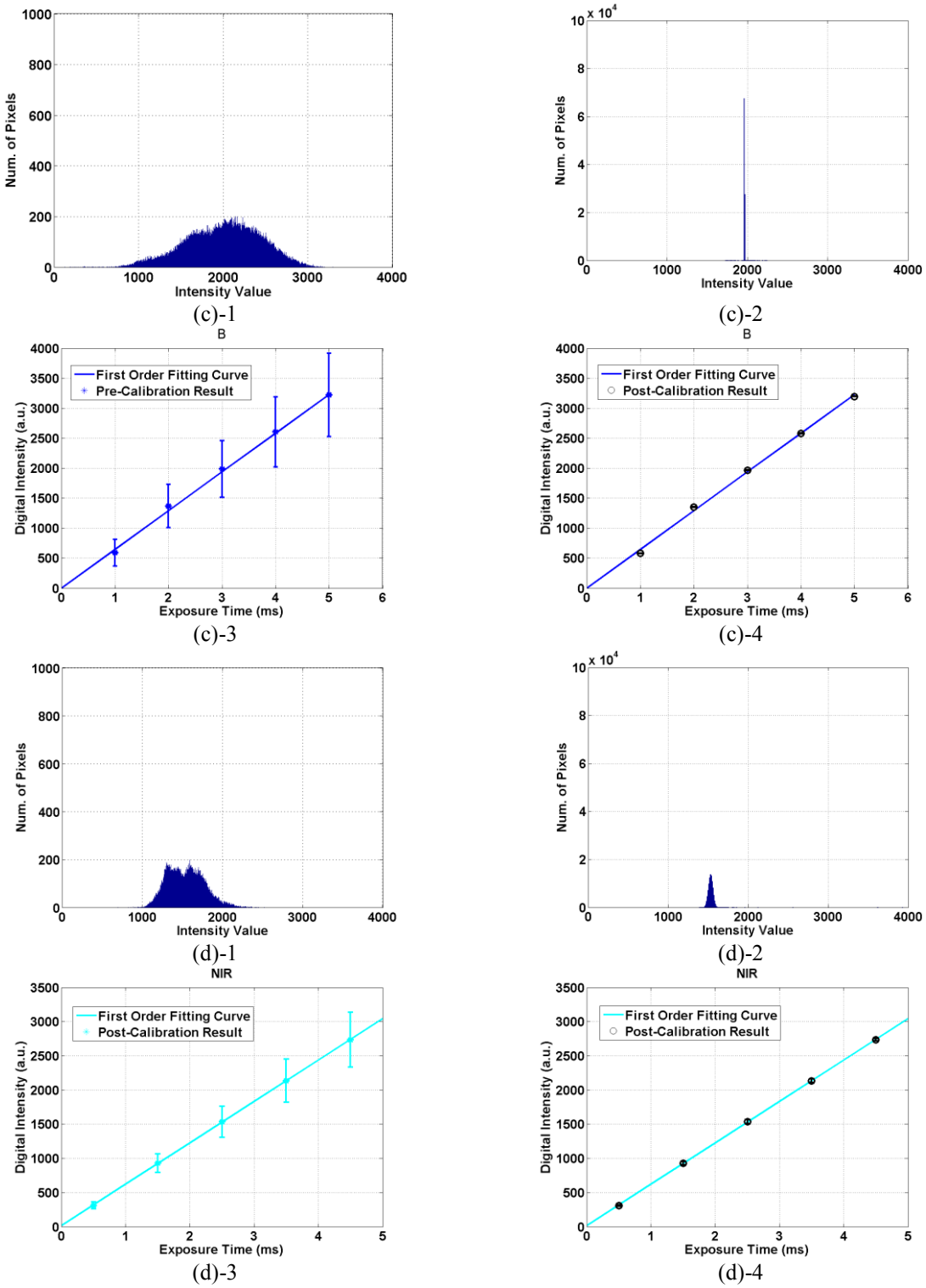

Figure 4.10. Histogram and intensity response of uniform scenes, (a) red pixels, (b) green pixel, (c) blue pixel, and (d) NIR pixel: 1. pre calibration histogram, 2. post calibration histogram, 3. pre calibration intensity curve and 4. post calibration intensity curve.

4.5 Performance Evaluation for Fluorescence Imaging

4.5.1 Detectability

The detectability of the bio-inspired multi-spectral imaging sensor based NFIS was tested by recording the NIR fluorescent signal responses for different ICG concentrations and different LS301 [22][25][26] concentrations dissolved in 100% dimethyl sulfoxide (DMSO). ICG has been widely used for NIR fluorescence since it has been FDA approved (1959) for 57 years. LS301 is a tumor-targeted contrast agent developed at WUSTL and is currently in preclinical trials. The vials with different ICG and LS301 concentrations were placed 1 m from the imaging sensor. A control vial with pure DMSO was also imaged and denoted as a background signal. The proposed NFIS was tested with 30 ms exposure time to ensure real-time imaging of 30 fps. The diluted samples were illuminated with a 780 nm excitation light source under two different optical power outputs (5mW/cm^2 and 10mW/cm^2). The mean and standard deviasion of the signal-to-background ratio (SBR) of the imaging system was calculated from a 30 x 30 pixel region. The experiments were repeated with three different samples with the same ICG-DMSO and LS301-DMSO concentrations.

The detectability measurement of the proposed NFIS is presented in Fig. 4.11(a). It shows the SBR of the proposed NFIS on different ICG and LS301 concentrations ranging from 500 pM to 50 uM; the vial with 100% DMSO was used as the background control negative sample. Higher illumination power increased the SBR from the same fluorescence sample. Defining the detectability of a system to be SBR = 2 [27], the proposed NFIS can detect 0.7 nM of ICG and 10 nM of LS301 under an excitation illumination of 10 mW/cm^2. Using an excitation illumination of 5 mW/cm^2, the minimal detectability is 1 nM and 15 nM for ICG and LS301, respectively. Furthermore, higher excitation power leads to lower SBR at higher concentrations,

which occurs because the fluorescent signal is saturated while the background signal is higher. Therefore, selecting a proper optical power for the illumination module is always a tradeoff between keeping a high SBR and a high signal response.

Fig. 4.11(a) also indicates that ICG achieves a higher signal response and SBR compared to LS301. The reason for this is that LS301 is a cypate-based contrast agent, which has lower quantum efficiency than ICG. Furthermore, as a tumor-targeted contrast agent, LS301 will clear from most animal organs 24 h after injection, which leads to a much higher fluorescent contrast in *in vivo* study. Hence, LS301 is used in our in vivo study in mice to further validate the performance of the proposed multi-spectral imaging sensor based NFIS.

4.5.2 Sensitivity

The sensitivity of the proposed NFIS was measured by using SNR. As explained in the previous chapter, SNR is the ratio of the signal response to the variation of the signal responses. Higher SNR indicates better system sensitivity on distinguishing signal change. Since auto-fluorescence and background reflection commonly exist in tissues and bio-materials, it is important to eliminate their influence on signal response. As shown in equation (2.5), the background signal, which was measured using a 100% pure DMSO solvent, is subtracted from the signal response.

In our experiment, sensitivity of the proposed NFIS was measured by computing the SNR of the NIR fluorescent signal responses of different ICG concentrations in DMSO. The proposed NFIS was setup at a 1 m working distance and 30ms exposure time per frame. ICG-DMSO concentration samples were illuminated under two different illumination power (5 mW/cm^2 and 10 mW/cm^2). For each concentration, 128 frames of images were collected to compute the signal intensities and deviation (considered as noise).

Fig. 4.11(b) shows the sensitivity results of the proposed NFIS. Using the high performance CCD imaging sensor, the noise part is lower than CMOS imaging sensor. Therefore, the SNR of the proposed NFIS is higher than the three other prototypes that were introduced in previous chapters. The SNR can reach up to 50 dB under near-saturation condition. Comparing different illumination power, higher illumination power leads to slightly higher SNR. SNR difference under different illumination becomes smaller in ICG samples with higher concentration, since the imaging sensor is approaching saturation, and fewer photons are collected and converted to electrons by the photodiode. Furthermore, Fig. 4.11(b) also shows that the SNR of the proposed NFIS can achieve more than 22 dB when ICG concentration is above 1nM when the system is running at 30 ms exposure time. This 22dB SNR result is much higher than the confidence level of a normal signal distribution, which is defined as 6dB for 95% and 9.5dB for 99.7% (shown as a green dotted line in Fig. 4.11[b]) [50].

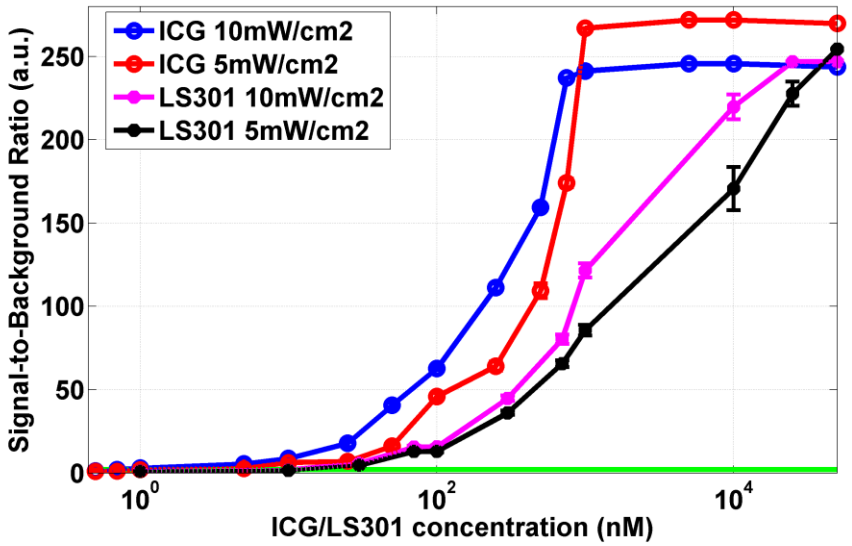

(a)

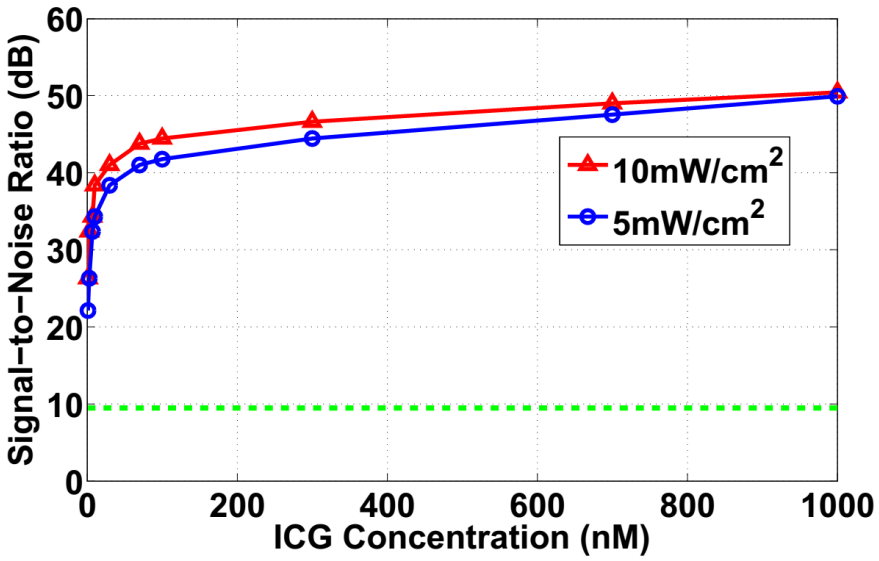

(b)

Figure 4.11. (a) Detectability test with SBR measurement using ICG-DMSO and LS301-DMSO, green line shows the SBR = 2 threshold. (b) Sensitivity test with SNR measurement using ICG-DMSO, green line shows the SNR=9.5 dB threshold.

4.6 Animal Study and Human Study

4.6.1 *In Vivo* Mouse Study for Breast Cancer

The proposed NFIS was evaluated through in vivo cancer imaging of a transgenic PYMT mice model with spontaneous breast cancer. The female carriers of this model develop palpable mammary tumors as early as 5–6 weeks. When the main tumors were at least 10 mm in size, the mice were injected with 10 µl of 60 uM tumor-targeted NIR fluorescence contrast agent LS301, via the tail vein. Images were taken 24 h post injection of LS301. During the in vivo study, the camera with the proposed multi-spectral imaging sensor was set up at 1 m working distance, and the illumination module was placed at a 50 cm distance with 5 mW/cm^2 illumination power. All images were captured at 30 ms. During the imaging experiments, the mouse was kept anesthetized using a cocktail of ketamine/xylazine or through intubation of isofluorane. Following the imaging experiment, the mouse was sacrificed through cervical dislocation, and its organs and tumors were harvested, imaged, and preserved for histologic evaluation.

Fig. 4.12 shows the test results of non-invasive mouse object. Fig. 4.12(a) is the NIR fluorescent signal in false JET color with proper threshold, which precisely reveals the locations of the main tumor and liver (not being considered); Fig. 4.12(b) is the color image of the mouse object. Fig. 4.12(c) shows the image overlay result by combining both NIR and visible channels. The main tumor is clearly detected, and its margins in NIR and visible channels match accurately. Histology experimental result using fluorescence microscopy is shown in Fig. 4.12(d), which validates imaging results captured by our proposed NFIS. Its corresponding hematoxylin and eosin (H&E) staining image is shown in Fig. 4.13(d).

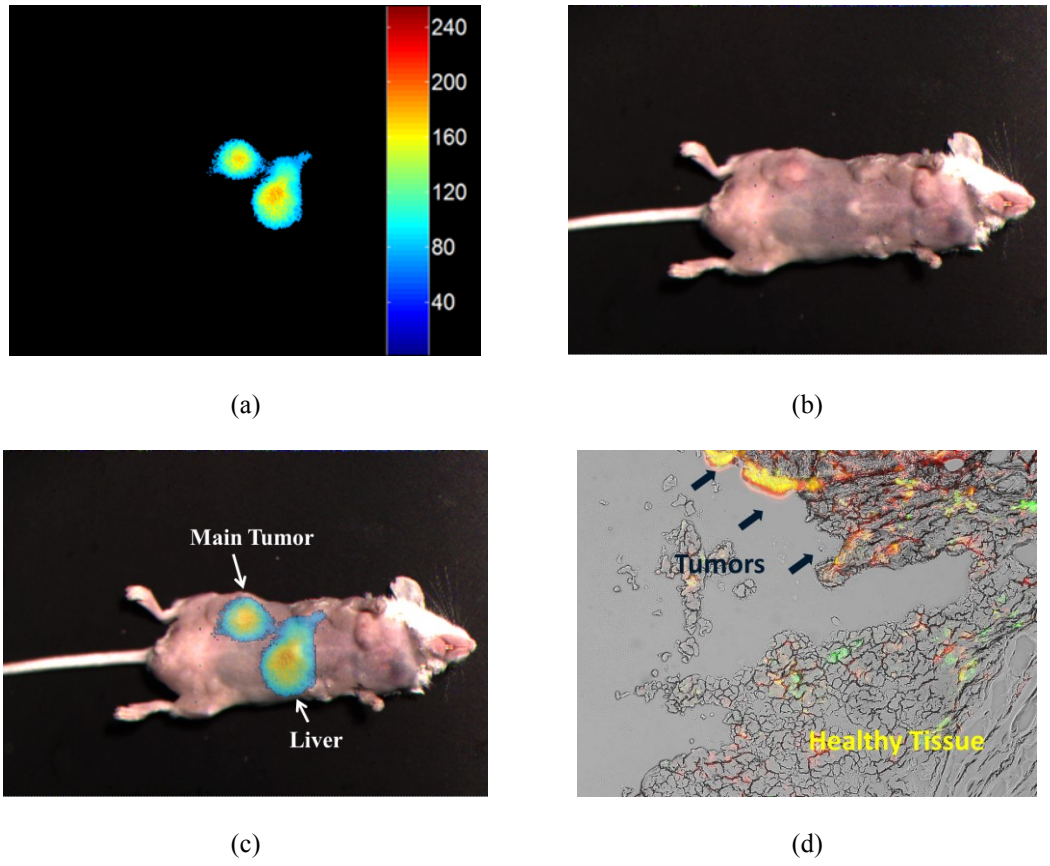

Figure 4.12. Mouse model study at 30 ms exposure time, (a) NIR channel, (b) visible channel, (c) NIR-visible overlay channel, and (d) Fluorescence microscopy image revealed good co-localization (yellow) of iRFP signal (green) and LS301 fluorescence (red)..

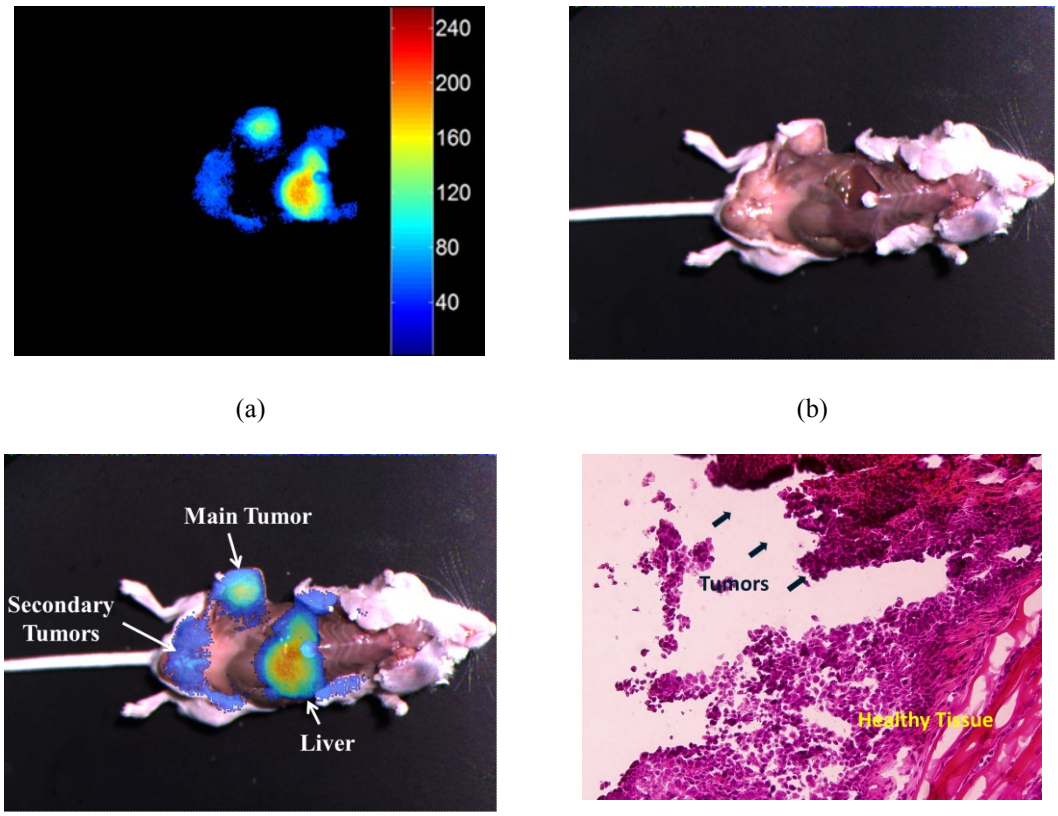

Figure 4.13. Mouse model study at 30 ms exposure time, (a) NIR channel, (b) visible channel, and (c) NIR-visible overlay channel, and (d) A representative image of tumor margin tissue with H&E staining (same slide of Fig. 4.12(d)).

Fig. 4.13 shows the imaging results of the same mouse object when the skin is deflected to reveal the tumors. NIR fluorescence signal precisely locates the main tumor and liver and also highlights the secondary tumors around the mouse's belly area. A stronger fluorescence signal can be achieved with a higher illumination source or longer exposure time.

4.6.2 Human Pilot Study for Sentinel Lymph Node Mapping

A human pilot study is used to examine the performance of the proposed NFIS in clinical settings. Currently, the proposed NFIS has been tested on patients with breast cancer (N=6) undergoing lumpectomy and partial mastectomy for sentinel lymph node mapping. Before the

surgery, as a commonly used visual tracer, ICG is injected into patient's tumor area with a lower concentration (5 mg/ml, 5 ml) for NIR fluorescence imaging, and the region was under site massage for 5 mins. At 10–15 mins post injection, surgeons use the proposed NFIS to observe sentinel lymph node area. The proposed NFIS was set up at 1 m working distance, and the illumination module was placed at 1 m distance. All images were captured at 30 ms. In vivo sentinel lymph node mapping results of a patient with breast cancer using the proposed NFIS are shown in Fig. 4.14. Fig. 4.14(a) is the NIR signal with proper threshold (threshold value equals to 40). Fig. 4.14(b) is the visible channel image. Fig. 4.14(c) shows the image co-registration result by combining both NIR and visible channel. The sentinel lymph node is clearly detected, and its margins in NIR and visible channels match accurately. An additional NIR fluorescent signal was also observed from the breast fat tissue, which proved to be the ICG residue left in the fat tissue in a post-operative pathology test.

(a) (b) (c)

Figure 4.14. Human pilot study on sentinel lymph node, (a) NIR, (b) visible, and (c) NIR-visible co-registered results.

Ex vivo sentinel lymph node mapping using the proposed NFIS is shown in Fig. 4.15. Fig. 4.15(a) is the NIR signal with a proper threshold (threshold value equals to 40). Fig. 4.15(b) is the visible channel image. Fig. 4.15(c) shows the image overlay result by combining both NIR

and visible channels. A higher NIR fluorescent signal was observed because of the higher illumination of the tissue with the NIR laser light source. Using histologic analysis as the gold standard, our proposed multi-spectral imaging sensor–based NFIS with ICG injection for sentinel lymph node mapping maintained a 100% matching rate. Furthermore, no pre-alignment or reference point adjustment is required a system setup, which shortens the lead time during the imaging session and further lowers the potential infection chance for the patient.

(a) (b) (c)

Figure 4.15. Human pilot study on sentinel lymph node, (a) NIR, (b) visible, and (c) NIR-visible co-registered results.

4.7 Performance Comparison of Different NFISs

We developed four NIR fluorescence imaging systems for image guided surgery and other potential clinical uses. These NFISs are designed to achieve compact, highly sensitive real-time fluorescence imaging and precise NIR-visible information co-registration. The first two NFIS prototypes used the post-processing based multiple camera solution. For the first NFIS, a threshold-based two-camera system was developed for NIR-visible dual channel imaging, while external compact LED trackers were used to provide reference points to both NIR and visible image channels. This method is an intuitive solution with a simple threshold detection algorithm

running at a low computational cost. However, it requires physical LED trackers to be placed close to the object, which may raise safety issues for clinical applications.

For the second NFIS, a feature matching–based three camera system was developed to achieve a "tracker-free" solution using the SIFT feature matching method. This solution doesn't have additional requirements for system setup; however, heavy computational loads caused by the SIFT feature matching algorithm lead to a slow disparity refresh rate (~ 6 FPS). Additionally, the randomness of the feature generation caused abrupt disparity changes during multi-spectral channels co-registration. The third NFIS prototype used the division-of-amplitude solution. For this NFIS, precise and adjustable NIR-visible co-registration was achieved by using a 3D-printing case and post-software processing. This solution can realize a simple and robust setup for the application; however, precise alignment is needed to implement each single camera to achieve an error-free NIR-visible co-registration. In order to achieve a precise multi-spectral co-registration, compact design, and real-time multi-channel imaging, we developed a bio-inspired multi-spectral imaging sensor as a single chip solution. This design mimics the ommatidium structure in monarch butterfly's compound eye to simultaneously capture NIR and visible information. In this proposed multi-spectral imaging sensor, pixelated spectral inference filters are integrated with a CCD imaging sensing unit.

The performance comparison of the four NFISs are listed in Table 4.1, the best performing parameter in each category is marked in blue. All four NFISs have a light weight compared with the commercial NFISs; currently, the bio-inspired multi-spectral imaging sensor–based camera doesn't have the lightest weight. However, a CMOS version is being developed to achieve it. For frame rate, all four systems can achieve more than 27 FPS display rate while maintaining 30 ms exposure time, but feature matching–based three camera NFIS suffers from a slow refresh rate of

feature matching due to the computational load. For detectability, the three NFISs can detect 30-50 nM ICG sample for SBR=2, while the bio-inspired NFIS can detect down to 1nM ICG. For sensitivity, the proposed bio-inspired multi-spectral imaging sensor reached up to 50 dB SNR, which also outperformed other NFISs. Furthermore, the proposed multi-spectral imaging sensor provided a simple solution to achieve single pixel pitch accuracy of multi-spectral information co-registration. By comparison, the division-of-amplitude solution ideally can achieve precise multi-spectral information co-registration. However, real alignment causes up to a dozen pixel disparity errors, and it also requires applying a disparity offset for each setup.

Table 4.1. Performance Comparison of the Three Proposed Camera Systems

	FLARE [62]	**Threshold detection–based two camera NFIS**	**Feature matching–based three camera NFIS**	**Beam splitter–based signal camera NFIS**	**Proposed bio-inspired multi-spectral imaging sensor–based NFIS**
Weight (g)	4 kg	30 g	45 g	50 g	300 g
Resolution	640 by 480	753 by 480	753 by 480	753 by 480	720 by 534
Frame Rate	15 FPS	27 FPS	27 FPS	27 FPS	30 FPS
Detectability (SBR)	N/A	30 nM	30 nM	50 nM	1 nM
Sensitivity (SNR)	N/A	45 dB	45 dB	45 dB	50 dB
NIR-visible co-registration accuracy	~0 mm (after prefect alignment)	<2 mm (65 cm or farther)	<2 mm (65 cm or farther)	~0 mm (after prefect alignment)	<1 pixel pitch

4.8 Conclusion

In this chapter, we presented a new butterfly-inspired multi-spectral imaging sensor and the corresponding NFIS for NIR fluorescence imaging. In this imaging sensor, pixelated spectral

interference filters were integrated with a CCD imaging sensing unit. The pixelated spectral filters were fabricated via a carefully optimized nanofabrication procedure and integrated with a CCD imaging array using custom off-chip alignment technology. The NFIS has been experimentally verified and optimized for high signal-to-background fluorescence imaging using an analytical approach. The NFIS is integrated with a wearable goggle for easy integration in the operating room. The NFIS has undergone a small animal study and clinical trials at WUSTL Medical School.

Our bio-inspired multi-spectral imaging sensor solution offers a compact and robust design and applicability in different clinical applications that need multi-spectral imaging technology, such as neuron recording, endoscopy [63], laparoscopy [50] and polarization combined cancer imaging [64]. A CMOS-based imaging sensing solution will also be explored for a more compact and lower cost NFIS solution in future.

Chapter 5. Image Interpolation Algorithms for Polarization and Multispectral Imaging Sensor

Our bio-inspired, multispectral imaging sensor uses a so-called division-of-focal-plane (DoFP) filter pattern for sensing multispectrum information. This pattern is also widely used in different types of imaging sensor design, such as the Bayer pattern in regular color imaging sensors and the four-polarimeter pattern in real-time polarization imaging sensors. As an on-chip multichannel solution, DoFP pattern contributes a much more compact and simplified electro-opto imaging sensor design. However, low spatial resolution and the instantaneous field-of-view error are two major limitations of DoFP pattern. To overcome them, various image interpolation algorithms have been studied and evaluated for our multispectral imaging sensor and DoFP polarization imaging sensor.

5.1 Background

There are three fundamental properties of light: intensity, wavelength, and polarization. The first two properties are encoded by our visual system as brightness and color, and current imaging technology aims to replicate them in high resolution in the visible spectrum with low spatial and temporal noise sensors. However, polarization of light and light out of the visible spectrum have largely been ignored by imaging technology, in part by the fact that the human eye is polarization insensitive. In recent biomedical and clinical research, people have found that polarization can be used effectively in cancer imaging, such as in colorectal cancer [65], breast cancer [66], skin cancer [67], and others [68]. Therefore, polarization imaging offers a new imaging modality to image guided surgery applications. Furthermore, as mentioned in previous

chapters, multispectral imaging using light out of the visible spectrum also leads to huge advantages in such fields as current cancer imaging [17] and blood perfusion research [69].

Due to recent advancements in nanotechnology and nanofabrication, polarization imaging sensors for the visible spectrum, known as division-of-focal-plane (DoFP) polarimeters, have emerged on the scene [40], [70]–[73], providing real-time, highly accurate polarization imaging results that are compact in size. Our proposed bioinspired multispectral imaging sensor also performs real-time multispectral imaging with precise multispectral channel information co-registration. These imaging sensors monolithically integrate and combine pixelated polarization or spectral filters with an array of imaging elements. The pixelated polarization filters are composed of metallic nanowires, typically oriented at 0º, 45º, 90º, and 135º, while the pixelated multispectral filters are composed of different vertically stacked interference filter structures for different spectrum imaging. Examples of these types of polarization and multispectral imaging sensors are presented in Figure 5.1. One of the main advantages of DoFP imaging sensors is the capability of capturing multichannel (polarization or spectrum) information with every frame. The polarization and multispectral information captured by this class of imaging sensors can be used to extract various parameters from an imaged scene, such as microscopy for tumor margin detection [74], 3-D shape reconstruction from a single image [75], underwater imaging [76], material classification [77][78], and cancer diagnosis [79][80].

A block diagram of a typical DoFP polarization imaging sensor for infrared or visible spectrum is presented in Fig. 5.1(a) [40]. In a neighborhood of 2x2 pixels, four different polarization filters, offset by 45 degrees, are deposited on individual photoreceptors. This neighborhood of four pixels is typically referred to as a "superpixel." An analogous concept was realized in our proposed bioinspired, multispectral imaging sensor by applying the interference filter structure

directly on top of the imaging elements of the charge coupled device (CCD). An example of the multispectral interference filter pattern is presented in Fig. 5.1(b). The integration of color filters with an array of imaging elements has created robust and compact color imaging sensors. However, the color information from the imaged scene is sub-sampled and can lead to inaccurate color reconstruction. In order to recreate high-resolution color images from low-resolution prime polarization and multispectral images, various interpolation techniques were introduced in the previous chapter. Since the inception of the Bayer pattern in the 1970s [81], research into the visible color interpolation area has created a tremendous body of literature whose main purpose is recovering as much missing color information in the imaging array as possible, with a high degree of accuracy [82][83]. As such, we can take advantage of these existing interpolation algorithms to explore the new interpolation algorithms used for multispectral and polarization imaging [84].

There are two main disadvantages of the DoFP-based imaging sensor: loss of spatial resolution and inaccuracy of the captured information. Due to sampling of the imaged scene with four spatially distributed, pixelated polarization or spectral filters, the instantaneous fields of view of the neighboring pixels in a 2x2 superpixel configuration can be different from each other. Taking the DoFP polarization image as an example, the computed polarization information, such as the first three Stokes parameters, angle of polarization, and degree of linear polarization, will contain an error from the true polarization signature of a target. Furthermore, the four types of polarization pixels, which are distributed throughout the imaging array, sub-sample the imaged environment by a factor of four and lead to loss of spatial resolution [85]. These two shortcomings need to be addressed in order to take full advantage of the real-time imaging capabilities of DoFP polarization imaging sensors.

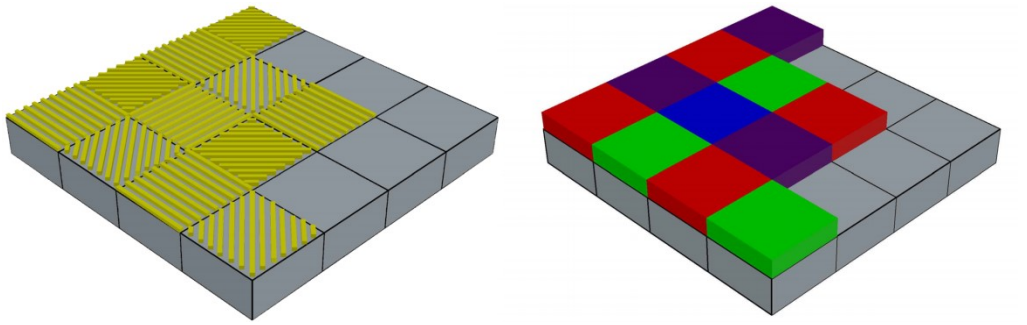

(a) (b)

Figure 5.1. Block diagrams of division-of-focal-plane (a) polarization sensor—0°, 45°, 90°, and 135° orientations—and (b) multispectral imaging sensor—red, green, blue, and near infrared (shown in purple).

In this chapter, we present four interpolation algorithms to overcome the two shortcomings of DoFP multispectral and polarization imaging subsection sensors. Specifically, linear polarization computation is introduced in subsection 5.2. The four interpolation algorithms for images produced by DoFP polarization imaging sensors are presented in subsection 5.3: bilinear interpolation[85], bicubic spline interpolation [21][22], bicubic convolution interpolation [88], and a new, gradient-based interpolation algorithm with adaptive threshold selection [89]. The performance of non-gradient-based interpolation algorithms is first evaluated using modulation transfer function in subsection 5.4. The performances of different interpolation algorithms are evaluated in terms of spatial resolution and accuracy of the reconstructed images, for both synthetic and real polarization images, in subsection 5.5 for multispectral imaging sensors and subsection 5.6 for DoFP polarization imaging sensors.

5.2 Linear Polarization Computation

DoFP imaging sensors capture both the intensity and polarization information of an imaged scene with every frame. In terms of polarization properties of an imaged scene, two polarization sub-properties are typically of interest: angle of polarization (AoP) and degree of linear

polarization (DoLP). Intensity, DoLP, and AoP are computed using Equations (5.1) through (5.3), respectively:

$$Intensity = (1/2)\bullet \quad I(45^o) + I(90^o) + I(135^o)) \tag{5.1}$$

$$DoLP = \sqrt{\left(I(0^o) - I(90^o)\right)^2 + \left(I(45^o) - I(135^o)\right)^2} \Big/ Intensity \tag{5.2}$$

$$AoP = (1/2)\bullet \quad \left(I(45^o) - I(135^o)\right) \Big/ \left(I(0^o) - I(90^o)\right) \tag{5.3}$$

where $I(x^o)$ is the intensity of the light wave filtered with a linear polarization filter in the x° orientation. Following Equations (5.1) through (5.3), an imaging sensor capable of recovering polarization information from a scene has to sample the imaged environment with four linear polarization filters offset by 45º. In the case of DoFP polarization sensors, the linear polarization filters are pixelated and embedded in the focal plane of the imaging sensor [see the block diagram in Fig. 5.1(a)]. The fourth Stokes parameter is not captured with the sensor described in Fig. 5.1(a), due to the lack of quarter-wave retarder embedded at the pixel level in the imaging array. These filters can be incorporated in future versions of DoFP polarization imaging sensors by adding pixelated, plasmonic quarter-wave retarders in combination with linear polarization filters [90]–[93].

5.3 Interpolation Algorithms

5.3.1 Bilinear Interpolation Algorithm

Bilinear interpolation algorithms are among the most common techniques used in image processing, due to their computational simplicity. In DoFP polarization imaging sensors, bilinear interpolation is computed separately on the four low-resolution images recorded with different polarization filters offset by 45°. For example, a 1-megapixel (MP) DoFP polarization sensor captures 0.25 MP for each of the four linear polarization filters (0°, 45°, 90°, and 135°). The

bilinear interpolation algorithm is then used to up-sample these 0.25-MP components back to the full resolution (1 MP) of the camera.

Figure 5.2 presents a neighborhood of 4x4 pixels in a typical DoFP imaging sensor composed of four different pixilated polarization filters. For this pixel neighborhood, the pixel in location (2,2) records the intensity of the light wave after filtering it with a linear polarization filter oriented at 90°. At this pixel location, the intensity values of the filtered light waves with 0°, 45°, and 135° polarization filters are estimated via bilinear interpolation from the surrounding pixels. Equations (5.4) through (5.6) present the formulas used to estimate these pixel values:

$$I_0^p(2,2) = \frac{1}{4}\left[I_0(1,1) + I_0(1,3) + I_0(3,1) + I_0(3,3)\right] \quad (5.4)$$

$$I_{45}^p(2,2) = \frac{1}{2}\left[I_{45}(1,2) + I_{45}(3,2)\right] \quad (5.5)$$

$$I_{135}^p(2,2) = \frac{1}{2}\left[I_{135}(2,1) + I_{135}(2,3)\right] \quad (5.6)$$

In Equations (5.4) through (5.6), the 0° interpolated intensity value at pixel location (2,2) is an average intensity value of the four adjacent diagonal pixels; the 45° interpolated intensity value is the average intensity of the two adjacent vertical pixels; and the 135° interpolated intensity value is the average intensity of the two adjacent horizontal pixels. Equations (5.4) through (5.6) are modified slightly when computing the interpolated pixel values at locations (2,3), (3,2), and (3,3) in the imaging array, due to differences in the linear polarization filters in the immediate pixel neighborhood.

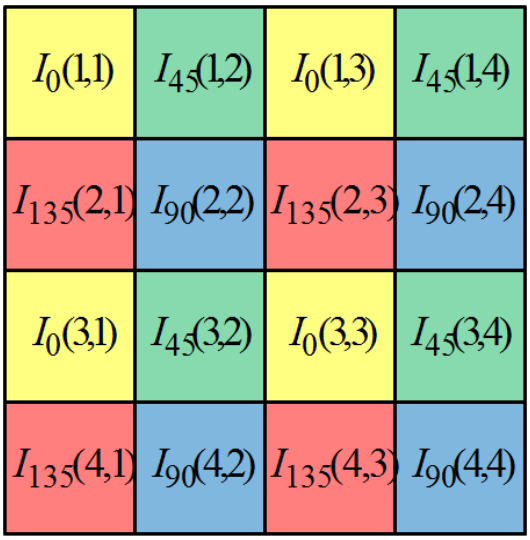

Figure 5.2. A 4x4 interpolated block in a DoFP polarimeter.

5.3.2 Bicubic Spline Interpolation Algorithm

The bicubic spline interpolation algorithm, a common algorithm used in color images, displays superior improvements in its performance over bilinear interpolation. However, the cost is increased computational complexity [94]. The bicubic spline interpolation algorithm can be applied easily to the four low-resolution polarization images produced by a DoFP polarimeter. This interpolation algorithm is applied first in the horizontal direction, followed by interpolation in the vertical direction. The bicubic spline interpolation algorithm computes new values from a low-resolution image by fitting a third-order polynomial, $f_i(x)$, between two neighboring pixels (x_i and x_{i+1}) with polarization filters oriented at the same angle. The third-order polynomial, $f_i(x)$, can be described by Equation (5.7):

$$f_i(x) = a_i + b_i(x - x_i) + c_i(x - x_i)^2 + d_i(x - x_i)^3 \qquad (5.7)$$

where x is the spatial location of the pixel value that is being interpolated and is typically halfway between x_i and x_{i+1}. Coefficients a_i, b_i, c_i, and d_i are defined as follows:

$$a_i = I(i,j) \qquad (5.8)$$

$$b_i = I(i+1,j) - I(i,j) - \frac{M_{i+1} - M_i}{6} \qquad (5.9)$$

$$c_i = \frac{M_i}{2} \qquad (5.10)$$

$$d_i = \frac{M_{i+1} - M_i}{6} \qquad (5.11)$$

In Equations (5.8) through (5.11), I(i,j) is the intensity value of a pixel at location (i,j) and M_i is the second derivative of function $f_i(x)$ [i.e., $M_i = f_i''(x)$]. The coefficients described by Equations (5.8) through (5.11) are derived by placing the following constraints on interpolated curve $f_i(x)$:

(a) Function $f_i(x)$ should be continuous between pixels x_1 and x_n

(b) The first derivative of function $f_i(x)$ should be continuous between pixels x_1 and x_n

(c) The second derivative of function $f_i(x)$ should be continuous between pixels x_1 and x_n.

In order to solve the coefficients presented in Equations (5.8) through (5.11), one additional equation is derived from the requirement that the second derivative of function $f_i(x)$ should be continuous:

$$M_i - 4 * M_{i+1} + M_{i+2} = 6\big(I(i,j) - 2(i+1,j) + I(i+2,j)\big) \qquad (5.12)$$

Equations (5.8) through (5.12) lead to the formulation of a system of N-2 linear equations with N unknowns, where N is the number of pixels in a row. In order to solve the system of linear equations presented in Fig. 5.3, two more edge constraints must be introduced. In natural splines, the edge constraints are set such that $M_1 = M_n = 0$. Once the system of equations is solved, the

values of a_i, b_i, c_i, and d_i are uniquely determined. Finally, the interpolated value $f_i(x)$ is computed using Equation (5.7).

Due to the edge constraints that $M_1 = M_N = 0$, the system of n-2 linear equations need to be solved, which can result in an $(n-2)^2$ computational workload. However, because the constant matrix here is in tridiagonal form, the Crout or Doolittle algorithm can be applied to solve the matrix [95]. This algorithm decreases the computational workload to 5*n-14 multiplications and divisions and 3*n-9 additions and subtractions. This reduction in computational cycles can lead to real-time execution of the interpolation algorithm.

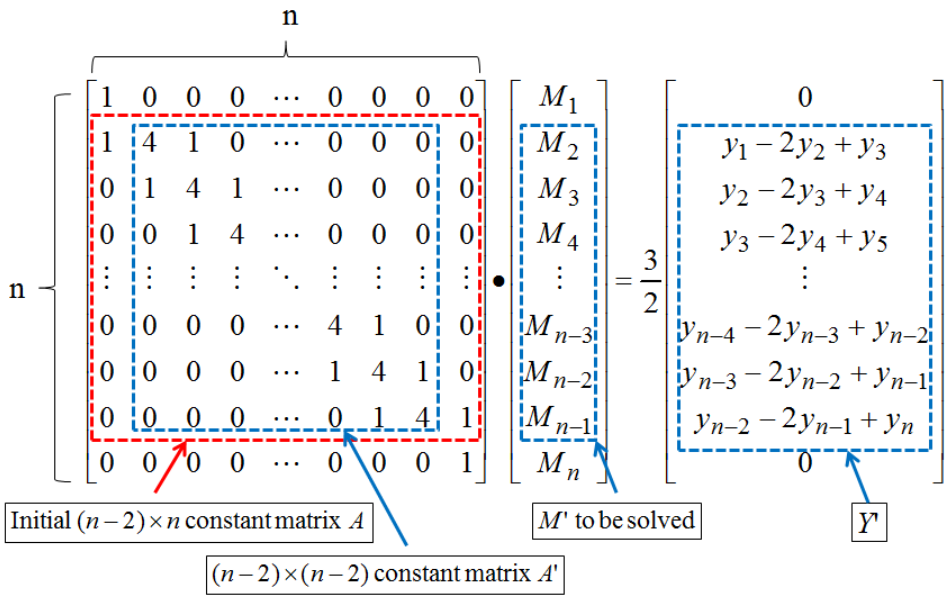

$$A \bullet M = Y \xrightarrow{M_0 = M_n = 0} A' \bullet M' = Y' \tag{5.13}$$

Figure 5.3. A system of n linear equations is constructed for solving the values of Mi. The value of the newly interpolated curve is computed using Equation (5.7).

The drawbacks of the above implementation are the need to store the entire frame information in memory and the computational complexity necessary to estimate new pixel values. This limitation might limit real-time execution of the algorithm. Thus, we developed an approximated

bicubic spline algorithm that is more suitable for computational systems with limited memory, such as FPGAs and DSPs [96]. This algorithm computes the bicubic spline interpolation on a sub-window of 10x10 pixels from the imaging array. The edge constraints of the computational window remain the same as described above: $M_0 = M_{10} = 0$. This algorithm can also be executed in parallel on multiple independent windows in the imaging array, and it can enable real-time execution of the algorithm.

5.3.3 Bicubic Convolution Interpolation Algorithm

The commonly used bicubic interpolation algorithm attempts to fit a surface between four corner points of the low-resolution image using a third-order polynomial function. In order to compute the intensity value of the target pixel via the bicubic interpolation algorithm, the spatial derivatives in the horizontal, vertical, and diagonal directions at the four corner points are initially computed. A total of twelve spatial derivatives are computed and combined with intensity values from the four corner points in order to compute the interpolated pixel value. Hence, the bicubic interpolation algorithm is very computational intensive and difficult to realize in real time with high-resolution images.

The bicubic convolution algorithm is an approximation of the bicubic interpolation algorithm that is more computationally efficient, but at the cost of lower reconstruction accuracy [88]. The bicubic convolution process is computed first in the x-direction, followed by convolution in the y-direction. The raw image, as recorded by the DoFP sensor, is composed of four sub-images sampled with four respective linear polarization filters. Each one of the four sub-images has a quarter of the total resolution of the DoFP imaging array. For example, if the DoFP sensor is composed of 1000x1000 pixels, the sub-image corresponding to the pixels covered with 0° linear polarization filters contains 500x500 pixels. The sub-images corresponding to the pixels covered

with 45°, 90°, and 135° also contain 500x500 pixels each. These four sub-images are referred to as low-resolution images, and the aim of the interpolation algorithms is to recover the full 1000x1000-pixel resolution, with the highest accuracy, for all four sub-images.

The interpolated pixel, I(x,y), located between the low-resolution pixels, f(x,y) and f(x+1,y), is computed via the convolution process described by Equation (5.14):

$$I(x,y) = \sum_{s=-1}^{2} W(s) \bullet f(x+s,y) \quad \text{for } x = [1, N-1] \text{ and } y = [1, M] \tag{5.14}$$

where the bicubic convolution kernel, W(s), can be described via Equation (5.15):

$$W(s) = \begin{cases} 3/2 \bullet |s|^3 - 5/2 \bullet |s|^2 + 1 & 0 < |s| \le 1 \\ -1/2 \bullet |s|^3 + 5/2 \bullet |s|^2 - 4 \bullet |s| + 2 & 1 < |s| \le 2 \\ 0 & 2 < |s| \end{cases} \tag{5.15}$$

In Equations (5.14) and (5.15), N is the number of pixels in the x-direction, M is the number of pixels in the y-direction, and s is the relative location of a pixel in the convolution kernel. Expanding Equation (5.14) into a matrix form, the bicubic convolution interpolation is computed via Equation (5.16):

$$I(x,y) = \begin{bmatrix} 1/2 \\ 1/4 \\ 1/8 \\ 1/16 \end{bmatrix}' \bullet \begin{bmatrix} 0 & 2 & 0 & 0 \\ -1 & 0 & 1 & 0 \\ 2 & -5 & 4 & -1 \\ -1 & 3 & -3 & 1 \end{bmatrix} \bullet \begin{bmatrix} f(x-1,y) \\ f(x,y) \\ f(x+1,y) \\ f(x+2,y) \end{bmatrix} \quad \begin{matrix} x = 1 \cdots \\ y = 1 \cdots \end{matrix} \tag{5.16}$$

Special boundary conditions are applied to the first and last pixel of each row in the image. The conditions are described by Equation (5.17).

$$\begin{cases} f(0,y) = 3f(1,y) - 3f(2,y) + f(3,y) \\ f(N+1,y) = 3f(N,y) - 3f(N-1,y) + f(N-2,y) \end{cases} \quad (5.17)$$

Once the image is convolved in the x-direction, the same convolution algorithm is repeated in the y-direction of the image to complete the interpolation process.

5.3.4 Gradient-Based Interpolation Algorithm

We propose a gradient-based interpolation algorithm in order to improve the quality of polarization information captured by a DoFP polarization imaging sensor. The fundamental idea behind the gradient-based algorithm is that if an edge is encountered in the scene, then interpolation is performed along the edge and not across the edge [97][84][98]. In the proposed implementation, bicubic convolution interpolation is performed along an edge in the image. Bilinear interpolation algorithm is implemented in the smooth areas of the image, that is, in the areas where no edges have been detected. In terms of low spatial frequency features, both bilinear and bicubic interpolation results have a similar error reconstruction and modulation transfer function (MTF) response [86]. In terms of medium and high spatial frequency features, bicubic interpolation outperforms bilinear interpolation in root mean square error (RMSE) and MTF. Because executing bilinear interpolation is less computationally complex than bicubic convolution, and due to the similar level of accuracy in the reconstructed images of the two algorithms, bilinear interpolation is used on the smooth features of the image.

In order to implement this algorithm, the boundary discontinuities (or edges) in an image need to be computed first. An edge in an image is defined as a place where the spatial gradient exceeds a given threshold, and it typically identifies an area in the image where one object ends and another one starts. For example, in color images, a high gradient exists between two objects of different colors or intensities. In polarization images, a high gradient exists between objects of

different intensities, angles of polarization, or degrees of linear polarization. These gradients imply that edges also exist in the four composite images (i.e., in the 0°, 45°, 90°, and 135° images.

In the gradient-based interpolation algorithm, the bicubic convolution and the bilinear interpolation algorithms are expanded to incorporate gradient selectivity features. To this extent, the gradients across the vertical, horizontal, and two diagonal directions in a 7x7, low-resolution pixel neighborhood on all four images (0°, 45°, 90°, and 135°) are computed using Equation (5.18):

$$\begin{cases} D_{0^o} = \sum_{i=2,4,6} \sum_{j=3,5,7} \left| I(i,j) - I(i,j-2) \right| \\ D_{45^o} = \sum_{i=1,3,5} \sum_{j=3,5,7} \left| I(i,j) - I(i+2,j-2) \right| \\ D_{90^o} = \sum_{i=3,5,7} \sum_{j=2,4,6} \left| I(i,j) - I(i-2,j) \right| \\ D_{135^o} = \sum_{i=1,3,5} \sum_{j=1,3,5} \left| I(i,j) - I(i+2,j+2) \right| \end{cases} \qquad (5.18)$$

In the above equations, D0° is the gradient in the horizontal direction, D90° is the gradient in the vertical direction, and so on. Fig. 5.4 illustrates how the gradient in the 135° diagonal and horizontal directions are computed. The black pixel in Fig. 5.4 denotes the target pixel of the interpolation computation.

An optimal gradient detection filter should satisfy the following three goals: accurate detection selectivity of the edges, accurate localization of the edges, and minimum response to false edges [99]. Following the above criteria, a small convolution kernel (e.g., a 2x 2-pixel window) will be very sensitive to image noise and result in many false-negative edges, while a large convolution kernel will smooth out the image, thus suppressing many edges that should be detected. We have

selected an intermediate size for the convolution kernel (e.g., a 7x7-pixel window), which provides a balance between suppressing many false edges due to noise and keeping image fidelity in order to detect the desirable edges of objects.

Depending on the relative positions between known and unknown pixels, the interpolation is implemented first on pixels with known values in the diagonal directions, followed by interpolation on pixels with known values in the horizontal or vertical direction, as described in the following steps:

1) If the ratio of the gradient in the 45° direction over the gradient in the 135° direction exceeds a threshold (i.e., $D_{45^o}/ D_{135^o} > T_{threshold}$), which indicates an edge along the 135° diagonal direction, the bicubic convolution algorithm is applied to the target pixel along the 135° diagonal direction. Similarly, if the ratio of the gradient in the 135° direction over the gradient in the 45° direction exceeds a threshold (i.e., $D_{135^o} / D_{45^o} > T_{threshold}$), the bicubic convolution algorithm is applied to the target pixel along the 45° diagonal direction. In all other cases, the intensity value of the target pixel is the average of the intensity values of its four adjacent pixels in the diagonal directions.

2) If the ratio of the gradient in the 0° direction over the gradient in the 90° direction exceeds a threshold (i.e., $D_{0^o}/D_{90^o} > T_{threshold}$), which indicates an edge along the vertical direction, the bicubic convolution is applied to the target pixel along the vertical direction. If the ratio of the gradient in the 90° direction over the gradient in the 0° direction exceeds a threshold (i.e., $D_{90^o}/D_{0^o} > T_{threshold}$), bicubic convolution is applied to the target pixel along the horizontal direction. In all other cases, the intensity value of the target pixel is the average of its four adjacent pixels in horizontal and vertical directions.

The $T_{threshold}$ value is decided using histogram distribution of the derivative ratios in a diagonal direction ($D_{45°}$/ $D_{135°}$) across the imaging scenes for all four angles (0°, 45°, 90°, and 135°). From our experimental results, we have determined that setting the $T_{threshold}$ value at 55%–65% of the gradient's ratio cumulated distribution function (CDF) yields the best reconstruction results, as explained in the results section (see subsection 4.3).

Figure 5.4. (a) 135° direction gradient example. (b) 0° direction gradient example. Note: the blue pixels are of known value, the black pixel is the target pixel, the gray pixels are the same type as the target pixel, and the white pixels are of unknown value.

The computational complexity of an interpolation algorithm is an important consideration for real-time implementation. The proposed gradient-based interpolation is computationally more intensive compared to bilinear and bicubic convolution algorithms. For example, the edge convolution filter requires two multiplications, 34 additions, and one thresholding operation per pixel; the bicubic convolution algorithm requires 24 multiplications and 23 additions; and the bilinear interpolation requires four multiplications and three additions. The overall computational complexity of the gradient-based algorithm depends on the spatial features of the imaged scene, while bilinear and bicubic interpolations have a determined number of computational steps.

5.4 Modulation Transfer Function Evaluation

Modulation transfer function (MTF) is commonly used for evaluating the optical characteristics and performance of an imaging system. It measures the contrast of sinusoids as a function of spatial frequency [100]. In order to evaluate the MTF of an imaging system, a spatially varying sinusoidal pattern at various frequencies is used as a target image. The output from the imaging system is recorded and the contrast for a given input frequency is computed (i.e., the difference between the maximum and the minimum of the output sinusoid). The MTF is computed as the ratio of the contrast of the output sinusoidal pattern over the contrast of the input sinusoidal pattern for various frequencies.

In order to evaluate the MTF response for typical complementary metal oxide semiconductor (CMOS) or CCD grayscale or color imaging sensors, a single target composed of spatially varying intensity patterns is imaged, using a set of calibrated sinusoidal targets provided by Kodak [36]. The MTF of an imaging sensor depends on the MTFs of individual optical elements used in the system, such as lenses, filters, and pixel design.

DoFP polarization imaging sensors record both the intensity and polarization information of the light wave in every frame. Therefore, the standard procedure for evaluating the MTF of a CMOS/CCD imaging sensor should be modified accordingly, in order to encompass changes in the polarization properties of an input target. Because polarization sensors record photo response at four different pixels with linear polarization filters offset by 45°, an input target can be defined in such a way that any of the four pixel photo responses varies spatially at a particular spatial frequency. For example, an input target image can be defined as spatially varying sinusoids where the responses of the four pixels are defined as follows:

$$I_0(x,y) = \cos(2\pi f_x x + 2\pi f_y y) + 1 \quad (5.19)$$

$$I_{45}(x,y) = 2 * \cos(2\pi f_x x + 2\pi f_y y) + 2 \quad (5.20)$$

$$I_{90}(x,y) = \cos(2\pi f_x x + 2\pi f_y y) + 1 \quad (5.21)$$

$$I_{135}(x,y) = 0 \quad (5.22)$$

In Equations (5.19) through (5.22), f_x and f_y are the spatial frequency elements in the horizontal and vertical directions, respectively, in cycles per pixel. The spatial patterns for I_0, I_{45}, and I_{90} are modulated in both the x and y directions, resulting in a target image with variable intensity (i.e., variable S0 parameter, constant S_1 parameter, and variable S_2 parameter). Hence, the target image is composed of spatially varying intensity, angle, and degree of polarization patterns. The spatial patterns for I_0, I_{45}, I_{90}, and I_{135} are projected across the entire imaging array of a DoFP polarimeter. Due to the pixelated polarization pattern at the focal plane, all four spatial patterns described by Equations (5.19) through (5.22) are decimated in order to emulate an image recorded by a DoFP imaging sensor. Using the decimated images as inputs to the different interpolation algorithms described in subsection 5.2, four high-resolution images are generated.

The original and interpolated images are used to compute the MTF of the system. First, the first Stokes parameter, S_0, is computed from the data recorded by the four pixels. The Fourier transform is computed on the intensity images from the original and interpolated datasets. Because the target image is a cosine function with horizontal and vertical frequencies (f_x,f_y), the Fourier image has two main frequency peaks, at positions (f_x,f_y) and (-f_x,-f_y). Because the accuracy of the interpolated images is a strong function of the input frequency of the target image, the amplitude of the main frequency peaks of the S_0 image will be a function of the input frequency as well. The MTF of the imaging sensor is computed as the ratio of the magnitude of

the main frequency peak in the interpolated result, $M_{interpolated}(f_x,f_y)$, over the magnitude of the main frequency peak in the original image, $M_{original}(f_x,f_y)$.

Figure 5.5 presents the MTF of an intensity image from four different interpolation algorithms. In Fig. 5.5(a)–(d), the vertical and horizontal frequencies, f_x and f_y, are swept from 0 to 0.5 cycles per pixel, and the MTF response is computed at each frequency. Figure 5.5(e) presents the MTF response for all four interpolation algorithms across equal horizontal and vertical frequencies (i.e., $f_x = f_y$). In Fig. 5.5(e), the ideal MTF response of a full-resolution sensor is plotted for comparison reasons. Due to the Nyquest sampling theorem, the ideal MTF has a response of 1.0–0.5 cycles per pixel, and it drops to 0 for higher frequencies. Because DoFP polarimeters sample scenes with four different polarization filters, the MTF of this class of sensors drops to 0 at frequencies higher than 0.25 cycles per pixel.

Two important observations can be made regarding bilinear and weighted bilinear interpolation [85]. Specifically, MTF function decreases relatively quickly at low spatial frequencies and goes to 0 at $f_x=f_y=0.25$ cycles per pixel. Bilinear interpolation does not perform well when the interpolated signal contains high spatial frequencies. According to Nyquest's theory, the signal cannot be reconstructed beyond a spatial frequency of 0.25 cycles per pixel. Meanwhile, the two bicubic interpolation algorithms reconstruct high spatial frequency information more effectively when compared to bilinear algorithms [86]. The bicubic spline interpolation algorithm is the best at preserving low-frequency features, while the bicubic algorithm can recover the highest frequency components better than any other algorithm (up to a spatial frequency of 0.375 cycles per pixel).

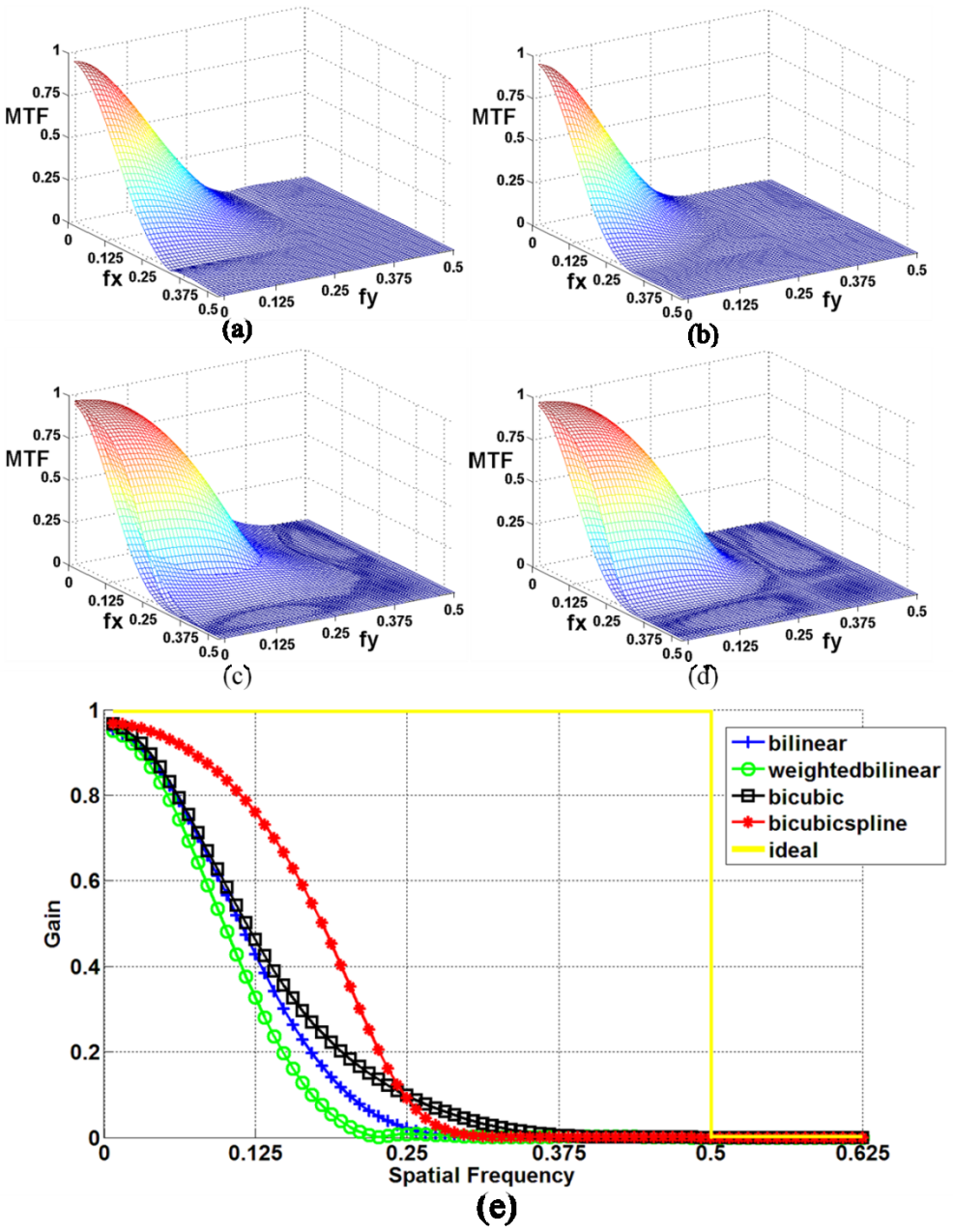

Figure 5.5. The MTF of S_0 for (a) bilinear, (b) weighted bilinear, (c) bicubic, and (d) bicubic spline interpolation algorithms. (e) The MTF results of S_0 along $f_x = f_y$.

5.5 Performance Evaluation of Interpolation Algorithms for Multispectral Imaging

In order to evaluate the reconstruction accuracy of different interpolation algorithms, the true high-resolution spectral image must be known a priori. Because our proposed bio-inspired spectral imaging sensor only has low-resolution imaging output, the performances of different

interpolation algorithms cannot be compared against the true spectral signatures, as they are not known a priori. To solve this problem, we developed an evaluation scheme based on a division-of-time multispectral camera solution (Fig. 5.6), using the same grayscale CCD imaging sensor (Kodak KAI-2020, 60dB dynamic range) and four different spectral filters (color filters: Thorlabs FD1D; near infrared (NIR) filter: Semrock BLP01-785R) placed on a filter wheel (Thorlabs FW1A) in front of the imaging sensor. The spectral filters in the visible channel are red (R), green (G), and blue (B. By rotating the filter wheel, four co-registered, high-resolution images are obtained with this setup. These four images are regarded as the "true" high-resolution images, as they sample the optical field at every pixel with four different spectral wavelengths.

As shown in Fig. 5.6, the four "true" high-resolution images are then decimated by following the sampling pattern of the multispectral imaging sensor pattern shown in Fig. 5.1(b). Hence, four low-resolution images, at the R, G, B, and NIR channels, are obtained, and they essentially simulate an image that would be acquired by the proposed multispectral imaging sensor. The four low-resolution images are interpolated via different algorithms, and high-resolution images are computed. Finally, the final high-resolution interpolated images are compared against the true high-resolution images that were originally recorded. This experimental setup aims to provide a fair comparison of reconstruction errors between bilinear, bicubic spline, and bicubic convolution and gradient-based interpolation algorithms.

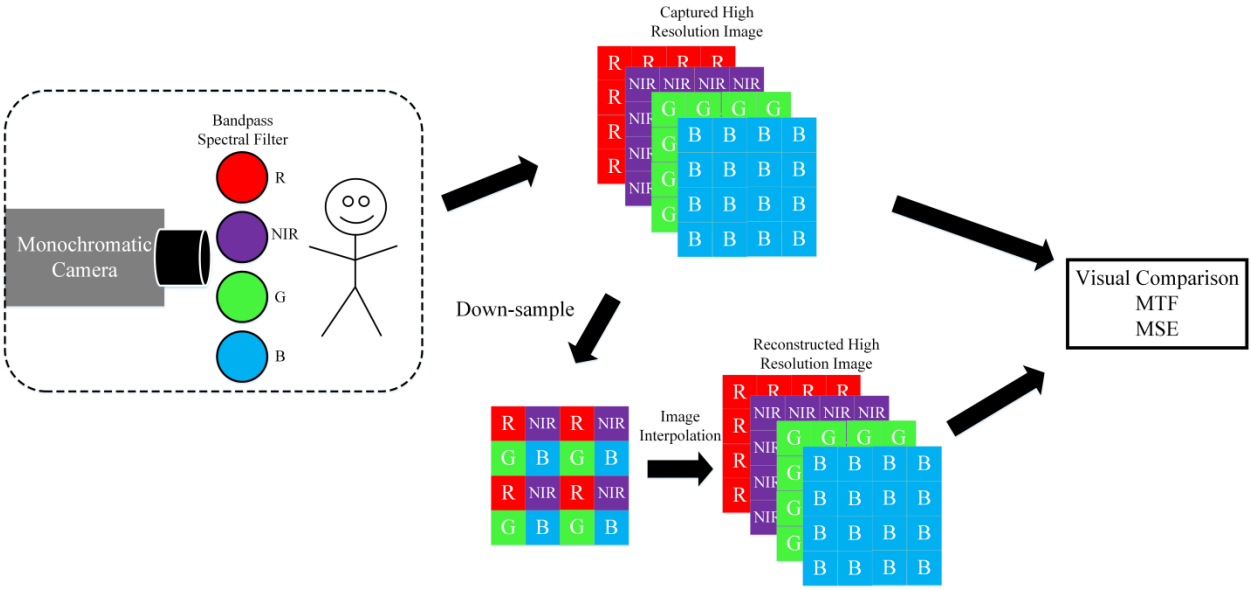

Figure 5.6. Evaluation scheme of multispectral imaging for different interpolation algorithms.

5.5.1 Image Visual Comparison

In Fig. 5.7, small regions in images of toys, depicted by white squares for visible channel and blue rectangles for NIR channel, were used for visual evaluation of the different interpolation algorithms. The regions are expanded in Fig. 5.8.

The set of images in Fig. 5.8 is organized as follows. Figure 5.8(a) shows the interpolated color images of region 1: from left to right, the images are the results of original true high resolution, bilinear, bicubic spline, bicubic convolution, and gradient-based interpolation algorithms. Figure 5.8(b) shows the interpolated color images of region 2, and Fig. 5.8(c) shows the interpolated NIR images of region 3.

The images obtained via bilinear interpolation show strong pixilation effects along the edge areas (marked as A, B, and C), and the backgrounds are accentuated and show strong "toothed artifacts," due to the large error introduced by the bilinear interpolation. The images obtained via bicubic spline and bicubic convolution interpolation algorithms show similar results. The details in the visible images and in the NIR image are recovered with higher accuracy than with bilinear

interpolation. Pixilation effects are visibly reduced with bicubic interpolation when compared to bilinear interpolation.

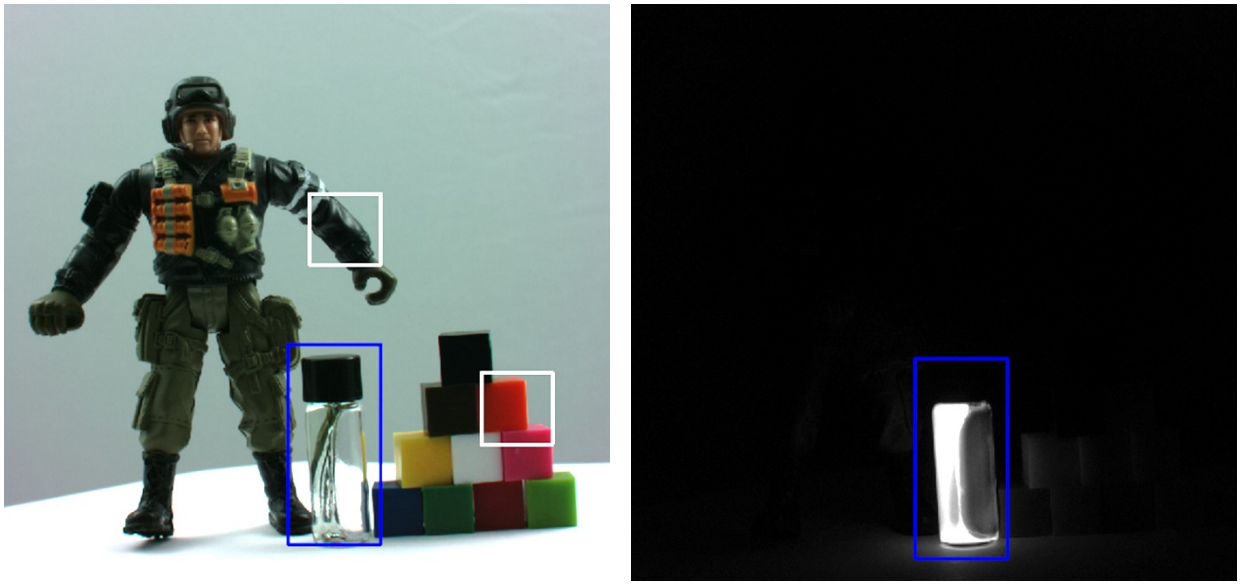

(a) (b)

Figure 5.7. The true, high-resolution image; (a) visible channel and (b) NIR channel.

The gradient-based interpolation images ($T_{threshold}$: 60% CDF) are presented in the last column. This set of images is well recovered, and they closely resemble the true, high-resolution visible and NIR images. There are no large pixilation artifacts observed in any image of the three regions. Therefore, the gradient-based interpolation algorithm visually recovers high-resolution images with the highest level of accuracy.

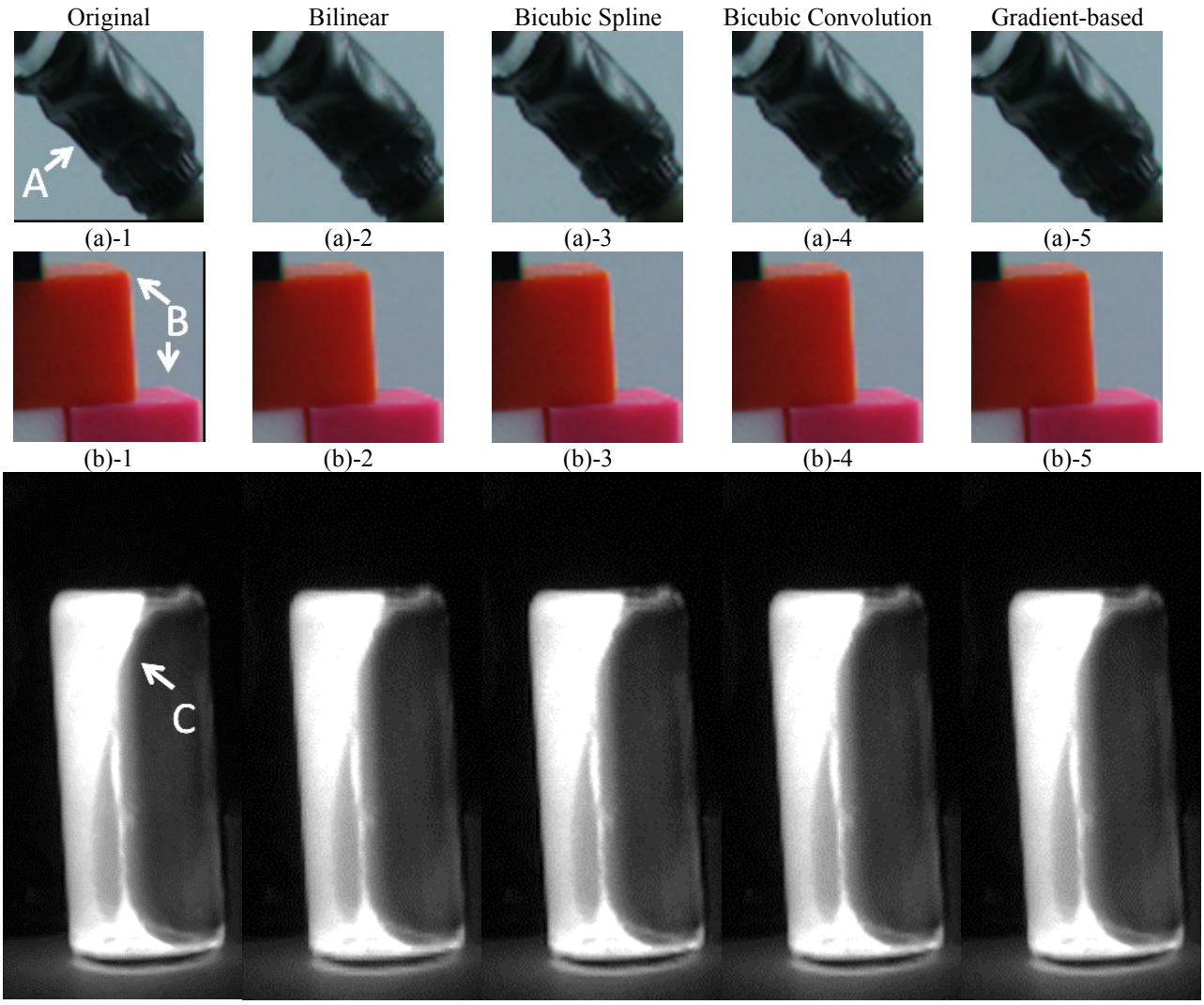

Figure 5.8. Comparison of different interpolation algorithms in visible and NIR channels: (a) region 1 visible channel result, (b) region 2 visible channel result, and (c) region 3 NIR channel result. In each row, the image order is: original, bilinear, bicubic spline, bicubic convolution, and our proposed gradient-based interpolation algorithms.

5.5.2 RMSE Comparison

In order to provide a numeric comparison of the accuracy of the different interpolation algorithms, the RMSE evaluating algorithm is applied in Equation (5.23):

$$RMSE = \sqrt{\frac{1}{MN} \sum_{1 \le i \le M} \sum_{1 \le j \le N} \left(O_c(i,j) - I_c(i,j) \right)^2} \qquad (5.23)$$

where $O_c(i, j)$ is the true value of the target pixel (i.e., the image presented in Fig.s 5.7 (a) and (b)), $I_c(i, j)$ is the interpolated intensity value of the target pixel, and M and N represent the number of rows and columns, respectively, in the image array.

Table 5.1. RMSE performance comparison for toy scene

	Bilinear	Bicubic Spline	Bicubic Convolution	**Gradient-based Interpolation**
Red	3.51E+01 (1.05)	3.48E+01 (1.04)	3.43E+01 (1.02)	**3.34E+01 (1)**
Green	3.66E+01 (1.04)	3.65E+01 (1.03)	3.59E+01 (1.01)	**3.53E+01 (1)**
Blue	3.42E+01 (1.05)	3.41E+01 (1.05)	3.35E+01 (1.03)	**3.27E+01 (1)**
NIR	8.58E+00 (1.09)	8.08E+00 (1.02)	8.00E+00 (1.01)	**7.89E+00 (1)**

Ratios of different interpolation algorithms to gradient algorithm are shown in parentheses

The RMSE results of the different interpolation algorithms of the test images are shown in Table 5.1. The minimum RMSEs of the different spectral channels are obtained via the gradient-based interpolation algorithm. Of all the comparisons, the bilinear interpolation algorithm introduces the greatest error, while the bicubic spline and bicubic convolution interpolation algorithms show similar error performances, with the latter being computationally efficient.

5.6 Performance Evaluation of Interpolation Algorithms for Polarization Imaging

In order to evaluate the accuracy of different interpolation algorithms, the true, high-resolution polarization image must be known a priori. DoFP polarization imaging sensors can only generate low-resolution images. Thus, the performances of the interpolation algorithms cannot be compared against the true polarization signature, as it is not known a priori. In order to circumvent this problem, a set of images are acquired using a grayscale CCD imaging sensor (Kodak KAI-4022, 40dB SNR, 60dB dynamic range) with a linear-polarized filter rotation stage (Thorlabs NR360s, 5 arcmin accuracy) placed in front of the sensor. The linear-polarized filter is rotated at 0°, 45°, 90°, and 135°, thus obtaining four co-registered, high-resolution images. These

four images are regarded as the “true” high-resolution images, as they sample the optical field at every pixel with four different linear polarization filters offset by 45°.

Next, the four “true” high-resolution images are decimated by following the sampling pattern of the DoFP polarization imaging sensor shown in Fig. 5.1(a). Hence, four low-resolution images are obtained at featured angles of 0°, 45°, 90°, and 135°, and they essentially simulate an image that would be acquired with a DoFP sensor. The four low-resolution images are interpolated using different algorithms, and high-resolution images are computed. The final high-resolution interpolated images are compared against the true high-resolution images that were originally recorded. This experimental setup aims to provide a fair comparison of the reconstruction errors among the bilinear, bicubic, and gradient-based interpolation algorithms.

The four high-resolution images are recorded with a grayscale camera with a rotating linear polarization filter, and they might contain alignment errors in the optical setup. The optical misalignment in the image acquisition setup generates errors in the acquired polarization data. These errors are not critical for our set of experiments, as the interpolation algorithms are implemented on the decimated images computed from the original high-resolution images. The interpolated images are compared against the original high-resolution images in order to estimate the accuracy of the algorithm. Thus, any optical misalignment errors would affect the original high-resolution images and the interpolated images equally.

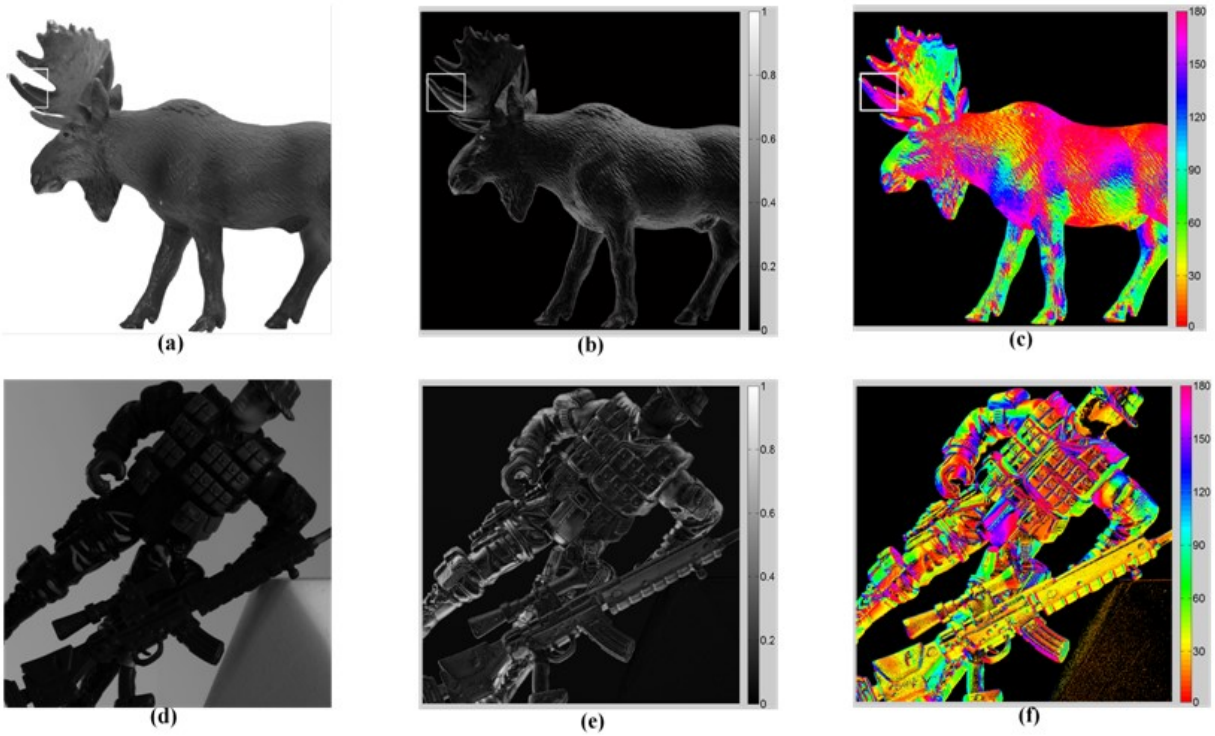

Figure 5.9. True high-resolution images: (a) moose–intensity, (b) moose–DoLP, (c) moose–AoP, (d) soldier–intensity, (e) soldier–DoLP, (f) soldier–AoP.

In Figures 5.9(a)–(c), the intensity, DoLP, and AoP results of a toy moose are presented (integration time: 100 msec). This figure, which presents the "true" high-resolution images, is used to compare the accuracy of the interpolated images. The polarization sub-properties, DoLP and AoP, are mapped to grayscale and false color scales, respectively (Figures 5.9(b) and (c)). A second example, using a toy soldier (Figures 5.9(d)–(f)), is used to verify the validation of the adaptive threshold selection (Sec. 5.6.3.1).

5.6.1 Visual image comparison

A small region in the images of the moose (Figures 5.9(a)–(c)), depicted by a white square, is used for visual evaluation of the different interpolation algorithms. The region in the white box is expanded and presented in Fig. 5.10.

The set of images in Fig. 5.10 is organized as follows: the first column presents the intensity images; the second column presents the DoLP images, and the third column presents the AoP images. The first row of images (Fig. 5.10(a)) presents the true, high-resolution polarization images, which are used to compare visually the reconstruction accuracy of the different interpolation algorithms presented in the following four rows.

The images in Fig. 5.10(b) are obtained via bilinear interpolation and show strong pixilation effects in the intensity, DoLP, and AoP images. In all three images, the details of the moose's antlers are pixelated; the edges (marked A, B, and C) and the background are accentuated and show strong "toothed artifacts," due to the large error introduced by the bilinear interpolation.

The images presented in Fig.s 5.10(c) and (d) are obtained via the bicubic spline and bicubic convolution interpolation algorithms, respectively. The two bicubic-based interpolation algorithms show similar results. In these sets of images, the details of the moose's antlers in both DoLP and AoP are recovered with higher accuracy than with bilinear interpolation. Pixelation effects are visibly reduced with bicubic interpolation compared to the bilinear technique. However, the DoLP and AoP images both present a visible "ripple effect," especially in the edge area (marked A, B, and C) between the moose's antlers and the background.

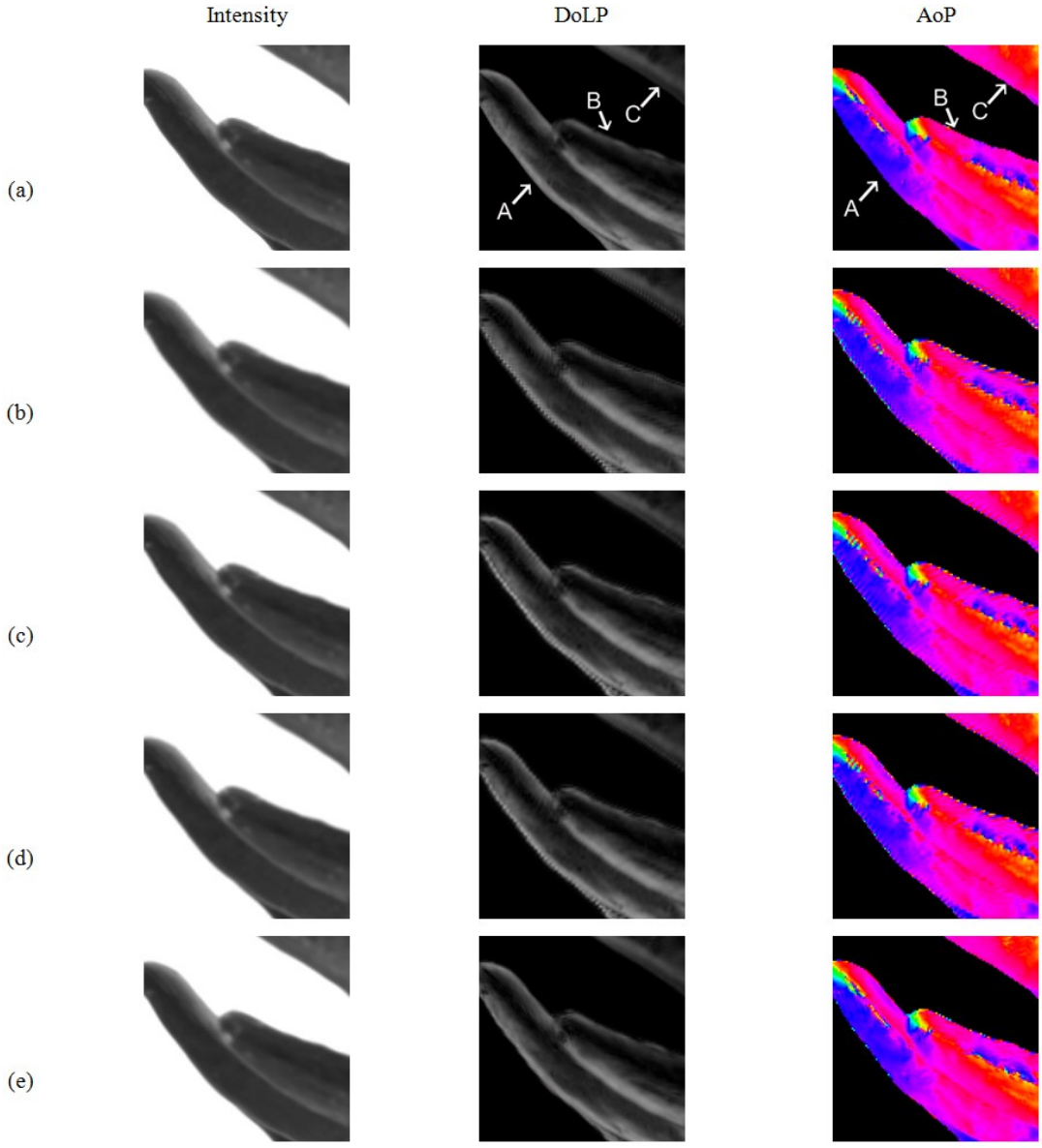

Figure 5.10. Comparison of different interpolation algorithms on intensity, DoLP, and AoP: (a) true polarization, (b) bilinear interpolation, (c) bicubic spline interpolation, (d) bicubic convolution, and (e) gradient-based interpolation.

The images presented in Fig. 5.10(e) are the results of gradient-based interpolation ($T_{threshold}$: 60% CDF). This set of images is well recovered, and it closely resembles the true polarization images. There are no large pixelation artifacts observed in any of the three polarization images. Hence, the gradient-based interpolation algorithm visually recovers a high-resolution image with the highest accuracy.

5.6.2 RMSE Comparison

The RMSE comparison is performed using Equation (5.23). The RMSE results of the different interpolation algorithms of the toy moose images are shown in Table 5.2. The minimum RMSE for I(0°), I(45°), I(90°), I(135°), intensity, DoLP, and AoP images is obtained using the gradient-based interpolation algorithm. The bilinear interpolation algorithm introduces the largest error of all the comparisons, while the bicubic spline and bicubic convolution interpolation algorithms exhibit a similar error performance, with the latter being computationally efficient.

Table 5.2. RMSE performance comparison of toy moose images

	Bilinear	Bicubic Spline	Bicubic Convolution	**Gradient-based Interpolation**
Intensity	2.40E+01 (1.48)	1.80E+01 (1.11)	1.90E+01 (1.17)	**1.62E+01 (1)**
DoLP	2.00E-02 (1.23)	1.94E-02 (1.19)	1.83E-02 (1.12)	**1.63E-02 (1)**
AoP	6.79E+00 (1.08)	6.59E+00 (1.04)	6.42E+00 (1.02)	**6.31E+00 (1)**
I(0°)	2.04E+01 (1.42)	1.69E+01 (1.17)	1.73E+01 (1.20)	**1.44E+01 (1)**
I(45°)	1.97E+01 (1.41)	1.66E+01 (1.19)	1.69E+01 (1.21)	**1.40E+01 (1)**
I(90°)	1.94E+01 (1.37)	1.66E+01 (1.17)	1.69E+01 (1.19)	**1.42E+01 (1)**
I(135°)	1.92E+01 (1.40)	1.61E+01 (1.18)	1.64E+01 (1.20)	**1.37E+01 (1)**

5.6.3 Discussion of Interpolation Algorithms for Polarization Imaging Sensor

5.6.3.1 Adaptive Threshold Selection

Accurate threshold selection for discerning edges in an image is a key part of most edge-detection algorithms. In order to determine an edge in an image, most algorithms use an experimentally determined edge threshold and assign it as a constant for a set of images. Although this algorithm is computationally efficient, it does not yield good edge detection results, as edge thresholds tend to vary between images.

In the proposed gradient-based interpolation algorithm, the threshold is determined using the CDF of the ratio between two orthogonal spatial derivatives (D_{0^o}/D_{90^o} or D_{45^o}/D_{135^o}) for the intensity image of each angle separately. One single threshold value is assigned to each intensity image by assuming that the spatial derivatives in different directions have the same histogram distribution. The edge thresholds are determined using the CDF by selecting different percentiles of the function. For example, selecting a threshold value of 100% of the CDF effectively suppresses edge detection and yields the same RMSE as a bilinear algorithm. If the threshold value is set to 30% of the CDF or lower, many false positive edges could be selected, leading to an RMSE similar to that of bicubic convolution. If the edge threshold is set to 0% of the CDF, all areas in the image are defined as edges, and bicubic convolution interpolation is applied across the entire image.

In order to determine a well-suited threshold value, the RMSEs of the DoLP and AoP images are computed for different threshold values. Because both display similar trends, in the interest of brevity, only the AoP results are shown in Fig. 5.11.

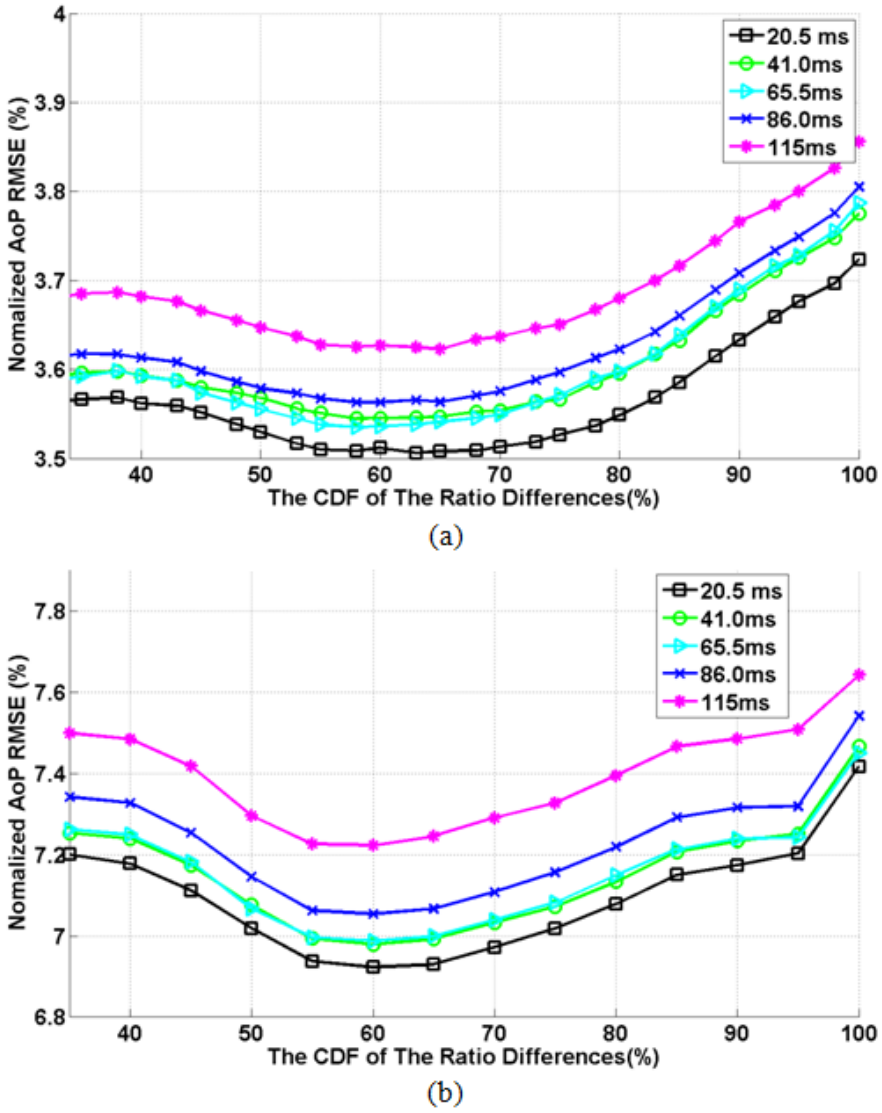

Figure 5.11. Different CDF threshold selections: (a) normalized AoP RMSE of the toy moose and (b) normalized AoP RMSE of the toy soldier .

The normalized AoP RMSE (the ratio of the RMSE to the maximum value) of the moose image was evaluated for five different integration times of the imaging sensor in order to emulate different dynamic ranges in a scene; the results are presented in Fig. 5.11(a). For example, low integration times allow few photons to be registered by the array of photodiodes, and the dynamic range of the scene is very low. Conversely, longer integration times allow for a higher number of photons to be collected by the array of photodiodes, and hence, the dynamic range of

the scene is higher (see Fig. 5.10). The normalized RMSE of the AoP image of the toy soldier as a function of the edge threshold is shown in Fig. 5.11(b). The RMSE error for both sets of images follows a similar trend with respect to edge threshold value.

For all five different integration times, the minimum RMSE is obtained when the threshold value is set between 55% and 65% of the CDF. Therefore, the threshold for computing edges in a scene is set to 60% of the CDF. This rule of thumb was used in several different sample images we collected, and consistent minimum RMSE results were obtained for each image. Therefore, setting the edge detection threshold between 55% and 65% of the CDF is a good guideline for any image.

5.6.3.2 Dynamic Range Impact on Interpolation

DoFP polarization sensors are used to image scenes with various dynamic ranges, ranging from very dim scenes to very bright ones. As such, the accuracy of the interpolated polarization information, as a function of a scene's dynamic range, needs to be evaluated closely. In this section, a toy moose scene, presented in Figures 5.9(a)–(c), is imaged under different integration times. The integration time of the imaging sensor is swept between 0.5 msec and 120 msec. Note that similar results are obtained when the aperture of the sensor is modulated or the illumination of the scene is varied between experiments. In the interest of brevity, we only present data collected under different integration periods.

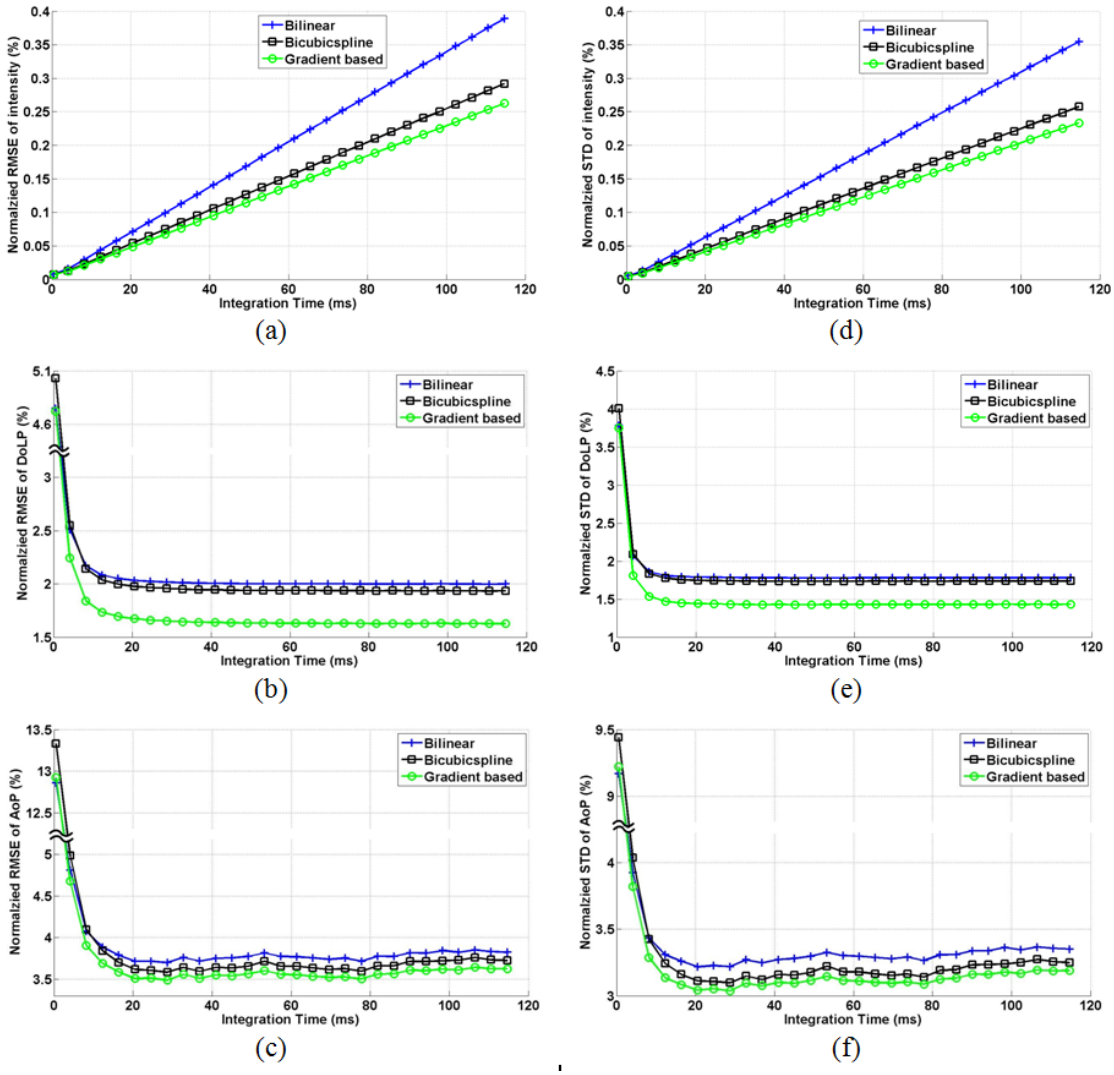

Figure 5.12. Normalized RMSE results: (a) intensity, (b) DoLP, and (c) AoP. Normalized standard deviation of RMSE (d) intensity, (e) DoLP, and (f) AoP for different interpolation algorithms by scanning integration time.

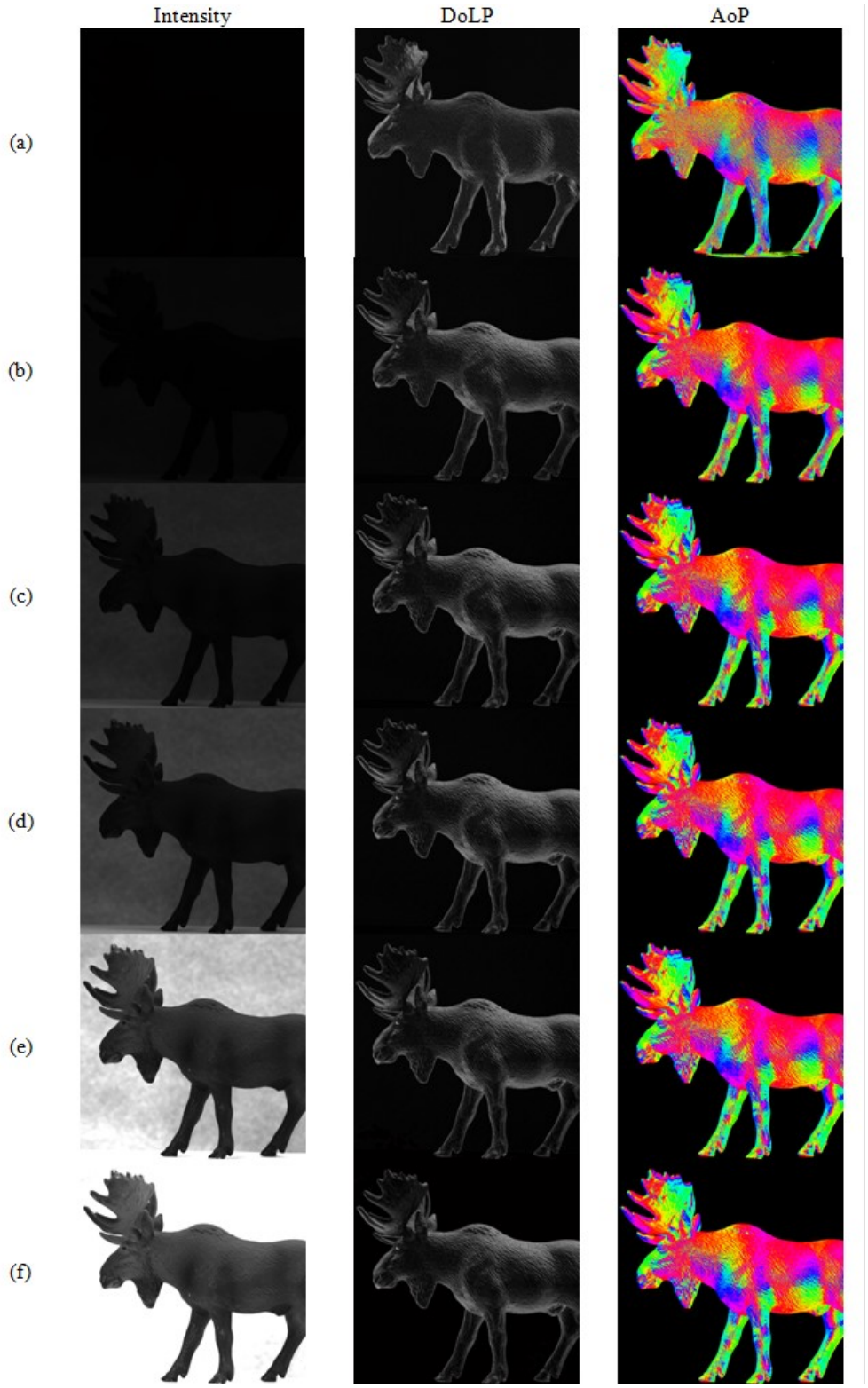

Figure 5.13. Image results of the sensor under different integration times: (a) 0.5 msec, (b) 4 msec, (c) 12 msec, (d) 20 msec, (e) 40 msec, and (f) 100 msec.

The normalized RMSE (the ratio of the RMSE to the maximum value) results for the intensity, DoLP, and AoP as a function of integration time are shown in Figures 5.12(a)–(c), respectively. Figures 5.12(d)–(f) present the corresponding normalized standard deviation (STD) of the RMSE for the intensity, DoLP, and AoP, respectively. The RMSE and STD figures are computed across all pixels in the imaging array. The STD plot follows a similar trend as the RMSE plots presented in Figures 5.12(a)–(c). The gradient-based interpolation algorithm yields the smallest variations in error measurements when compared to bilinear and bicubic interpolation across different integration times.

Sample images of intensity, DoLP, and AoP as a function of different integration times are presented in Fig. 5.13. The images were collected with a normal camera with a linear dynamic range of 60 dB; a high dynamic range camera was not used for collecting data. The images presented in Fig. 5.13(a) were collected with an integration time of 0.5 msec. In this set of images, the intensity image does not provide visible contrast to the object against the background, and the dynamic range of the scene, defined as the ratio of the difference between the maximum and minimum intensity pixels within the scene to the maximum allowed intensity of the pixel, is 0.5%. The dynamic range of the scene increases to 3% in the second row of images and continues to increase steadily in the rest of the images. The dynamic range of the scene for the intensity image in the last row is 70%. Based on the results shown in Fig. 5.12, the DoLP and AoP always provide good contrast and details of the target in a wide intensity range (any integration time larger than 4 msec), while having inaccurate information for a small dynamic range of the scene.

Figure 5.12(a) shows the intensity image error for different interpolation algorithms. The RMSE increases linearly with scene brightness (i.e., integration time of the imaging sensor). As the

integration time increases, the intensity values of the image increase as well. The interpolation algorithms attempt to compute a missing pixel value, and the error is greater for brighter scenes. The intensity values of dim scenes are low, and hence, the interpolation errors are naturally lower. The intensity values of bright scenes are high, and the interpolation errors are accordingly higher than the errors in the dim scenes. Another important observation that can be made is that the gradient-based interpolation algorithm has the lowest error compared to the other two interpolation algorithms.

Figures 5.12(b) and (c) present the normalized RMSE for the DoLP and AoP images as a function of the integration time. The errors in the AoP and DoLP are constant for the majority of the different integration times. This can be explained by observing Equation (5.2) and (5.3). Because the AoP and DoLP equations do not depend on the intensity measurements of the target, the errors introduced during the interpolation step in the image processing algorithm are constant for different integration times (i.e., for different dynamic ranges of the scene). In low-light conditions, the reconstruction errors increase because the signal-to-noise ratio (SNR) of the imaging sensor is low. Hence, the interpolated value has lower SNR or higher temporal variations. These temporal variations lead to higher inaccuracies in the reconstructed values of the raw pixel values. In Fig. 5.12, it can be observed that the proposed gradient-based interpolation algorithm outperforms the bilinear and bicubic interpolation algorithms under both short and long integration times of the imaging sensor.

Figures 5.12(d)–(f) present the corresponding normalized STDs of the RMSE for intensity, DoLP, and AoP. The RMSE and STD figures are computed across all pixels in the imaging array. The STD plot follows a similar trend as the RMSE plots presented in Figures 5.12(a)–(c). Furthermore, the gradient-based interpolation algorithm yields the smallest variations in error

measurements when compared to bilinear and bicubic interpolation across different integration times.

5.6.3.3 Interpolation Results of DoFP Polarization Imaging Sensor

The three interpolation algorithms (bilinear, bicubic spline, and gradient based) were applied to the image output of a high-resolution DoFP polarization imaging sensor [101] in order to evaluate their reconstruction performances. The DoFP sensor was inserted into an underwater casing, and real-life images of a lobster in its natural habitat were been recorded. The lobster images are presented in Fig. 5.14. Because the camera was submerged underwater, there is no specular reflection from the surface of the water in this imaging setup.

Figure 5.14 shows the interpolated results of a lobster body recorded underwater. Figure 5.14(a) shows the bilinear interpolation results. In this set of images, strong horizontal and vertical artifacts can be observed on the lobster's leg and tail in both the DoLP and AoP images. Figure 5.14(b) shows the bicubic interpolation results; many of the artifacts observed in the bilinear interpolation have been suppressed. Figure 5.14(c) shows the gradient-based interpolation results. In this set of images, many of the edge artifacts that caused strong polarization signatures in the bilinear and bicubic interpolation are suppressed by the gradient-based interpolation algorithm.

Examining the above results for each interpolation algorithm, the proposed gradient-based interpolation algorithm presents the best visual results and eliminates most of the noise and artifacts, which could be misinterpreted as "real" polarization information. It has been reported in the literature that there is no polarization information between the shell ridges of lobsters [102]. In addition, polarization information has not been observed between shell ridges when the lobster has been imaged with division of time imaging sensors. Division of time polarimeters

produce accurate polarization information at the edges of stationary objects. The polarization information at the edges of the shell ridges, when recorded with DoFP polarimeters, is incorrectly computed by the bilinear and bicubic interpolation algorithms and is suppressed by our gradient-based algorithm.

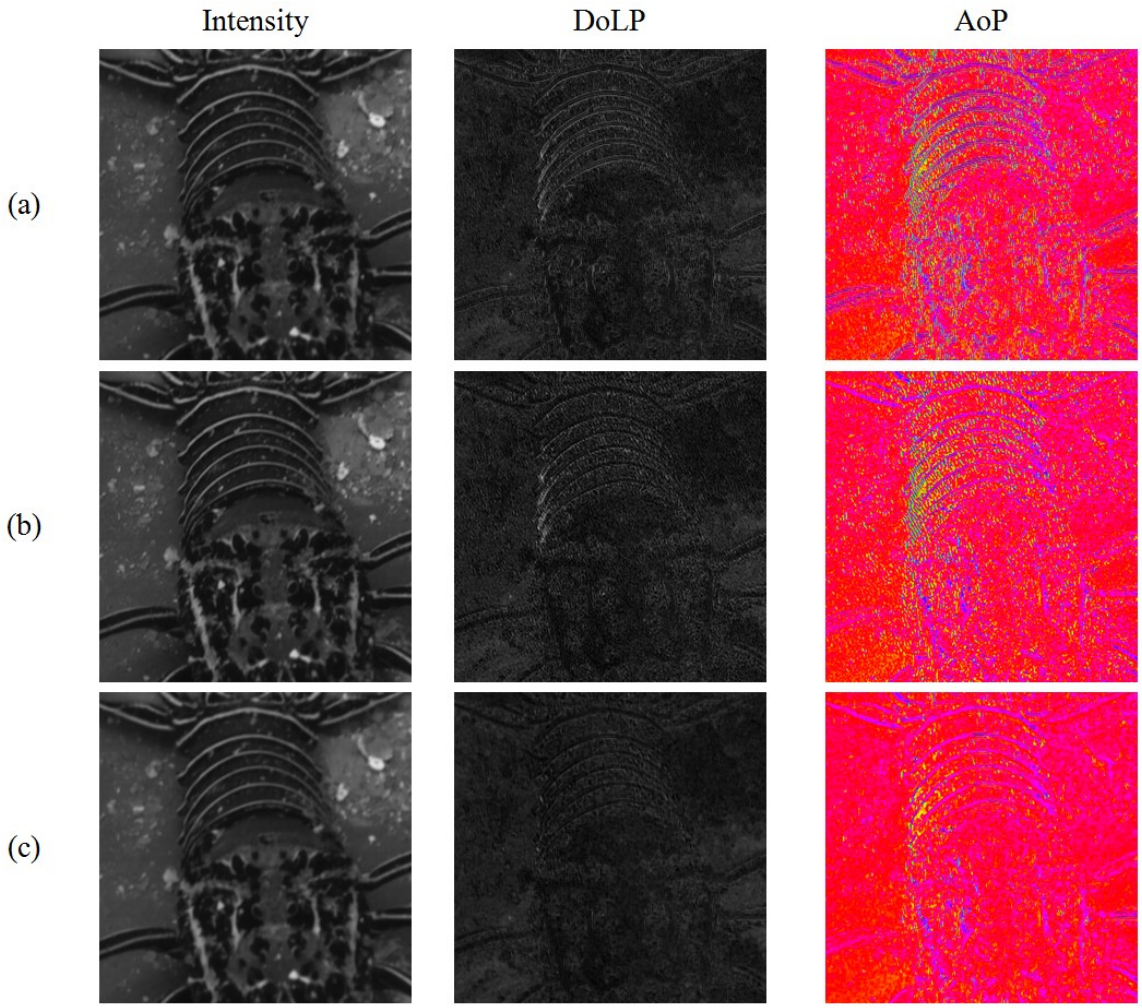

Figure 5.14. Interpolated results of DoFP imaging sensor on intensity, DoLP, and AoP: (a) bilinear interpolation, (b) bicubic spline interpolation, and (c) gradient-based interpolation.

5.7 Conclusion

In this chapter, we have presented several existing interpolation algorithms and a new, gradient-based interpolation algorithm for multispectral imaging sensors and DoFP polarization imaging

sensors. The performance of the proposed gradient-based interpolation algorithm is compared against the performance of three other interpolation algorithms in terms of visual testing and RMSE comparison. The theoretical frameworks of all four interpolation algorithms were also presented in this chapter. The interpolation algorithms were first analyzed using the MTF for their frequency performance, followed by numerical analysis on a set of images obtained via a CCD camera with different spectral filters, or a linear polarization filter rotated in front of the imaging sensor. The presented algorithm allows for the reconstruction of a true spectral or polarization image and constructs lower-resolution images by appropriately down-sampling the high-resolution images. The interpolation algorithms were implemented on the low-resolution images and compared numerically against the true high-resolution images. According to the results, the adaptive, gradient-based interpolation algorithm outperformed the bilinear and bicubic interpolation algorithms using both visual quantitative evaluation and qualitative evaluation via an RMSE method.

The improvements in reconstruction accuracy provided by the proposed gradient-based interpolation algorithm are achieved by applying bicubic convolution interpolation to the edge area and bilinear interpolation to the non-edge area. The original discontinuity within the edge area can be reconstructed well, while the smoothness within the non-edge area can also be maintained. The gradient-based interpolation algorithm outperformed bilinear and bicubic interpolation algorithms under various dynamic ranges of a scene, ranging from dim to bright conditions. It also improved greatly the output quality of the real multispectral imaging sensor and DoFP polarization imaging sensor.

Chapter 6: Conclusion and Future Work

6.1 Conclusion

The primary goal of image-guided surgery (IGS) is to provide structural and/or functional information to the surgeon in clinical settings. Optical imaging techniques for IGS have been explored widely for real-time clinical imaging, ranging from fluorescence imaging to two-photon imaging, polarization contrast imaging, and others. These imaging techniques allow for the accurate assessment of tumor margins during surgical procedures, as well as for identification of secondary tumor sites that otherwise would be missed by the unaided eye. As such, my research is targeted at developing an NIR fluorescence imaging system (NFIS) for IGS that includes a compact design, real-time imaging with high fluorescence signal sensitivity, and accurate multispectral information co-registration.

In order to develop a system that can meet those requirements, three non-bio-inspired NIR fluorescence imaging systems were developed to achieve a compact NIR fluorescence goggle system solution with real-time imaging capability. The system architectures and performance evaluation are presented in Chapters 2 and 3.

The first NFIS is a threshold-detection-based, two-camera system that can be integrated easily with a goggle display system for intraoperative guidance. The proposed NFIS achieves NIR–visible image overlay with high precision and a real-time frame rate. In addition, the miniature, ultra-lightweight LED tracking pod is easy to incorporate with an NIR fluorescence imaging study. Based on experimental evaluations in a mouse *in vivo* study, the proposed NFIS solution can achieve down to 25nM ICG detectability at 27 FPS, and it can realize a highly precise image

overlay of NIR and visible images. The overlay error is limited within a 2mm scale at a 65cm working distance, which is highly reliable for clinical study and surgical use.

The second NFIS is a scale-invariant feature transform (SIFT) feature matching-based, three-camera system. The proposed NFIS enables a stereoscopic view and tool-free, high-precision image overlay solution for intraoperative guidance. In a characterization test, the proposed NFIS solution achieved a less than 0.4mm disparity error, greater than 25dB SNR, and down to 25nM detectability, while running at a 27FPS frame rate. It also demonstrated accurate NIR–visible image overlay results in an *in vivo* animal study.

The third NFIS is a compact, beam-splitter-based, single-camera system. The proposed system offers 27FPS real-time frame rate NIR–visible dual-channel image streaming. The designs of the electronic and optical components of the proposed NFIS were analyzed, and its performance was evaluated with detectability and sensitivity measurements. Then, the proposed NFIS was tested further in an *in vivo* mouse model study for breast cancer and a human pilot study of sentinel lymph node mapping. The results show that the proposed system could offer sensitive and accurate NIR fluorescence imaging results for possible IGS.

However, all three NFISs have weakness in multispectral channel information co-registration. The first two NFISs have a small disparity error due to the depth difference between the reference point and the targeting area, while the third NFIS requires careful pre-alignment before each experiment. A solution that can overcome these limitations is worth exploring in order to meet the urgent need for an NFIS for IGS. As such, in the subsequent chapters, this dissertation proposes a novel, bio-inspired, on-chip solution for multispectral imaging.

In addition, by mimicking the ommatidium structure of the butterfly, a new, bio-inspired, multispectral imaging sensor and the corresponding NFIS setup for NIR fluorescence imaging were developed, and they are presented in Chapter 4. In the proposed multispectral imaging sensor, pixelated spectral inference filters (R, G, B, and NIR) are integrated with a light-sensitive CCD imaging sensing unit. The pixelated spectral filters are fabricated by following a carefully optimized nanofabrication procedure, and they are integrated with a CCD imaging array using off-chip alignment technology. Visible channel information is instinctively co-registered with the NIR channel, with only sub-pixel co-registration error; thus, the single-imaging sensor solution can be a revolutionary solution for compact multispectral imaging. The entire imaging system has been optimized for high signal-to-background fluorescence imaging using an analytical approach that has been verified experimentally. This bio-inspired spectral imaging sensor is integrated with wearable goggles for easy integration in the operating room. An *in vivo* animal study showed the potential of using the proposed imaging sensor with blood perfusion.

To address the low spatial resolution and non-uniform pixel response of the proposed bio-inspired, multispectral imaging sensor, corresponding imaging processing technologies were explored to improve the performance and imaging quality of the proposed imaging sensor. A calibration method implemented with the proposed multispectral imaging sensor is presented in Chapter 4. In addition, several existing interpolation algorithms and a new, gradient-based interpolation algorithm for the proposed multispectral imaging sensor and DoFP polarization imaging sensor are presented in Chapter 5. The performance of the proposed gradient-based interpolation algorithm was compared against the performances of three other interpolation algorithms in terms of MTF evaluation, visual comparison, and RMSE testing. The theoretical frameworks of all four interpolation algorithms were also presented.

6.2 Future Work

In the future, our proposed multispectral imaging sensor and corresponding NFIS will be evaluated in several domains, such as cancer imaging or blood flow perfusion in clinical research; single-snapshot, 3D image reconstruction using NIR light; super-high-speed, high-resolution, multispectral imaging; and possibly, combined gesture control or motion tracking using NIR light with visible imaging.

In addition, to reduce the weight and size of the proposed multispectral imaging sensor further, a similar sensor structure will be implemented on a CMOS imaging sensor. By taking the advantages of the CMOS imaging sensor, such as low power, flexible pixel exposure control, compactness, and light weight, our future NFIS can be a lightweight, remote[103] and compact solution for different applications.

Finally, this biomimicry concept of on-chip multispectral imaging can motivate research on multimodal imaging even further. For instance, because a single-imaging sensor can realize single-modal imaging, it is possible to combine such components as a multispectral imaging sensor, a polarization imaging sensor, and a thermal sensor into a compact case setup. It is expected that a potential multimodal imaging device with a small footprint will be developed in the future.

References

[1] S. Thevarajah, T. L. Huston, and R. M. Simmons, "A comparison of the adverse reactions associated with isosulfan blue versus methylene blue dye in sentinel lymph node biopsy for breast cancer," *Am. J. Surg.*, vol. 189, no. 2, pp. 236–239, Feb. 2005.

[2] L. Jacobs, "Positive Margins: The Challenge Continues for Breast Surgeons," *Ann. Surg. Oncol.*, vol. 15, no. 5, pp. 1271–1272, May 2008.

[3] A. L. Vahrmeijer, M. Hutteman, J. R. van der Vorst, C. J. H. van de Velde, and J. V. Frangioni, "Image-guided cancer surgery using near-infrared fluorescence," *Nat. Rev. Clin. Oncol.*, vol. 10, no. 9, pp. 507–518, Sep. 2013.

[4] S. Gioux, H. S. Choi, and J. V. Frangioni, "Image-guided surgery using invisible near-infrared light: fundamentals of clinical translation," *Mol. Imaging*, vol. 9, no. 5, pp. 237–255, Oct. 2010.

[5] D. G. Stavenga, "Reflections on colourful ommatidia of butterfly eyes," *J. Exp. Biol.*, vol. 205, no. Pt 8, pp. 1077–1085, Apr. 2002.

[6] R. Weissleder and M. J. Pittet, "Imaging in the era of molecular oncology," *Nature*, vol. 452, no. 7187, pp. 580–589, Apr. 2008.

[7] M. Badruddoja, "Ductal Carcinoma In Situ of the Breast: A Surgical Perspective," *Int. J. Surg. Oncol.*, vol. 2012, p. e761364, Sep. 2012.

[8] A. L. Vahrmeijer, M. Hutteman, J. R. van der Vorst, C. J. H. van de Velde, and J. V. Frangioni, "Image-guided cancer surgery using near-infrared fluorescence," *Nat. Rev. Clin. Oncol.*, vol. 10, no. 9, pp. 507–518, Sep. 2013.

[9] S. Gioux, H. S. Choi, and J. V. Frangioni, "Image-guided surgery using invisible near-infrared light: fundamentals of clinical translation," *Mol. Imaging*, vol. 9, no. 5, pp. 237–255, Oct. 2010.

[10] M. V. Marshall, J. C. Rasmussen, I.-C. Tan, M. B. Aldrich, K. E. Adams, X. Wang, C. E. Fife, E. A. Maus, L. A. Smith, and E. M. Sevick-Muraca, "Near-Infrared Fluorescence Imaging in Humans with Indocyanine Green: A Review and Update," *Open Surg. Oncol. J. Online*, vol. 2, no. 2, pp. 12–25, 2010.

[11] S. Luo, E. Zhang, Y. Su, T. Cheng, and C. Shi, "A review of NIR dyes in cancer targeting and imaging," *Biomaterials*, vol. 32, no. 29, pp. 7127–7138, Oct. 2011.

[12] E. R. Fossum, "CMOS image sensors: electronic camera on a chip," in *Electron Devices Meeting, 1995. IEDM '95., International*, 1995, pp. 17–25.

[13] S. L. Troyan, V. Kianzad, S. L. Gibbs-Strauss, S. Gioux, A. Matsui, R. Oketokoun, L. Ngo, A. Khamene, F. Azar, and J. V. Frangioni, "The FLARE intraoperative near-infrared fluorescence imaging system: a first-in-human clinical trial in breast cancer sentinel lymph node mapping," *Ann. Surg. Oncol.*, vol. 16, no. 10, pp. 2943–2952, Oct. 2009.

[14] J. S. D. Mieog, S. L. Troyan, M. Hutteman, K. J. Donohoe, J. R. van der Vorst, A. Stockdale, G.-J. Liefers, H. S. Choi, S. L. Gibbs-Strauss, H. Putter, S. Gioux, P. J. K. Kuppen, Y. Ashitate, C. W. G. M. Lowik, V. T. H. B. M. Smit, R. Oketokoun, L. H. Ngo, C. J. H. van de Velde, J. V. Frangioni, and A. L. Vahrmeijer, "Toward Optimization of Imaging System and Lymphatic Tracer for Near-Infrared Fluorescent Sentinel Lymph Node Mapping in Breast Cancer," *Ann. Surg. Oncol.*, vol. 18, no. 9, pp. 2483–2491, Sep. 2011.

[15] M. Takahashi, T. Ishikawa, K. Higashidani, and H. Katoh, "SPY^{TM}: an innovative intra-operative imaging system to evaluate graft patency during off-pump coronary artery

bypass grafting," *Interact. Cardiovasc. Thorac. Surg.*, vol. 3, no. 3, pp. 479–483, Sep. 2004.
[16] N. Tagaya, R. Yamazaki, A. Nakagawa, A. Abe, K. Hamada, K. Kubota, and T. Oyama, "Intraoperative identification of sentinel lymph nodes by near-infrared fluorescence imaging in patients with breast cancer," *Am. J. Surg.*, vol. 195, no. 6, pp. 850–853, Jun. 2008.
[17] S. B. Mondal, S. Gao, N. Zhu, R. Liang, V. Gruev, and S. Achilefu, "Real-Time Fluorescence Image-Guided Oncologic Surgery," in *Advances in Cancer Research*, vol. 124, Elsevier, 2014, pp. 171–211.
[18] V. Venugopal, M. Park, Y. Ashitate, F. Neacsu, F. Kettenring, J. V. Frangioni, S. P. Gangadharan, and S. Gioux, "Design and characterization of an optimized simultaneous color and near-infrared fluorescence rigid endoscopic imaging system," *J. Biomed. Opt.*, vol. 18, no. 12, p. 126018, Dec. 2013.
[19] J. Glatz, J. Varga, P. B. Garcia-Allende, M. Koch, F. R. Greten, and V. Ntziachristos, "Concurrent video-rate color and near-infrared fluorescence laparoscopy," *J. Biomed. Opt.*, vol. 18, no. 10, p. 101302, Oct. 2013.
[20] X. Wang, S. Bhaumik, Q. Li, V. P. Staudinger, and S. Yazdanfar, "Compact instrument for fluorescence image-guided surgery," *J. Biomed. Opt.*, vol. 15, no. 2, p. 020509, Apr. 2010.
[21] S. Gioux, J.-G. Coutard, M. Berger, H. Grateau, V. Josserand, M. Keramidas, C. Righini, J.-L. Coll, and J.-M. Dinten, "FluoSTIC: miniaturized fluorescence image-guided surgery system," *J. Biomed. Opt.*, vol. 17, no. 10, p. 106014, Oct. 2012.
[22] Y. Liu, R. Njuguna, T. Matthews, W. J. Akers, G. P. Sudlow, S. Mondal, R. Tang, V. Gruev, and S. Achilefu, "Near-infrared fluorescence goggle system with complementary metal-oxide-semiconductor imaging sensor and see-through display," *J. Biomed. Opt.*, vol. 18, no. 10, p. 101303, Oct. 2013.
[23] P. Shao, H. Ding, J. Wang, P. Liu, Q. Ling, J. Chen, J. Xu, S. Zhang, and R. Xu, "Designing a Wearable Navigation System for Image-Guided Cancer Resection Surgery," *Ann. Biomed. Eng.*, Jul. 2014.
[24] S. Gao, S. B. Mondal, N. Zhu, R. Liang, S. Achilefu, and V. Gruev, "Image overlay solution based on threshold detection for a compact near infrared fluorescence goggle system," *J. Biomed. Opt.*, vol. 20, no. 1, pp. 016018–016018, 2015.
[25] S. Achilefu, H. N. Jimenez, R. B. Dorshow, J. E. Bugaj, E. G. Webb, R. R. Wilhelm, R. Rajagopalan, J. Johler, and J. L. Erion, "Synthesis, in vitro receptor binding, and in vivo evaluation of fluorescein and carbocyanine peptide-based optical contrast agents," *J. Med. Chem.*, vol. 45, no. 10, pp. 2003–2015, May 2002.
[26] M. Y. Berezin, H. Lee, W. Akers, and S. Achilefu, "Near Infrared Dyes as Lifetime Solvatochromic Probes for Micropolarity Measurements of Biological Systems," *Biophys. J.*, vol. 93, no. 8, pp. 2892–2899, Oct. 2007.
[27] V. Venugopal, M. Park, Y. Ashitate, F. Neacsu, F. Kettenring, J. V. Frangioni, S. P. Gangadharan, and S. Gioux, "Design and characterization of an optimized simultaneous color and near-infrared fluorescence rigid endoscopic imaging system," *J. Biomed. Opt.*, vol. 18, no. 12, pp. 126018–126018, 2013.
[28] S. Gioux, J.-G. Coutard, M. Berger, H. Grateau, V. Josserand, M. Keramidas, C. Righini, J.-L. Coll, and J.-M. Dinten, "FluoSTIC: miniaturized fluorescence image-guided surgery system," *J. Biomed. Opt.*, vol. 17, no. 10, pp. 106014–106014, 2012.

[29] N. Zhu, S. Mondal, S. Gao, S. Achilefu, V. Gruev, and R. Liang, "Engineering light-emitting diode surgical light for near-infrared fluorescence image-guided surgical systems," *J. Biomed. Opt.*, vol. 19, no. 7, pp. 076018–076018, 2014.
[30] D. G. Lowe, "Distinctive Image Features from Scale-Invariant Keypoints," *Int. J. Comput. Vis.*, vol. 60, no. 2, pp. 91–110, Nov. 2004.
[31] C. Liu, J. Yuen, and A. Torralba, "SIFT Flow: Dense Correspondence across Scenes and Its Applications," *IEEE Trans. Pattern Anal. Mach. Intell.*, vol. 33, no. 5, pp. 978–994, May 2011.
[32] S. Agarwal, Y. Furukawa, N. Snavely, I. Simon, B. Curless, S. M. Seitz, and R. Szeliski, "Building Rome in a Day," *Commun ACM*, vol. 54, no. 10, pp. 105–112, Oct. 2011.
[33] X. Xiong and F. De la Torre, "Supervised Descent Method and Its Applications to Face Alignment," in *2013 IEEE Conference on Computer Vision and Pattern Recognition (CVPR)*, 2013, pp. 532–539.
[34] Y. Liu, R. Njuguna, T. Matthews, W. J. Akers, G. P. Sudlow, S. Mondal, R. Tang, V. Gruev, and S. Achilefu, "Near-infrared fluorescence goggle system with complementary metal-oxide-semiconductor imaging sensor and see-through display," *J. Biomed. Opt.*, vol. 18, no. 10, p. 101303, 2013.
[35] L. Ma, K. Agrawal, and R. D. Chamberlain, "Theoretical Analysis of Classic Algorithms on Highly-threaded Many-core GPUs," in *Proc. of the 19th ACM SIGPLAN Symposium on Principles and Practice of Parallel Programming (PPoPP)*, Orlando, Florida, USA, 2014, pp. 391–392.
[36] L. Ma, K. Agrawal, and R. D. Chamberlain, "Analysis of Classic Algorithms on GPUs," in *Proc. of the 12th ACM/IEEE Int'l Conf. on High Performance Computing and Simulation (HPCS)*, Bologna, Italy, 2014.
[37] P. Li, K. Agrawal, J. Buhler, and R. D. Chamberlain, "Adding data parallelism to streaming pipelines for throughput optimization," in *HiPC*, 2013, pp. 20–29.
[38] J. C. Beard, P. Li, and R. D. Chamberlain, "RaftLib: A C++ template library for high performance stream parallel processing," in *Proceedings of Programming Models and Applications on Multicores and Manycores*, New York, NY, USA, 2015.
[39] N. Zhu, S. Mondal, S. Gao, S. Achilefua, V. Gruev, and R. Liang, "Dual-mode optical imaging system for fluorescence image-guided surgery," *Opt. Lett.*, vol. 39, no. 13, pp. 3830–3832, Jul. 2014.
[40] T. York, S. B. Powell, S. Gao, L. Kahan, T. Charanya, D. Saha, N. W. Roberts, T. W. Cronin, J. Marshall, S. Achilefu, S. P. Lake, B. Raman, and V. Gruev, "Bioinspired Polarization Imaging Sensors: From Circuits and Optics to Signal Processing Algorithms and Biomedical Applications," *Proc. IEEE*, vol. 102, no. 10, pp. 1450–1469, Oct. 2014.
[41] M. V. Marshall, J. C. Rasmussen, I.-C. Tan, M. B. Aldrich, K. E. Adams, X. Wang, C. E. Fife, E. A. Maus, L. A. Smith, and E. M. Sevick-Muraca, "Near-Infrared Fluorescence Imaging in Humans with Indocyanine Green: A Review and Update," *Open Surg. Oncol. J. Online*, vol. 2, no. 2, pp. 12–25, 2010.
[42] S. Gao, S. B. Mondal, N. Zhu, R. Liang, S. Achilefu, and V. Gruev, "Image overlay solution based on threshold detection for a compact near infrared fluorescence goggle system," *J. Biomed. Opt.*, vol. 20, no. 1, pp. 016018–016018, 2015.
[43] S. L. Troyan, V. Kianzad, S. L. Gibbs-Strauss, S. Gioux, A. Matsui, R. Oketokoun, L. Ngo, A. Khamene, F. Azar, and J. V. Frangioni, "The FLARE intraoperative near-infrared

fluorescence imaging system: a first-in-human clinical trial in breast cancer sentinel lymph node mapping," *Ann. Surg. Oncol.*, vol. 16, no. 10, pp. 2943–2952, Oct. 2009.
[44] C. Hirche, H. Engel, L. Kolios, J. Cognie, M. Hünerbein, M. Lehnhardt, and T. Kremer, "An Experimental Study to Evaluate the Fluobeam 800 Imaging System for Fluorescence-Guided Lymphatic Imaging and Sentinel Node Biopsy," *Surg. Innov.*, p. 1553350612468962, Dec. 2012.
[45] S. Gioux, H. S. Choi, and J. V. Frangioni, "Image-Guided Surgery using Invisible Near-Infrared Light: Fundamentals of Clinical Translation," *Mol. Imaging*, vol. 9, no. 5, pp. 237–255, Oct. 2010.
[46] N. Zhu, S. Mondal, S. Gao, S. Achilefu, V. Gruev, and R. Liang, "Engineering light-emitting diode surgical light for near-infrared fluorescence image-guided surgical systems," *J. Biomed. Opt.*, vol. 19, no. 7, pp. 076018–076018, 2014.
[47] Y. Liu, R. Njuguna, T. Matthews, W. J. Akers, G. P. Sudlow, S. Mondal, R. Tang, V. Gruev, and S. Achilefu, "Near-infrared fluorescence goggle system with complementary metal-oxide-semiconductor imaging sensor and see-through display," *J. Biomed. Opt.*, vol. 18, no. 10, Oct. 2013.
[48] S. Achilefu, H. N. Jimenez, R. B. Dorshow, J. E. Bugaj, E. G. Webb, R. R. Wilhelm, R. Rajagopalan, J. Johler, and J. L. Erion, "Synthesis, in vitro receptor binding, and in vivo evaluation of fluorescein and carbocyanine peptide-based optical contrast agents," *J. Med. Chem.*, vol. 45, no. 10, pp. 2003–2015, May 2002.
[49] V. Venugopal, M. Park, Y. Ashitate, F. Neacsu, F. Kettenring, J. V. Frangioni, S. P. Gangadharan, and S. Gioux, "Design and characterization of an optimized simultaneous color and near-infrared fluorescence rigid endoscopic imaging system," *J. Biomed. Opt.*, vol. 18, no. 12, Dec. 2013.
[50] J. Glatz, J. Varga, P. B. Garcia-Allende, M. Koch, F. R. Greten, and V. Ntziachristos, "Concurrent video-rate color and near-infrared fluorescence laparoscopy," *J. Biomed. Opt.*, vol. 18, no. 10, Oct. 2013.
[51] S. Gioux, H. S. Choi, and J. V. Frangioni, "Image-guided surgery using invisible near-infrared light: fundamentals of clinical translation," *Mol. Imaging*, vol. 9, no. 5, pp. 237–255, Oct. 2010.
[52] S. B. Mondal, S. Gao, N. Zhu, R. Liang, V. Gruev, and S. Achilefu, "Real-Time Fluorescence Image-Guided Oncologic Surgery," in *Advances in Cancer Research*, vol. 124, Elsevier, 2014, pp. 171–211.
[53] Y. Liu, R. Njuguna, T. Matthews, W. J. Akers, G. P. Sudlow, S. Mondal, R. Tang, V. Gruev, and S. Achilefu, "Near-infrared fluorescence goggle system with complementary metal-oxide-semiconductor imaging sensor and see-through display," *J. Biomed. Opt.*, vol. 18, no. 10, p. 101303, 2013.
[54] J. S. D. Mieog, S. L. Troyan, M. Hutteman, K. J. Donohoe, J. R. van der Vorst, A. Stockdale, G.-J. Liefers, H. S. Choi, S. L. Gibbs-Strauss, H. Putter, S. Gioux, P. J. K. Kuppen, Y. Ashitate, C. W. G. M. Lowik, V. T. H. B. M. Smit, R. Oketokoun, L. H. Ngo, C. J. H. van de Velde, J. V. Frangioni, and A. L. Vahrmeijer, "Toward Optimization of Imaging System and Lymphatic Tracer for Near-Infrared Fluorescent Sentinel Lymph Node Mapping in Breast Cancer," *Ann. Surg. Oncol.*, vol. 18, no. 9, pp. 2483–2491, Sep. 2011.

[55] S. Gioux, J.-G. Coutard, M. Berger, H. Grateau, V. Josserand, M. Keramidas, C. Righini, J.-L. Coll, and J.-M. Dinten, "FluoSTIC: miniaturized fluorescence image-guided surgery system," *J. Biomed. Opt.*, vol. 17, no. 10, Oct. 2012.
[56] R. A. Potyrailo, H. Ghiradella, A. Vertiatchikh, K. Dovidenko, J. R. Cournoyer, and E. Olson, "Morpho butterfly wing scales demonstrate highly selective vapour response," *Nat. Photonics*, vol. 1, no. 2, pp. 123–128, Feb. 2007.
[57] P. Vukusic and J. R. Sambles, "Photonic structures in biology," *Nature*, vol. 424, no. 6950, pp. 852–855, Aug. 2003.
[58] A. D. Pris, Y. Utturkar, C. Surman, W. G. Morris, A. Vert, S. Zalyubovskiy, T. Deng, H. T. Ghiradella, and R. A. Potyrailo, "Towards high-speed imaging of infrared photons with bio-inspired nanoarchitectures," *Nat. Photonics*, vol. 6, no. 3, pp. 195–200, Mar. 2012.
[59] M. Srinivasarao, "Nano-Optics in the Biological World: Beetles, Butterflies, Birds, and Moths," *Chem. Rev.*, vol. 99, no. 7, pp. 1935–1962, Jul. 1999.
[60] G. R. Fowles, *Introduction to Modern Optics*. Courier Corporation, 1975.
[61] Kodak, "KODAK KAI-2020 Imaging Sensor 1600 (H) x 1200 (V) Interline Transfer Progressive Scan CCD." 2005.
[62] J. S. D. Mieog, S. L. Troyan, M. Hutteman, K. J. Donohoe, J. R. van der Vorst, A. Stockdale, G.-J. Liefers, H. S. Choi, S. L. Gibbs-Strauss, H. Putter, S. Gioux, P. J. K. Kuppen, Y. Ashitate, C. W. G. M. Lowik, V. T. H. B. M. Smit, R. Oketokoun, L. H. Ngo, C. J. H. van de Velde, J. V. Frangioni, and A. L. Vahrmeijer, "Toward Optimization of Imaging System and Lymphatic Tracer for Near-Infrared Fluorescent Sentinel Lymph Node Mapping in Breast Cancer," *Ann. Surg. Oncol.*, vol. 18, no. 9, pp. 2483–2491, Sep. 2011.
[63] V. Venugopal, M. Park, Y. Ashitate, F. Neacsu, F. Kettenring, J. V. Frangioni, S. P. Gangadharan, and S. Gioux, "Design and characterization of an optimized simultaneous color and near-infrared fluorescence rigid endoscopic imaging system," *J. Biomed. Opt.*, vol. 18, no. 12, Dec. 2013.
[64] T. York, S. B. Powell, S. Gao, L. Kahan, T. Charanya, D. Saha, N. W. Roberts, T. W. Cronin, J. Marshall, S. Achilefu, S. P. Lake, B. Raman, and V. Gruev, "Bioinspired Polarization Imaging Sensors: From Circuits and Optics to Signal Processing Algorithms and Biomedical Applications," *Proc. IEEE*, vol. 102, no. 10, pp. 1450–1469, Oct. 2014.
[65] T. Charanya, T. York, S. Bloch, G. Sudlow, K. Liang, M. Garcia, W. J. Akers, D. Rubin, V. Gruev, and S. Achilefu, "Trimodal color-fluorescence-polarization endoscopy aided by a tumor selective molecular probe accurately detects flat lesions in colitis-associated cancer," *J. Biomed. Opt.*, vol. 19, no. 12, p. 126002, Dec. 2014.
[66] R. Patel, A. Khan, R. Quinlan, and A. N. Yaroslavsky, "Polarization-sensitive multimodal imaging for detecting breast cancer," *Cancer Res.*, vol. 74, no. 17, pp. 4685–4693, Sep. 2014.
[67] L. Tchvialeva, G. Dhadwal, H. Lui, S. Kalia, H. Zeng, D. I. McLean, and T. K. Lee, "Polarization speckle imaging as a potential technique for in vivo skin cancer detection," *J. Biomed. Opt.*, vol. 18, no. 6, p. 061211, Jun. 2013.
[68] Y. Pu, W. B. Wang, G. C. Tang, F. Zeng, S. Achilefu, J. H. Vitenson, I. Sawczuk, S. Peters, J. M. Lombardo, and R. R. Alfano, "Spectral polarization imaging of human prostate cancer tissue using a near-infrared receptor-targeted contrast agent," *Technol. Cancer Res. Treat.*, vol. 4, no. 4, pp. 429–436, Aug. 2005.

[69] J. T. Alander, I. Kaartinen, A. Laakso, T. Pätilä, T. Spillmann, V. V. Tuchin, M. Venermo, and P. Välisuo, "A Review of Indocyanine Green Fluorescent Imaging in Surgery," *Int. J. Biomed. Imaging*, vol. 2012, p. e940585, Apr. 2012.
[70] V. Gruev, R. Perkins, and T. York, "CCD polarization imaging sensor with aluminum nanowire optical filters," *Opt. Express*, vol. 18, no. 18, pp. 19087–19094, Aug. 2010.
[71] R. Perkins and V. Gruev, "Signal-to-noise analysis of Stokes parameters in division of focal plane polarimeters," *Opt. Express*, vol. 18, no. 25, pp. 25815–25824, Dec. 2010.
[72] T. York and V. Gruev, "Characterization of a visible spectrum division-of-focal-plane polarimeter," *Appl. Opt.*, vol. 51, no. 22, pp. 5392–5400, Aug. 2012.
[73] J. S. Tyo, D. L. Goldstein, D. B. Chenault, and J. A. Shaw, "Review of passive imaging polarimetry for remote sensing applications," *Appl. Opt.*, vol. 45, no. 22, pp. 5453–5469, Aug. 2006.
[74] Y. Liu, T. York, W. Akers, G. Sudlow, V. Gruev, and S. Achilefu, "Complementary fluorescence-polarization microscopy using division-of-focal-plane polarization imaging sensor," *J. Biomed. Opt.*, vol. 17, no. 11, p. 116001, Nov. 2012.
[75] D. Miyazaki, R. T. Tan, K. Hara, and K. Ikeuchi, "Polarization-based inverse rendering from a single view," in *Ninth IEEE International Conference on Computer Vision, 2003. Proceedings*, 2003, pp. 982–987 vol.2.
[76] Y. Y. Schechner and N. Karpel, "Recovery of underwater visibility and structure by polarization analysis," *IEEE J. Ocean. Eng.*, vol. 30, no. 3, pp. 570–587, Jul. 2005.
[77] T. V. T. Krishna, C. D. Creusere, and D. G. Voelz, "Passive Polarimetric Imagery-Based Material Classification Robust to Illumination Source Position and Viewpoint," *IEEE Trans. Image Process.*, vol. 20, no. 1, pp. 288–292, Jan. 2011.
[78] M. Sarkar, D. San Segundo Bello, C. Van Hoof, and A. Theuwissen, "Integrated Polarization Analyzing CMOS Image Sensor for Material Classification," *IEEE Sens. J.*, vol. 11, no. 8, pp. 1692–1703, Aug. 2011.
[79] M. Anastasiadou, A. D. Martino, D. Clement, F. Liège, B. Laude-Boulesteix, N. Quang, J. Dreyfuss, B. Huynh, A. Nazac, L. Schwartz, and H. Cohen, "Polarimetric imaging for the diagnosis of cervical cancer," *Phys. Status Solidi C*, vol. 5, no. 5, pp. 1423–1426, May 2008.
[80] E. Salomatina-Motts, V. A. Neel, and A. N. Yaroslavskaya, "Multimodal polarization system for imaging skin cancer," *Opt. Spectrosc.*, vol. 107, no. 6, pp. 884–890, Dec. 2009.
[81] B. E. Bayer, "Color imaging array," US3971065 A, 20-Jul-1976.
[82] Z. Dengwen, "An edge-directed bicubic interpolation algorithm," in *2010 3rd International Congress on Image and Signal Processing (CISP)*, 2010, vol. 3, pp. 1186–1189.
[83] A. Giachetti and N. Asuni, "Real-Time Artifact-Free Image Upscaling," *IEEE Trans. Image Process.*, vol. 20, no. 10, pp. 2760–2768, Oct. 2011.
[84] J. Canny, "A Computational Approach to Edge Detection," *IEEE Trans. Pattern Anal. Mach. Intell.*, vol. PAMI-8, no. 6, pp. 679–698, Nov. 1986.
[85] B. M. Ratliff, C. F. LaCasse, and J. S. Tyo, "Interpolation strategies for reducing IFOV artifacts in microgrid polarimeter imagery," *Opt. Express*, vol. 17, no. 11, pp. 9112–9125, May 2009.
[86] S. Gao and V. Gruev, "Bilinear and bicubic interpolation methods for division of focal plane polarimeters," *Opt. Express*, vol. 19, no. 27, pp. 26161–26173, Dec. 2011.

[87] S. Gao and V. Gruev, “Image interpolation methods evaluation for division of focal plane polarimeters,” 2011, vol. 8012, p. 80120N–80120N–10.
[88] R. Keys, “Cubic convolution interpolation for digital image processing,” *Acoust. Speech Signal Process. IEEE Trans. On*, vol. 29, no. 6, pp. 1153–1160, Dec. 1981.
[89] S. Gao and V. Gruev, “Gradient-based interpolation method for division-of-focal-plane polarimeters,” *Opt. Express*, vol. 21, no. 1, pp. 1137–1151, Jan. 2013.
[90] J. J. Peltzer, P. D. Flammer, T. E. Furtak, R. T. Collins, and R. E. Hollingsworth, “Ultra-high extinction ratio micropolarizers using plasmonic lenses,” *Opt Express*, vol. 19, no. 19, pp. 18072–18079, Sep. 2011.
[91] Y. Zhao, M. A. Belkin, and A. Alù, “Twisted optical metamaterials for planarized ultrathin broadband circular polarizers,” *Nat Commun*, vol. 3, p. 870, May 2012.
[92] W.-L. Hsu, G. Myhre, K. Balakrishnan, N. Brock, M. Ibn-Elhaj, and S. Pau, “Full-Stokes imaging polarimeter using an array of elliptical polarizer,” *Opt Express*, vol. 22, no. 3, pp. 3063–3074, Feb. 2014.
[93] W.-L. Hsu, J. Davis, K. Balakrishnan, M. Ibn-Elhaj, S. Kroto, N. Brock, and S. Pau, “Polarization microscope using a near infrared full-Stokes imaging polarimeter,” *Opt Express*, vol. 23, no. 4, pp. 4357–4368, Feb. 2015.
[94] H. S. Hou and H. Andrews, “Cubic splines for image interpolation and digital filtering,” *IEEE Trans. Acoust. Speech Signal Process.*, vol. 26, no. 6, pp. 508–517, Dec. 1978.
[95] R. L. Burden and J. D. Faires, *Numerical Analysis*, 9th edition. Florence, KY: Brooks Cole, 2010.
[96] T. York, S. Powell, and V. Gruev, “A comparison of polarization image processing across different platforms,” 2011, vol. 8160, pp. 816004–816004–7.
[97] X. Li and M. T. Orchard, “New edge-directed interpolation,” *IEEE Trans. Image Process.*, vol. 10, no. 10, pp. 1521–1527, Oct. 2001.
[98] K. Jensen and D. Anastassiou, “Subpixel edge localization and the interpolation of still images,” *IEEE Trans. Image Process.*, vol. 4, no. 3, pp. 285–295, Mar. 1995.
[99] J. Canny, “A Computational Approach to Edge Detection,” *Pattern Anal. Mach. Intell. IEEE Trans. On*, vol. PAMI-8, no. 6, pp. 679–698, Nov. 1986.
[100] G. D. Boreman, *Modulation Transfer Function in Optical and Electro-Optical Systems*, vol. TT52. SPIE PRESS BOOK, 2001.
[101] V. Gruev, R. Perkins, and T. York, “CCD polarization imaging sensor with aluminum nanowire optical filters,” *Opt. Express*, vol. 18, no. 18, pp. 19087–19094, Aug. 2010.
[102] A. C. Neville and B. M. Luke, “Form optical activity in crustacean cuticle,” *J. Insect Physiol.*, vol. 17, no. 3, pp. 519 – 526, 1971.
[103] B. Li, L. Nie, C. Wu, and H. G. C. Lu, “Incorporating Emergency Alarms in Reliable Wireless Process Control,” in *ACM/IEEE International Conference on Cyber-Physical Systems (ICCPS’15)*, 2015.